Smith Purcell Radiation from Femtosecond Electron Bunches

by

Stephen E. Korbly

A.B. (Physics), Princeton University, Princeton, NJ (1997)

Submitted to the
Department of Physics
in partial fulfillment of the requirements for the degree of

Doctor of Philosophy

at the

MASSACHUSETTS INSTITUTE OF TECHNOLOGY

February 2005

Signature of Author ... .
Department of Physics
November 10, 2004

Certified by .....
Richard J. Temkin
Senior Scientist, Department of Physics
Thesis Supervisor

Accepted by .....
Thomas J. Greytak
Associate Department Head for Education

Smith Purcell Radiation from Femtosecond Electron Bunches

by

Stephen E. Korbly

Submitted to the Department of Physics
on November 10, 2004, in partial fulfillment of the
requirements for the degree of
Doctor of Philosophy

Abstract

We present theoretical and experimental results from a Smith-Purcell radiation experiment using the electron beam from a 17 GHz high gradient accelerator. Smith-Purcell radiation occurs when a charged particle travels above a periodic grating structure. The electron beam consists of a train of 15 MeV, 9 pC bunches of bunch lengths varying from 600 fs to 1 ps. The radiated energy for one electron travelling above a periodic grating is solved. The effects of multiple electrons in a bunch and multiple bunches in a train are introduced. The Smith-Purcell resonance condition and the dependence of the radiated energy upon beam current and beam height above the grating are presented. Measurement of the angular distribution of the Smith-Purcell radiation resulted in bunch length measurements of 0.60 $\pm$ 0.1 ps and 1 $\pm$ 0.1 ps under different accelerator operating conditions. This demonstrates the use of Smith-Purcell radiation as a non-destructive bunch length diagnostic with 100 fs resolution. Smith-Purcell radiation is comparable to other sources of radiation, such as transistion radiation, synchrotron radiation, etc. except that it has an inherent enhancement by a factor of N_g, the number of grating periods. Additional enhancement occurs when the electron bunch length is short compared with the radiation wavelength, resulting in coherent emission with an enhancement by a factor of N_e, the number of electrons in the bunch. Finally, the electron beam consists of a regular train of N_b bunches, resulting in an energy density spectrum that is restricted in frequency space to harmonics of the bunch train frequency, with an increase in the energy density at these frequencies by a factor of N_b. We report the first observation of Smith-Purcell radiation displaying all three of these enhancements, that is, with a total enhancement of $N_g \cdot N_e \cdot N_b$. This total enhancement provides a simple method of generating powerful THz radiation at specific frequencies, which can be detected with a high signal to noise ratio by a heterodyne receiver.

Thesis Supervisor: Richard J. Temkin
Title: Senior Scientist, Department of Physics

Acknowledgements

I would particularly like to thank Dr. Richard Temkin for his guidance and assistance throughout this work. Mr. Ivan Mastovsky was very helpful with suggestions during the design of the experiment and assistance with various aspects of the accelerator. I would like to thank Mr. Bill Mulligan for his help with the accelerator operation and interlocks. Dr. Winthrop Brown, Dr. Amit Kesar and Roark Marsh contributed to running of the experiments. I also wish to thank Dr. Michael Shapiro for his assistance in interpreting the results and for his experimental suggestions. Dr. Hayden Brownell assisted with the initial design and offered numerous suggestions. I would also like to thank Dr. Amit Kesar for his continuous assistance with the theory and Dr. Jagadishwar Sirigiri for his help with the heterodyne receiver.

It was my pleasure to work with all of the people in the Accelerator and Gyrotron groups at the Plasma Science and Fusion Center. In particular I would like to thank Jags for making each day at MIT interesting and enjoyable. It would not have been the same without you. I would like to thank my Mom, Dad and Nicole for their support and encouragement throughout this endeavor. Finally, I would like to thank Jenn and Isabella, you have made this whole effort worth it. Jenn, without your continued support and patience I could not have done it without you.

Contents

List of Figures

List of Tables

Chapter 1

Introduction

1.1 Smith Purcell Radiation

Smith-Purcell radiation (SPR), which occurs when a charged particle passes over a periodic structure as shown in Fig. 2-1 was first observed in 1953 [1]. In the 50 years since it was first observed many authors have reported incoherent SPR ranging from the visible to millimeter spectrum [2–6]. Only recently (1990's) was coherent SPR in the millimeter regime [7,8] observed. SPR has been proposed as both a source in the THz (submillimeter) regime and a bunch length diagnostic [9, 10]. This thesis describes the work performed in regard to using SPR to measure sub-picosecond electron bunches and the generation of high power coherent THz radiation from these bunches.

1.2 High Gradient Accelerators

High gradient accelerators are of interest for a wide range of applications including TeV colliders, Free Electron Lasers (FELs) and other high energy electron beam applications such as medicine, materials processing and food irradiation. While the Large Hadron Collider proton collider at CERN is being built, the international high energy physics community has agreed that the next accelerator should be an electron-positron linear collider. An electron collider in the TeV class would be of

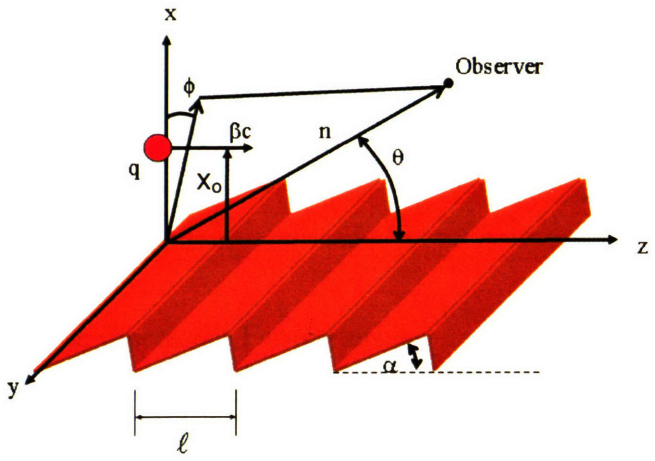

Figure 1-1: Schematic of the Smith-Purcell problem, a charge travelling near a periodic grating structure.

great interest for exploring the frontiers of high energy physics, specifically the search for the Higgs particle. Historical progress in accelerator center of mass energy is illustrated by the "Livingston Chart" shown in Fig. 1-2. Many reports have been given on the general considerations of a TeV linear collider [11–18].

TeV collider designs have been proposed by a number of major laboratories in Europe, Japan, Russia and the United States. Proposed concepts include room temperature copper accelerators, superconducting accelerators and two-beam accelerators. As a result of this initiative, MIT, along with Haimson Research Corporation (HRC), has developed and tested a 17 GHz, 10-30 MeV linear accelerator. 17 GHz is 6 times the frequency, 2.856 GHz, of SLAC. One interesting feature of this high frequency accelerator is that it is designed to produce electron bunches as short as 1°, or ~180 femtoseconds. The accelerator is described in detail in Chapter 3.

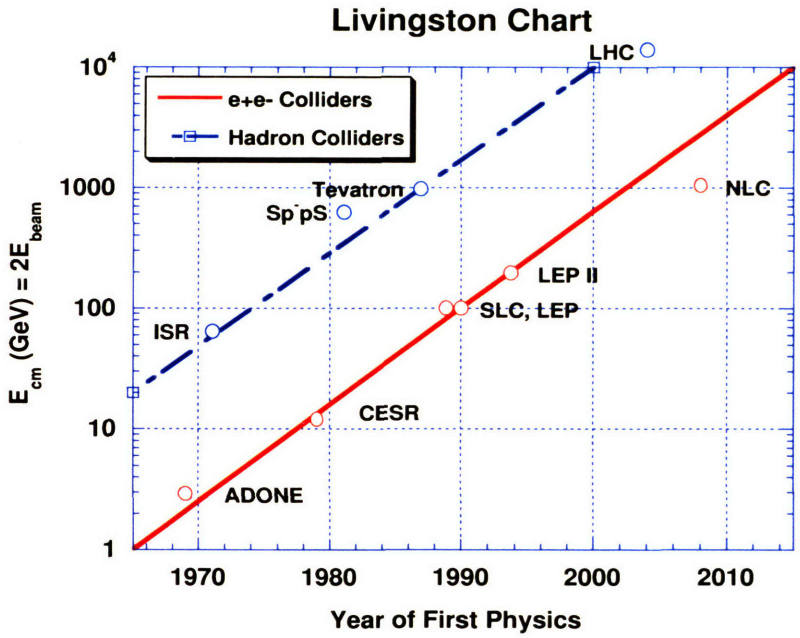

Figure 1-2: Livingston Chart showing the historical progress of accelerators.

1.3 Bunch Length Measurement Techniques

One of the many technical challenges for FELs, linear colliders and advanced accelerators such as laser or plasma wakefield accelerators is the measurement and diagnosis of extremely short bunch lengths. The next generation of light sources will require subpicosecond, kA bunches for operation [19, 20]. Efforts to extend the operating wavelength range of several FELs to XUV (extreme ultraviolet) and soft x-ray continue [21, 22]. The success of these projects requires the demonstration of self-amplified spontaneous emission (SASE). In the SASE mode of operation, an ultrashort, high peak-current, relativistic electron bunch is used to amplify its own spontaneous emission radiation in one pass through an undulator. For these FELs a critical factor for computing, measuring and optimizing the gain is the peak current. The measurement of charge is a straight forward procedure, however, an online diagnostic for measuring bunch length is required to obtain an accurate measurement of peak current.

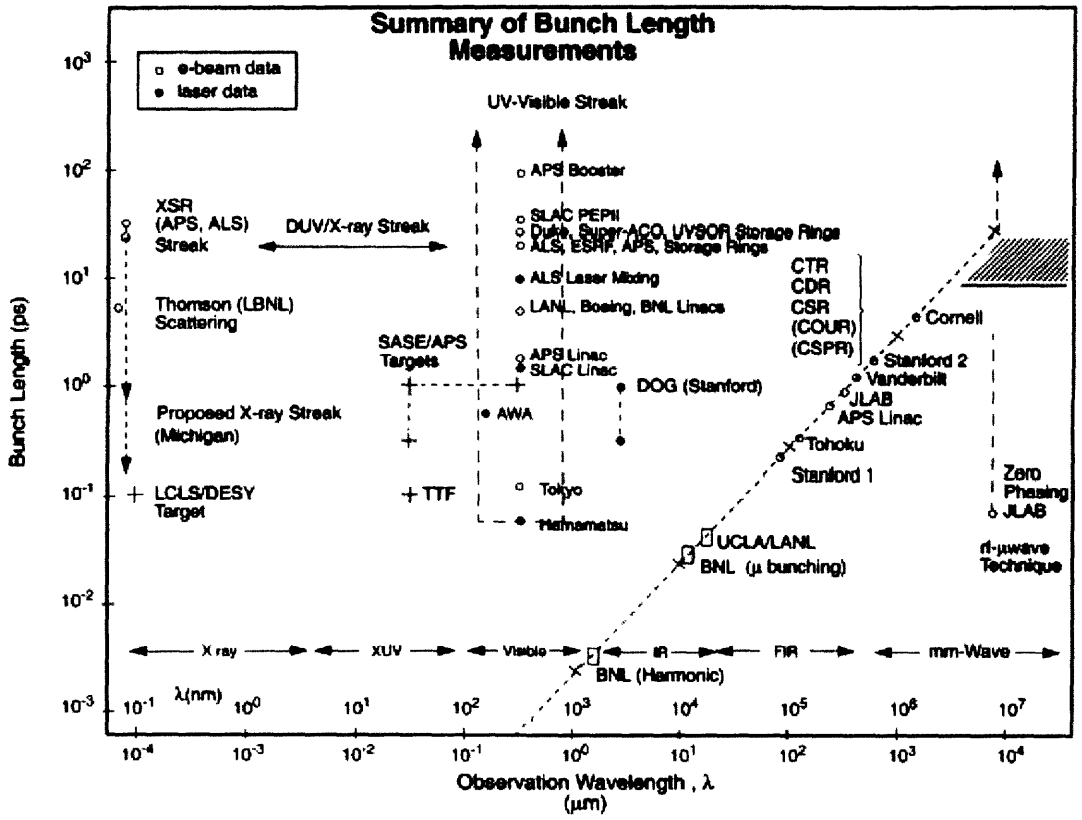

Figure 1-3: Summary of bunch length measurements. Plotted as bunch length in ps versus the observation wavelength. Adapted from [25]

Numerous methods have been developed to measure bunch length including: streak cameras, rf deflecting structures, laser techniques, and coherent and incoherent radiation methods [23, 24]. The many different techniques and their respective bunch length measurements as of 2000 are summarized in Fig. 1-3 [25]. The reader should note from Fig. 1-3 that there are many different techniques being used to measure bunch length, the majority of which have measured picosecond or longer bunch lengths. Unfortunately, many of the demonstrated techniques do not work well for measuring hundred femtosecond bunch lengths. Additionally, most measurement techniques are destructive to the electron beam. A Smith-Purcell radiation (SPR)

bunch length diagnostic can effectively measure femtosecond bunches with minimal effect on the bunch. A brief summary of the existing bunch length techniques is given in the remainder of this section.

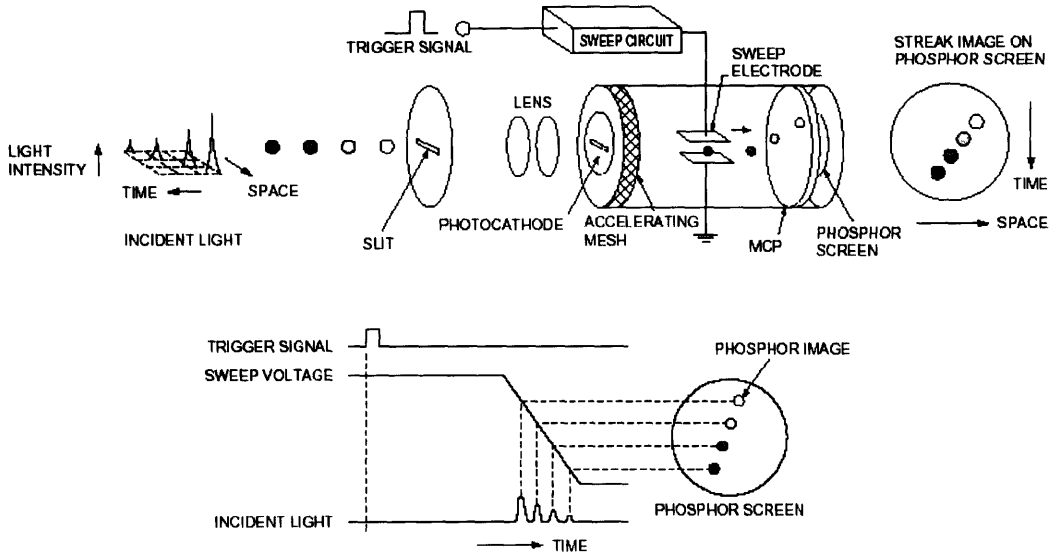

Figure 1-4: Schematic of the operating principle of a streak camera. Picture adapted from http://www.hpk.co.jp/Eng/products/SYSE/pdfs/StreakGuide.pdf

1.3.1 Streak Camera

Perhaps the most widespread and well known bunch length measurement technique involves using a streak camera [26–28]. The use of a streak camera requires the production and imaging of optical radiation from the electron beam. Typically, the optical radiation is produced via Cherenkov or transition radiation, but any type of radiation can be used as long as the radiation mechanism is short compared to the bunch length. The optical pulse is subsequently imaged by the streak camera to obtain the bunch length as shown in Fig. 1-4. The state of the art streak camera from Hamamatsu (FESCA-200), which has a minimum resolution of 200 fs, has been used to measure electron bunches of length 500 fs [29].

However, streak cameras have several disadvantages. Errors in the bunch length measurement can be introduced due to dispersion in the optics, the bandwidth of filters used in the radiation transmission line, and the finite size of the source. Moreover, for very short bunch lengths the synchronization between the camera and the

accelerator RF can further add difficulty to the measurement. Lastly, the streak camera is a relatively expensive (~$100,000) device and typically requires the destruction of the beam to produce the optical pulse.

1.3.2 RF deflecting structures

The use of an RF deflecting structure to measure the bunch length was first demonstrated in 1965 [30, 31]. The RF deflecting technique requires a series of RF accelerating cavities, a magnet/spectrometer and a profile measuring device. Electrons at various positions in the bunch are given a time correlated momentum kick along the longitudinal length of the bunch. The spectrometer then translates the momentum spread into horizontal position spread. The bunch length can then be determined directly from a profile monitor. This technique has been revisited recently with the need to measure ultrashort electron bunches and has been demonstrated to measure 84 fs (rms) bunches [32]. The major disadvantage of this technique is that mixing between the energy and phase distributions may result in an inaccurate measurement of the bunch length.

An RF deflecting technique is concurrently being implemented by Dr. Jake Haimson for the HRC accelerator here at MIT [33] that specifically addresses the mixing problem stated above. This technique passes the electron beam through a circularly polarized beam deflecting RF structure. The bunched beam interacts with two quadrature phased, orthogonally polarized, transverse magnetic deflection fields such that particles of equal energy populating a sequential array of thin slices cut transversely through the bunch will experience identical transverse momenta impulses but at incrementally changing (rotating) radial directions that depend only on the RF phase of the cavity fields at the time of traversal of each slice. Moreover, within each slice, particles having different energies will be deflected in the same radial direction but at different deflection angles. The phase and energy distributions are then displayed in orthogonally separate azimuthal and radial directions as shown in Fig. 1-5. This technique is being tested in parallel with the SPR experiment resulting in a comparison between the two techniques.

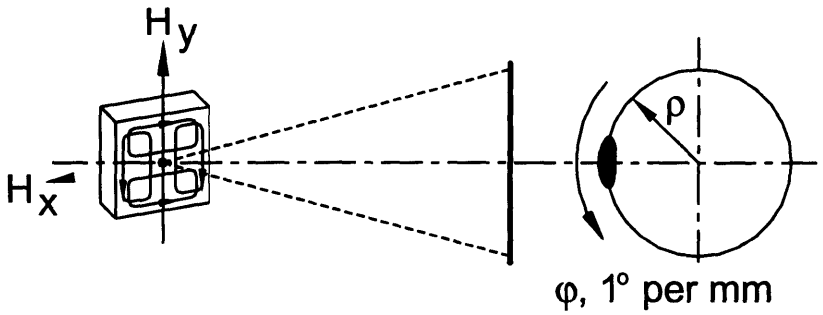

Figure 1-5: Diagram of the HRC RF Deflecting Structure. Adapted from [33].

1.3.3 Laser Techniques

The use of lasers as a means of particle beam characterization was first proposed in 1963 [34, 35]. Recent advances in producing short pulse (100fs), high peak power (TW) lasers has rekindled the idea of using lasers to diagnose electron beams, specifically the longitudinal distribution. There are two techniques that have been demonstrated. The first technique produces 90° Thomson scattering between the electron and laser beams as shown in Fig. 1-6. The resulting x-ray profile as a function of position with respect to the electron beam in space and time produces a transverse and longitudinal beam profile. The Thomson scattering technique has measured 10-15 ps electron bunches [36].

The second method uses an electro-optic crystal which interacts with the wake fields of the electron bunch. The presence of an electric field in the crystal due to the electron bunch at the same time as the laser pulse results in a rotation of the two polarizations of the laser pulse. The direction and degree of the polarization rotation is proportional to the amplitude and phase of the electric field. An experimental setup is shown in Fig. 1-7. Several different analysis techniques of the laser pulse have been implemented in order to retrieve the electron bunch length. Experiments have demonstrated the use of this technique to measure 2 ps and 650 fs electron bunches [37–39].

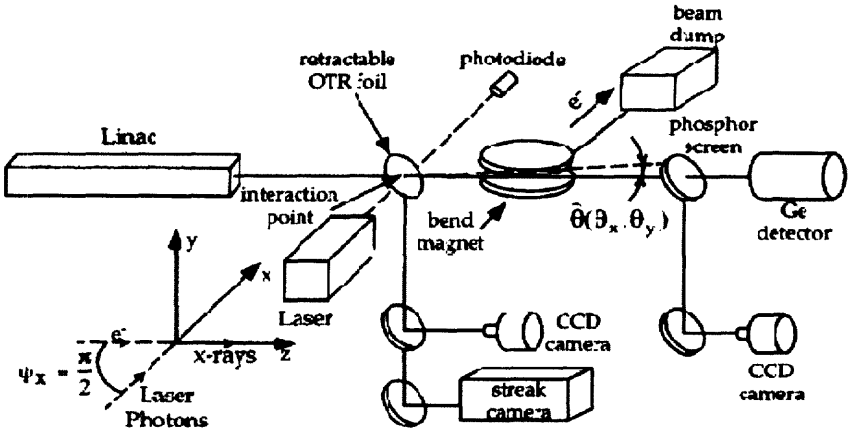

Figure 1-6: Schematic of a Laser Scattering Experiment.

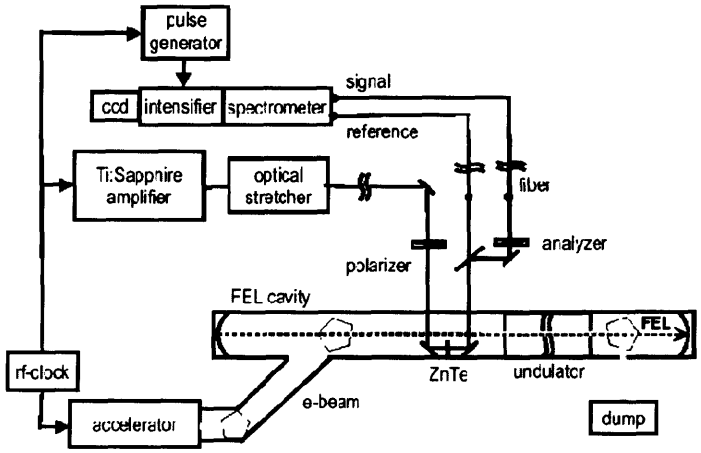

Figure 1-7: Schematic of an Electro-Optic Experiment.

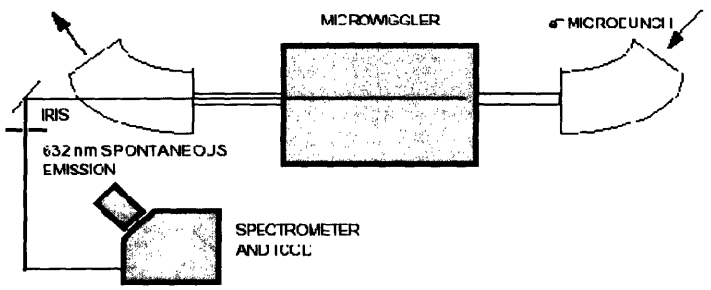

Figure 1-8: Schematic of an Incoherent Radiation Experiment.

1.3.4 Incoherent Radiation

Properties of charged particle bunches can be determined through measurement of fluctuations of incoherent emissions from the bunches [40]. The emissions can be produced by an interaction of the particles with either electromagnetic fields or media as shown in Fig. 1-8. The radiation spectra are composed of random spikes of width $\Delta\omega \sim 1/\tau_b$. This technique has be used to measure 1-5 ps bunches [41].

1.3.5 Coherent Radiation

Another widespread bunch length measurement technique uses the generation of coherent radiation in which the radiation intensity scales as N_e^2, where N_e is the number of electrons in the bunch. The radiation is typically produced via transition or synchrotron radiation mechanisms, however, diffraction, undulator and SP radiation can be utilized. The emitted radiation is only coherent for wavelengths longer than the bunch length and a measurement of the cutoff frequency allows the bunch length to be determined. Typically, the emitted radiation is collected by a Michelson interferometer and an interferogram is produced, which when Fourier transformed gives the radiation spectrum.

Coherent transition radiation bunch length measurements were first demonstrated in [42] and [43] for bunches of length 10 ps and 45 ps, respectively. Coherent

synchrotron radiation has been used to measure bunch lengths of 900 fs [44] and 90 fs - 1 ps [45]. Coherent diffraction radiation has also been used to measure bunches of 600 fs [46] and 450 fs [47].

The use of coherent SPR for a bunch length diagnostic was first proposed by Nguyen and Lampel [9, 10]. Until recently (2002), the bunch length had not been measured via SPR. Doucas, et.al. [48] measured bunches of 14 ps. This experiment demonstrates the use of SPR as a bunch length diagnostic for sub-picosecond electron bunches.

1.4 Terahertz Radiation

Research into the Terahertz (THz), or submillimeter regime, which corresponds to 1 mm to 100 μm (300 GHz to 3 THz), has been ongoing for many years. Located between the microwave and visible and having limited atmospheric propagation there has been little commercial emphasis on THz sources, detectors and other components. Historically, THz technology has been used by spectroscopists and astronomers to measure and catalog thermal emission lines from various molecules. One of the newest applications, THz imaging, utilizes THz radiation for noninvasive medical imaging and the probing of biological materials or electronic parts. THz radiation has several characteristics which make them useful for imaging applications. Terahertz radiation penetrates most dry, nonmetallic and nonpolar materials such as plastics, paper, and nonpolar organic substances. In contrast, metals are completely opaque and polar liquids like water are strongly absorptive. Several articles exist which describe the history and applications of this frequency regime [49, 50].

1.4.1 Sources

Perhaps the most difficult component to realize in the submillimeter regime has been the THz source [50]. Electronic solid-state sources based on semiconductors are limited by reactive parasitics or transit times that cause high-frequency rolloff. Tube sources suffer from physical scaling problems, metallic losses and the need for high

magnetic fields. Optical style sources need to operate at low energy levels of the order of meV which is comparable to the relaxation energy of the crystal.

The most successful techniques have used a frequency conversion technique: up from microwave or down from optical/IR. These sources can typically produce mW power levels. Other techniques that produce narrow-band, μW power levels include: optical mixing in non-linear crystals, photomixing, picosecond laser pulsing, laser sideband generation, quantum cascade lasing, direct semiconductor oscillation, direct lasing of gases, and Josephson junction oscillators.

Recently interesting work has come from the production of coherent THz radiation via ultrashort ($\sim$ 100 fs) near-infrared laser pulses [51]. The THz radiation is produced when the laser pulse hits a semiconductor which then converts the incident pulse into broadband THz radiation. These sources are the basis for THz time domain spectroscopy (THz-TDS) which allows for measurement of both the intensity and phase of the electric field. Many laboratories are now performing THz-TDS experiments and several articles describe the state of the field [52–54].

Short electron bunches ($\lesssim$ 1 ps) have the ability to directly produce high intensity coherent radiation in the THz regime. THz radiation has been generated using electron beams in FEL's and via synchrotron radiation [55–57] and transition radiation [58]. SPR has the inherent advantage of N_g, the number of grating periods, over other radiation mechanisms. This experiment demonstrates the use of SPR to create a high intensity, broadband, frequency selective Terahertz source.

1.4.2 Frequency Locking

The accelerator macropulse has a steady state width of $\sim$40 ns which means there are $>$ 500 bunches in a pulse. Interference between the radiation from periodic electron bunches was first predicted for Cherenkov radiation [59] such that harmonics of the RF frequency would be observed. Interference between bunches has been measured for coherent synchrotron radiation [60] and transition radiation [61]. Researchers have also seen interference in several FEL experiments [62, 63] and an experiment that uses picosecond electron pulses to excite a rectangular waveguide [64]. All of

these experiments except [64] used a Fabry-Perot Interferometer to measure the interference. The resolution in [60] and [63] was 2.7 GHz with an accelerator frequency 2.856 GHz so the interference was just above the observable threshold. The authors in [62] report measuring a linewidth of $< 1.5\%$ for an accelerator operating frequency of 3 GHz. A transform-limited bandwidth of 200 kHz (RF frequency of 2.853 GHz) is reported to be observed by [64] using a microwave spectrum analyzer, although no data were supplied. This experiment uses a double heterodyne receiver to measure the linewidth to 1 part in 10,000 (2 MHz for an RF frequency of 17.14 GHz) of frequency locked SPR (FL-SPR). A transform limited bandwidth at harmonics of the accelerator frequency is demonstrated.

1.5 Thesis Outline

The remainder of this thesis consists of four sections. In Chapter 2 the theory of SPR is developed starting with a general description of the problem for one electron and continuing with a solution of the problem via several different methods. Subsequently, the effects of multiple electrons in a bunch and multiple bunches in a pulse are treated. Lastly, several computer codes are discussed which are used to compute the intensity and distribution of radiation and from which a bunch length is determined. Chapter 3 presents the experimental design and includes a description of the accelerator system in addition to PARMELA simulations of the accelerator. The remainder of the chapter describes the SPR vacuum chamber, designs for several gratings and the radiation detection system. The experimental results including verification of the SPR resonance condition, dependence on beam height and current, bunch length measurements, and measurements of frequency locked SPR are presented in Chapter 4 . Finally, Chapter 5 contains a discussion and the conclusions from this research.

Chapter 2

Smith-Purcell Radiation Theory

2.1 Introduction

Smith-Purcell radiation, which occurs when a charged particle passes over a periodic structure as shown in Fig. 2-1 was first observed in 1953 [1]. Since then, many authors have reported incoherent SPR ranging from the visible to millimeter spectrum [2–6] and coherent SPR in the millimeter regime [7, 8]. The dispersion relation for SPR is a well known relation,

$$n\lambda = l(\frac{1}{\beta} - \cos\theta) \tag{2.1}$$

where λ is the wavelength of the radiation, l is the grating period, n is the order of radiation, β is the ratio of the electron velocity to the speed of light, and θ is the angle of emission. The dispersion relation can be derived by considering the constructive interference that occurs between two successive grating periods as in Fig. 2-2.

There are two widely accepted methods to solving the SPR problem. The first method, the image charge theory, considers the radiation emitted by the surface currents induced on the grating. This radiation mechanism was suggested by Smith and Purcell [1]. More recently Walsh, et.al. developed the image charge theory for a strip grating [65] and Brownell et.al. generalized it for an arbitrary grating profile [66]. The second method, diffracted wave theory, describes SPR as the diffraction

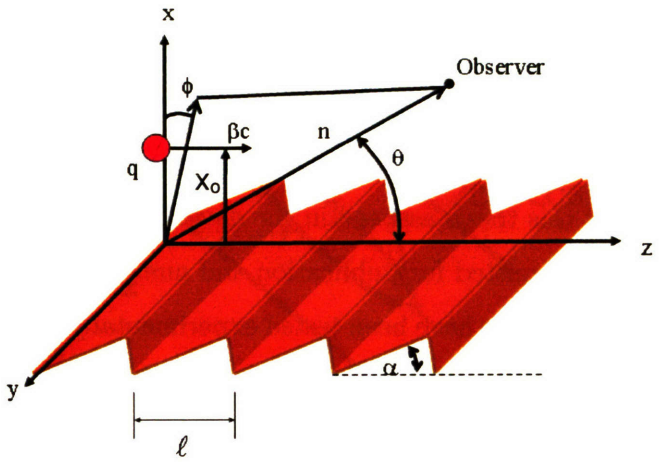

Figure 2-1: Schematic of the Smith-Purcell problem, a charge travelling near a periodic grating structure.

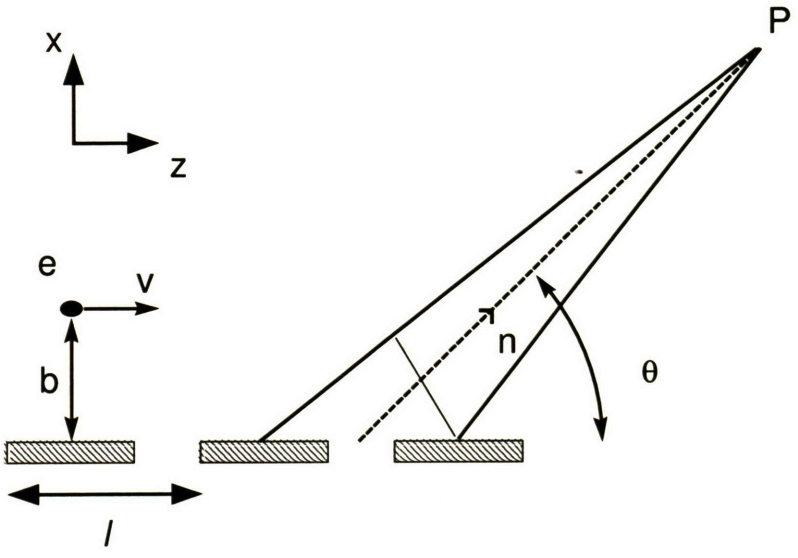

Figure 2-2: Schematic of the interference from successive grating periods.

of evanescent waves in the electron wakefield from the grating. The diffracted wave theory was first derived by Toraldo di Francia [67] who treated the wakefields as Cerenkov radiation. A rigorous solution was obtained by van den Berg [68] who treated the case of a point charge moving parallel to an infinite grating and solved a set of integral equations using a periodic Green's function. Recently, a diffracted wave theory that includes the effects of finite grating size was initiated by Amit Kesar at MIT. The author of this thesis assisted in the development of the theory and is a coauthor on one paper submitted for publication and one paper in preparation.

The validity of both theories have been tested experimentally and very good agreement for the resonance condition and the dependence of the radiation on b, the beam height above the grating was found. A comparison of the theoretical radiated energy to the measured energy has been performed by several groups [2, 4, 8, 48]. Order of magnitude agreement between theory and experiment for both the image charge and diffracted wave theories has been demonstrated. However, the determination of energy typically involves some estimation of losses in the radiation transmission line and when the theories are compared to each other the predicted energy can differ by as much as an order of magnitude. Fortunately, the distribution of the radiated energy agrees reasonably well between the various theories and if the energy is normalized a bunch length can be determined.

The remainder of this chapter develops both the image charge theory and the diffracted wave theories to describe the radiated energy. Except for simple grating geometries, i.e. a strip grating, a calculation of the radiated energy requires a computer. One advantage of the image charge theory is that it can compute the radiated energy very quickly ($\sim$1 s) on a desktop computer. The finite grating diffracted wave theory can take more than 24 hours. Due to the short computation time and the fact that the finite grating diffracted wave theory did not exist at the time, the image charge theory was used to design the gratings for the experiment. The image charge theory could be used to perform a bunch length measurement. However, since the finite grating diffracted wave theory is considered more rigorous, it was used to determine the bunch length from the experimental data. Another advantage of

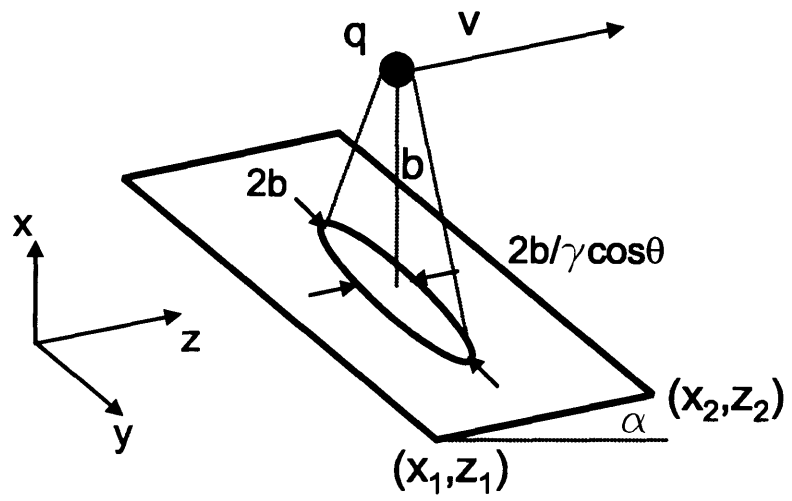

Figure 2-3: Diagram of the footprint of the charge on a grating facet.

the image charge theory is that the equation for the radiated energy can be written such that various dependencies on parameters such as beam height, grating length are transparent.

2.2 Image Charge Model

In the image charge model an electron bunch travels parallel to a periodic grating structure as in Fig. 2-1. The electrons travel at a constant velocity, $\vec{v} = v\hat{z}$ parallel to the grating surface and perpendicular to the planar rule, $\hat{y}$. An image charge is induced on the surface that follows the electrons as in Fig. 2-3. Variations in the surface cause the image charge to accelerate and thus radiate.

In the far field the energy radiated per unit frequency per unit solid angle for a current density $\vec{J}$ is [69]

$$\frac{\partial^2 I}{\partial\omega\partial\Omega} = \frac{\omega^2}{4\pi^2 c^3}\left|\int dt \int d^3\vec{x}\,\hat{n}\times\hat{n}\times\vec{J}(\vec{r},t)e^{i(\omega t-\vec{k}\cdot\vec{r})}\right|^2 \tag{2.2}$$

where $\hat{n} = \hat{x}\sin\theta\cos\phi + \hat{y}\sin\theta\cos\phi + \hat{z}\cos\theta$ is the direction of emission, $\vec{k} = \hat{n}\omega/c$,

c is the speed of light, and ω is the radiation frequency. For a grating that is periodic in z (N_g periods) the total current becomes the sum over the currents in each grating period,

$$\vec{J}(\vec{r},t) = \sum_{m=1}^{N_g} \vec{J}_{tooth}(\vec{x} - ml\hat{z}, t - \frac{ml}{\beta c}). \tag{2.3}$$

Using Eq. (2.3) in Eq. (2.2) and transforming the coordinates to $\vec{r}' = \vec{r} - ml\hat{z}$ and $t' = t - ml/\beta c$ the total energy radiated becomes

$$\frac{\partial^2 I}{\partial\omega\partial\Omega} = \frac{\omega^2}{4\pi^2 c^3}\left|\sum_{m=1}^{N_g} e^{iml\omega(1/v-\hat{n}\cdot\hat{z}/c)}\right|^2 \left|\int dt \int d^3x \hat{n}\times\hat{n}\times\vec{J}_{tooth}(\vec{r},t)e^{i(\omega t-\vec{k}\cdot\vec{r})}\right|^2. \tag{2.4}$$

The term which sums over the grating facets has a well known expression

$$\left|\sum_{m=1}^{N_g} e^{iml\omega(1/v-\hat{n}\cdot\hat{z}/c)}\right|^2 = \frac{\sin^2\left[\omega N_g l/2c\,(1/\beta-\cos\theta)\right]}{\sin^2\left[\omega l/2c\,(1/\beta-\cos\theta)\right]} \quad \begin{matrix} N_g \gg 1 \\ \longrightarrow \end{matrix} \quad \sum_{n\neq 0}\frac{\omega L}{|n|\,l}\delta(\omega-\omega_n) \tag{2.5}$$

which reproduces the Smith-Purcell relationship:

$$\omega_n \equiv \frac{2\pi\,|n|\,c\beta}{l\,(1-\beta\cos\theta)}. \tag{2.6}$$

The expression for the total energy radiated becomes

$$\frac{\partial^2 I}{\partial\omega\partial\Omega} = \frac{\omega^2}{4\pi^2 c^3}\sum_{n\neq 0}\frac{\omega L}{|n|\,l}\delta(\omega-\omega_n)\left|\int dt\int d^3x\hat{n}\times\hat{n}\times\vec{J}_{tooth}(\vec{r},t)e^{i(\omega t-\vec{k}\cdot\vec{r})}\right|^2. \tag{2.7}$$

At this point the expression for the energy radiated is independent of the form of the image current travelling on the grating. Following the literature two different types of gratings, and thus solutions for the image current, will be considered: a strip grating (see Fig. 2-2) and a general grating which is composed of a periodic array of

F infinitely conducting planar facets (see Fig. 2-3).

2.2.1 Image Current

Strip Grating

A closed, analytic solution can be obtained for a strip grating and will be derived first. Consider the well known problem of a charge q a distance b above a perfectly conducting plane. The surface charge is described by

$$\sigma(y,z) = -\frac{1}{4\pi}\frac{2qb}{\left(b^2+y^2+z^2\right)^{3/2}}. \tag{2.8}$$

For a charge trajectory of $\vec{r}(t) = b\hat{x} + \beta ct\hat{z}$ and an infinitely conductive metal, the image charge moves in a similar fashion to the charge. In the relativistic case $t' = \gamma\left(t-\beta cz\right)$, $z' = \gamma\left(z-\beta ct\right)$ and the surface charge $\sigma \rightarrow \gamma\sigma$ because of the Lorentz contraction in z. Additionally, the surface current can be constrained to the surface with a Dirac δ function. The surface current becomes

$$\vec{J}(x,y,z,t) = -\left(\beta c\hat{z}\right)\frac{\delta(x)2q\gamma b/4\pi}{\left[b^2+y^2+\gamma^2\left(z-\beta ct\right)^2\right]^{3/2}}. \tag{2.9}$$

For a strip grating one can assume that the image current is identical to that for an uninterrupted metal plane when the charge is above the strips and zero in the gaps. This can be accomplished with the Heaviside step function such that

$$\begin{aligned} g(z;a,b) &= \Theta(z-a)-\Theta(z-b) \\ &= \begin{cases} 1 & if \quad a<z<b \\ 0 & if \quad z<a \quad or \quad z>b \end{cases}. \end{aligned} \tag{2.10}$$

The strip grating is composed of width d and periodicity l and has N_g strips which are indexed by m, running from 1 to N_g. Thus, the grating is described by

$$g_{tot}(z) = \sum_{m=1}^{N_g} g\left(z;ml,ml+d\right) \tag{2.11}$$

and the total surface current on the strip grating is

$$\vec{J}(x,y,z,t) = -g_{tot}(z)\,(\beta c\hat{z})\,\frac{\delta(x)2q\gamma b/4\pi}{\left[b^2+y^2+\gamma^2\,(z-\beta ct)^2\right]^{3/2}}. \tag{2.12}$$

Comparing Eq. (2.12) to that of the current density from each tooth, Eq. (2.3), gives

$$\vec{J}_{tooth}(\vec{x},t) = -\,(\beta c\hat{z})\,g(z;0,d)\frac{\delta(x)2q\gamma b/4\pi}{\left[b^2+y^2+\gamma^2\,(z-\beta ct)^2\right]^{3/2}}. \tag{2.13}$$

The last term in Eq. (2.7) can be defined as

$$\vec{\mathcal{J}} = \int dt \int d^3\vec{x}\;\hat{n}\times\hat{n}\times\vec{J}_{tooth}e^{i\left(\omega t-\vec{k}\cdot\vec{r}\right)}. \tag{2.14}$$

The cross products reduce to $|\hat{n}\times\hat{n}\times\hat{z}|^2 = |\hat{n}\times\hat{z}|^2 = \sin^2\theta$. Performing the x integration and substituting $\tau = \gamma\,(\beta ct - z)$ gives

$$\begin{aligned}\vec{\mathcal{J}} &= \hat{n}\frac{qb}{2\pi}\sin^2\theta\int_{-\infty}^{\infty}dy\int_{-\infty}^{\infty}dz\int_{-\infty}^{\infty}d\tau\frac{g\,(z;0,d)}{\left(b^2+y^2+\tau^2\right)^{3/2}} \\ &\quad\times e^{\left[\frac{i\omega}{c}\left(\frac{\tau}{\gamma\beta}+\frac{z}{\beta}+y\sin\theta\sin\phi+z\cos\theta\right)\right]}.\end{aligned} \tag{2.15}$$

This equation can be simplified by recognizing the integration over y as that of a modified Bessel function of the second kind [70] such that

$$\begin{aligned}\vec{\mathcal{J}} &= \hat{n}\frac{qb\omega\sin^2\theta\sin\phi}{\pi c}\int_0^s dz e^{\left[\frac{i\omega z}{\beta c}(1-\beta\cos\theta)\right]} \\ &\quad\times\int_{-\infty}^{\infty}d\tau\frac{K_1\left(\left(\frac{\omega}{c}\right)\sin\theta\sin\phi\sqrt{b^2+\tau^2}\right)}{\sqrt{b^2+\tau^2}}\exp^{i\frac{\omega b\tau}{\gamma\beta c}}.\end{aligned} \tag{2.16}$$

The z integration is an integral of an exponential over the interval $[0,d]$. The τ integration gives another modified Bessel function that reduces to the exponential function $K_{1/2}(z) = e^{-z}\sqrt{\frac{\pi}{2z}}$. The total current on each strip becomes

$$\vec{\mathcal{J}} = \frac{2q\beta c}{\omega}\frac{\sin\theta}{1-\beta\cos\theta}\sin\left(\frac{\omega s\left(1-\beta\cos\theta\right)}{2\beta c}\right)e^{-\frac{b}{\lambda_e}} \tag{2.17}$$

where the evanescent length is defined as $\lambda_e \equiv \left[\left(\frac{\omega}{\gamma\beta c}\right)\sqrt{1+\left(\gamma\beta\sin\theta\sin\phi\right)^2}\right]^{-1}$.

Using Eq. (2.17) in Eq. (2.7) gives the total radiated energy per unit frequency and solid angle:

$$\frac{\partial I}{\partial\omega\partial\Omega} = \frac{\omega^2}{4\pi^2c^3}\sum_{n\neq 0}\frac{\omega L}{|n|\,l}\delta\left(\omega-\omega_n\right)\left|\frac{2q\beta c}{\omega}\frac{\sin\theta}{1-\beta\cos\theta}\sin\left(\frac{\omega d\left(1-\beta\cos\theta\right)}{2\beta c}\right)e^{-\frac{b}{\lambda_e}}\right|^2. \tag{2.18}$$

The total radiated energy per solid angle can be determined by integrating over frequency such that

$$\frac{dI}{d\Omega} = \int_0^\infty d\omega\frac{\omega^2}{4\pi^2c^3}\sum_{n\neq 0}\frac{\omega L}{|n|\,l}\delta\left(\omega-\omega_n\right)\left|\frac{2q\beta c}{\omega}\frac{\sin\theta}{1-\beta\cos\theta}\sin\left(\frac{\omega d\left(1-\beta\cos\theta\right)}{2\beta c}\right)e^{-\frac{b}{\lambda_e}}\right|^2$$

$$= \frac{2q^2N}{\pi l}\frac{\beta^3\sin^2\theta}{\left(1-\beta\cos\theta\right)^3}\sum_{n\neq 0}e^{-\frac{4\pi|n|b\sqrt{1+(\gamma\beta\sin\theta\sin\phi)^2}}{\gamma l(1-\beta\cos\theta)}}\sin^2\left(\frac{d\pi\,|n|}{l}\right). \tag{2.19}$$

The last term in Eq. (2.19) is the dependence on the particular grating geometry. The term $\sin^2\left(\frac{d\pi|n|}{l}\right)$ is valid for a strip grating and is different for other types of gratings.

General Surface

The surface current for a generalized surface can also be developed. Consider an electron travelling above an arbitrary grating tooth as in Fig. 2-3. The grating profile is composed of F planar facets where the f^{th} facet extends from $\{x_{1f}, z_{1f}\}$ to $\{x_{2f}, z_{2f}\}$ and the grating is infinite in the y plane. Note that $z_{2f} - z_{11} \leq l$ and we will assume that facets are not inverted or covered, $z_{1f} \leq z_{2f} \leq z_{1f+1}$. The angle of each facet is $\alpha = \tan^{-1}\left[\frac{x_{2f}-x_{1f}}{z_{2f}-z_{1f}}\right]$. The current density for a single tooth is

$$\overrightarrow{J}_{tooth} = \sum_{f=1}^{F} \overrightarrow{\rho}\left(\overrightarrow{r}, t, s_f\right) v\left(\overrightarrow{r}, t, s_f\right) \tag{2.20}$$

where ρ and v are the image charge density and velocity and s_f is the set $\{x_{1f}, z_{1f}, x_{2f}, z_{2f}\}$. The image charge model assumes that the total image charge can be described by a linear superposition of the images due to a single electron and that the image charge on each facet equals that for an infinite conducting planar surface which was described in the previous section.

Similar to the strip grating case, a relativistic electron travelling with a velocity $\overrightarrow{v} = v\widehat{z}$ travelling above a conducting plane defined by $\tan\alpha = \frac{x_2 - x_1}{z_2 - z_1}$ induces an image charge which is proportional to the normal component of the electric field such that the charge density is

$$\begin{aligned} \overrightarrow{\rho}\left(\overrightarrow{r}, \overrightarrow{r}_o, t, s\right) &= -\frac{q\gamma}{2\pi} \frac{\left|(x - x_0)\cos\alpha - (z - z_o - vt)\sin\alpha\right|}{\left[(x - x_o)^2 + (y - y_o)^2 + \gamma^2 (z - z_o - vt)^2\right]^{3/2}} \\ &\quad \times\delta\left[(z - z_1)\sin\alpha - (x - x_1)\cos\alpha\right] \end{aligned} \tag{2.21}$$

where q is the electron charge and $\overrightarrow{r}_o = (x_o, y_o, z_o)$ is the charge position at $t = 0$.

In order to derive an expression for the image charge velocity consider that the image charge becomes a point when the electron intercepts the facet at time $t' = \left[z_1 - z_o + (x_1 - x_o)\cot\alpha\right]/v$ and since the electric field lines are radial the charge distribution scales with the distance of the electron from the surface. Thus the velocity of each image charge is the distance to the intersecting point divided by the transit time,

$$\overrightarrow{v}\left(\overrightarrow{r}, \overrightarrow{r}_o, t, s\right) = \frac{\widehat{x}\,(x_o - x) + \widehat{y}\,(y_o - y) + \widehat{z}\,(z_o + vt' - z)}{(t' - t)}. \tag{2.22}$$

The image current density within a single tooth becomes

$$\vec{J}_{tooth} = \sum_{f=1}^{F} \int_{-\infty}^{\infty} dt \int_{z_1}^{z_2} dz \int_{-\infty}^{\infty} dy \int_{-\infty}^{\infty} dx \rho\left(\vec{r}, \vec{r}_o, t, s\right) \vec{v}\left(\vec{r}, \vec{r}_o, t, s\right) \quad (2.23)$$

$$= -\frac{q\gamma}{2\pi} \sum_{f=1}^{F} \int_{z_1}^{z_2} dz \int_{-\infty}^{\infty} d\overline{y} \int_{-\infty}^{\infty} du \frac{(\widehat{x}\tan\alpha + \widehat{z}) \pm \widehat{y}\overline{y}\tan\alpha}{\left[d^2 + \overline{y}^2 + \gamma^2 u^2\right]^{3/2}}$$
$$\times e^{i[\omega(u-z_o)/v + k_y(\overline{y}-y_o) + \kappa z]} e^{-ik_x(x_1 - z_1\tan\alpha)} \quad (2.24)$$

where $u \equiv vt - z - z_o$, $\overline{y} \equiv y_o - y$, $d \equiv |x_1 - x_o + (z - z_1)\tan\alpha|$, and $\kappa \equiv \omega/v - k_z - k_x \tan\alpha$. The upper sign in Eq. (2.24) is chosen if the electron is above the facet (x_1, $x_2 \leq x_o$), the lower sign if the electron is below the facet (x_1, $x_2 \geq x_o$). Using [70] the current density on each tooth can be reduced to

$$\vec{J}_{tooth} = \sum_{f=1}^{F} -qle^{\mp\frac{b}{\lambda_e}} e^{-i(k_y y_o + \omega z_o/v)} \vec{G}\left(\omega, \widehat{n}, s\right) \quad (2.25)$$

where

$$\vec{G}\left(\omega, \widehat{n}, s\right) \equiv (\widehat{x}\tan\alpha \pm \widehat{y}i2k_y\lambda_e\tan\alpha + \widehat{z}) \quad (2.26)$$
$$\times \frac{e^{(\pm 1/\lambda_e - ik_x)(x_1 - z_1\tan\alpha)}}{(\pm\tan\alpha/\lambda_e + i\kappa)\, l} e^{(\pm\tan\alpha/\lambda_e + i\kappa)z} \Big|_{z_1}^{z_2}.$$

The expression for the total radiated energy per unit frequency and solid angle becomes

$$\frac{\partial I}{\partial\omega\partial\Omega} = \frac{\omega^2}{4\pi^2 c^3} \sum_{m=1}^{N} \frac{\omega L}{|m|\, l} \delta\left(\omega - \omega_m\right) \left| \widehat{n} \times \widehat{n} \times \sum_{f=1}^{F} \left(-qle^{\mp\frac{b}{\lambda_e}} e^{-i(k_y y_o + \omega z_o/v)}\right) \vec{G} \right|^2 \quad (2.27)$$

$$= \sum_{m=1}^{N} \frac{q^2 Ll}{4\pi^2 c^3} e^{\mp\frac{2b}{\lambda_e}} \delta\left(\omega - \omega_m\right) \left| \widehat{n} \times \widehat{n} \times \sum_{f=1}^{F} \vec{G} \right|^2. \quad (2.28)$$

If the special case of a strip grating with strips of width d separated by length l

is considered integrating Eq. (2.28) over frequency gives the same result as in Eq. (2.19). Eq. (2.28) readily shows that the radiated energy scales as the total length of the grating (i.e. N_g). Additionally the exponential dependence of the radiation on the beam height, b, is seen. Lastly, the final factor $\left|\widehat{n} \times \widehat{n} \times \sum_{f=1}^{F} \overrightarrow{G}\right|$ is typically called a grating efficiency factor and is a function of the grating profile and wavelength of radiation.

2.3 Diffraction of Plane Waves

The theory of diffraction of plane-waves was first developed by Toraldo di Francia [67] and adapted for the case of SPR by van den Berg [68]. Van den Berg uses an integral method [71, 72] in the first complete solution of the SP problem. Van den Berg computes the reflected electric and magnetic fields from an infinite grating by developing a set of two integral equations for the electric and magnetic fields. The radiated energy is subsequently computed by calculation of the Poynting vector. The van den Berg approach is generally followed in much of the literature [8, 73] and is considered to be a rigorous solution. The increase in computing power has enabled the ability to solve the SPR problem with increasing precision.

An integral method similar to van den Berg's was developed by Kesar [74, 75] with the collaboration of the author. The new theory takes into account the effects of the finite size of the grating. The far field radiation is computed after finding the surface current by solving an integral equation for the electric field. The van den Berg approach for infinite gratings will first be described, followed by the Kesar approach for finite gratings. Since the van den Berg approach is considered rigorous it was used to benchmark the 3D theory in the infinite grating limit.

2.3.1 Electric and Magnetic Field Integral Equations

Consider a point charge travelling in free space, which produces the field incident upon the grating, $E^i = E^i(x, y, z, t)$ and $H^i = H^i(x, y, z, t)$. The electric and magnetic fields can be describe as Fourier integrals such that

$$\vec{E}^i(x,y,z,t) = \frac{1}{(2\pi)^2}\int_{-\omega}^{\omega} d\omega \int_{-\infty}^{\infty} \vec{\mathcal{E}}^i(x,z;k_y,\omega)e^{(ik_y y - i\omega t)}dk_y \quad (2.29a)$$

$$\vec{H}^i(x,y,z,t) = \frac{1}{(2\pi)^2}\int_{-\omega}^{\omega} d\omega \int_{-\infty}^{\infty} \vec{\mathcal{H}}^i(x,z;k_y,\omega)e^{(ik_y y - i\omega t)}dk_y. \quad (2.29b)$$

These can be rewritten as

$$\vec{E}^i(x,y,z,t) = \frac{1}{2\pi}\,\mathrm{Re}\left[\int_{0}^{\omega} d\omega \int_{-\infty}^{\infty} \vec{\mathcal{E}}^i(x,z;k_y,\omega)e^{(ik_y y - i\omega t)}dk_y\right] \quad (2.30a)$$

$$\vec{H}^i(x,y,z,t) = \frac{1}{2\pi}\,\mathrm{Re}\left[\int_{0}^{\omega} d\omega \int_{-\infty}^{\infty} \vec{\mathcal{H}}^i(x,z;k_y,\omega)e^{(ik_y y - i\omega t)}dk_y\right] \quad (2.30b)$$

since E^i and H^i are real and only positive frequencies are considered. The Fourier components satisfy Maxwell's equations:

$$(\nabla + ik_y\hat{y}) \times \vec{\mathcal{H}}^i + i\omega\epsilon_o \vec{\mathcal{E}}^i = \vec{\mathcal{J}} \quad (2.31a)$$

$$(\nabla + ik_y\hat{y}) \times \vec{\mathcal{E}}^i - i\omega\mu_o \vec{\mathcal{H}}^i = 0 \quad (2.31b)$$

where $\nabla = \partial_x\hat{x} + \partial_z\hat{z}$ and $\vec{\mathcal{J}}$ is the Fourier transform of the current density,

$$\vec{\mathcal{J}}(x,z;k_y,\omega) = \int_{-\infty}^{\infty} dt \int_{-\infty}^{\infty} \vec{J}(x,y,z,t)e^{(ik_y y - i\omega t)}dy. \quad (2.32)$$

A charge, q, moving with velocity $\vec{v} = v\hat{z}$ at the position $y = 0$, $x = b$ produces a current density that can be written as

$$\vec{J}(x,y,z,t) = qv\delta(x-b, y, z-vt)\,\hat{z} \quad (2.33)$$

The Fourier transform of the current becomes

$$\vec{\mathcal{J}}(x,z;k_y,\omega) = qe^{ik_z z}\delta(x-b)\,\hat{z} \quad (2.34)$$

where $k_z \equiv \omega/v = k/\beta$. Note that $\vec{J}(x,z;k_y,\omega)$ is independent of k_y and only has a z component. Using Eqs. (2.31a) and (2.31b) the x and z components of $\vec{E}^i$ and $\vec{H}^i$ can be expressed in terms of $\mathcal{E}_y^i$ and $\mathcal{H}_y^i$. The y components of the electric and magnetic fields can then be written as

$$\begin{aligned} \partial_x^2\mathcal{E}_y^i + \partial_z^2\mathcal{E}_y^i + k_\perp^2\mathcal{E}_y^i &= (\mu_o/\epsilon_o)^{1/2}(k_y/k)\,\partial_z\mathcal{J}_z \\ \partial_x^2\mathcal{H}_y^i + \partial_z^2\mathcal{H}_y^i + k_\perp^2\mathcal{H}_y^i &= \partial_x\mathcal{J}_z \end{aligned} \tag{2.35}$$

where $k_\perp^2 \equiv k^2 - k_y^2$. The solutions of Eqs. (2.35) using the current density, Eq. (2.34), are

$$\mathcal{E}_y^i(x,z;k_y,\omega) = \frac{1}{2}q\left(\frac{\mu_o}{\epsilon_o}\right)^{1/2}\left(\frac{k_y}{k}\right)\left(\frac{k_z}{k_x}\right)e^{ik_z z + ik_x|x-b|} \tag{2.36a}$$

$$\mathcal{H}_y^i(x,z;k_y,\omega) = -\frac{q}{2}sgn(x-b)e^{ik_z z + ik_x|x-b|} \tag{2.36b}$$

where

$$k_x = i\left(k_z^2 + k_y^2 - k^2\right)^{1/2} \qquad \text{and} \qquad \left(k_z^2 + k_y^2 - k^2\right) \geq 0. \tag{2.37}$$

Since $v < c$ and $k_z > k$, k_x is imaginary and the solutions are evanescent waves that decay exponentially away from the particle.

In the presence of a reflecting grating the evanescent waves can be diffracted and become propagating plane waves. These propagating waves are the Smith-Purcell radiation. The total field above the grating can be described using the incident and reflected fields such that

$$E^r \equiv E - E^i \qquad \text{and} \qquad H^r \equiv H - H^i. \tag{2.38}$$

The reflected fields can also be represented as Fourier integrals and the Fourier components satisfy the source free electromagnetic field equations

$$(\nabla + ik_y\hat{y}) \times \vec{\mathcal{H}}^r + i\omega\epsilon_o \vec{\mathcal{E}}^r = 0 \quad (2.39a)$$

$$(\nabla + ik_y\hat{y}) \times \vec{\mathcal{E}}^r - i\omega\mu_o \vec{\mathcal{H}}^r = 0. \quad (2.39b)$$

Moreover, the total fields must satisfy the boundary condition on the surface S of the grating such that

$$\hat{n} \times (\vec{\mathcal{E}}^i + \vec{\mathcal{E}}^r) = 0. \quad (2.40)$$

Two fundamental cases arise: E polarization and H polarization. For the E polarization case, where $E_y \neq 0$ and $H_y = 0$, E_y^r satisfies

$$\partial_x^2 \mathcal{E}_y^r + \partial_z^2 \mathcal{E}_y^r + k_\perp^2 \mathcal{E}_y^r = 0 \quad (2.41)$$

with the boundary condition $E_y = 0$ on the surface of the grating. For the H polarization case, where $H_y \neq 0$ and $E_y = 0$, H_y^r satisfies

$$\partial_x^2 \mathcal{H}_y^r + \partial_z^2 \mathcal{H}_y^r + k_\perp^2 \mathcal{H}_y^r = 0 \quad (2.42)$$

with the boundary condition $n \cdot \bigtriangledown H_y = 0$ on the surface.

The reflected field above the grating can be represented as a Rayleigh expansion of propagating and evanescent waves,

$$E_y^r(x, z; k_y, \omega) = \sum_{n=-\infty}^{\infty} E_{y,n}^r(k_y, \omega) e^{i(k_z z + k_x x)} \quad (2.43)$$

$$H_y^r(x, z; k_y, \omega) = \sum_{n=-\infty}^{\infty} H_{y,n}^r(k_y, \omega) e^{i(k_z z + k_x x)}$$

where $k_{zn} = k_{zo} + 2\pi n/l$ and $k_{xn} = \left(k^2 - k_{zn}^2 - k_y^2\right)^{1/2}$. SPR is the sum of all the propagating waves, which have $\mathrm{Im}(k_{xn}) = 0$, such that $k_{zn}^2 + k_y^2 = k^2$. The emission angles (θ, ϕ) of the SPR are related to k_{zn}, k_y, and k_{xn}, by

$$k_{zn} = k\cos(\theta_n) \tag{2.44}$$

$$k_y = k\sin(\theta_n)\sin(\phi_n) \tag{2.45}$$

$$k_{xn} = k\sin(\theta_n)\cos(\phi_n). \tag{2.46}$$

Using $\lambda_o = \frac{2\pi}{k_o}$, $k_{zn} = k_{zo} + 2\pi n/l$, and Eq. (2.44) the Smith-Purcell relationship can be reproduced:

$$-n\lambda_o = l\left(1/\beta - \cos(\theta_n)\right). \tag{2.47}$$

To find the intensity of the SPR the coefficients $E^r_{y,n}$ and $H^r_{y,n}$ in Eqs. (2.43) must be calculated. An integral representation for the electric and magnetic fields using Green's theorem is found. The Green's function is chosen such that on the surface S only $n\cdot\bigtriangledown H_y$ or E_y contribute. Additionally, the Green's function must be composed of waves travelling in the x direction. The Green's function is then

$$G(x,z,k_y,\omega) = \sum_{n=-\infty}^{\infty} \frac{i}{2k_{xn}l} e^{ik_{zn}(z_p-z)+ik_{xn}|x_p-x|}. \tag{2.48}$$

The $E^r_{y,n}$ and $H^r_{y,n}$ coefficients are then functions of the total field at the surface of the grating

$$E^r_{y,n} = \frac{i}{2k_{xn}l}\int_s (n\cdot\bigtriangledown E_y)\, e^{-ik_{zn}z-ik_{xn}x} ds \tag{2.49a}$$

$$H^r_{y,n} = \frac{i}{2k_{xn}l}\int_s H_y\,(n\cdot\bigtriangledown)\, e^{-ik_{zn}z-ik_{xn}x} ds. \tag{2.49b}$$

The path of integration s is on the grating surface and for grating period. (x_p, z_p) is on s. Applying Green's theorem gives the following equations of the second kind [68]

$$\begin{aligned} \frac{1}{2} n_p \cdot \nabla_p E_y(x_p, z_p) + P \int_L (n \cdot \nabla E_y)\,(-n_p \cdot \nabla_p G)\, ds &= n_p \cdot \nabla_p E_y^i(x_p, z_p) \\ \frac{1}{2} H_y(x_p, z_p) + P \int_L (n \cdot \nabla G)\, ds &= H_y^i(x_p, z_p) \end{aligned} \tag{2.50}$$

where P denotes the Cauchy principal value of the integral. The set of integral equations, Eqs. (2.50), are solved by discretizing the unknown functions $n \cdot \nabla E_y$ and H_y into N points on the surface, leading to a matrix equation of order N.

The energy of the radiated SPR is calculated from the Poynting vector of the reflected fields. The energy lost by a single electron when traversing one grating period is the sum of the x components of the Poynting vector integrated over all ω and k_x [73]:

$$\frac{dI}{d\Omega} = \frac{e^2}{D\varepsilon_o} \sum_n \frac{\sin^2\theta \cos^2\phi}{\left(\frac{1}{\beta} - \cos\theta\right)^3} \left|R_n\left(\eta, \theta, \phi\right)\right|^2 e^{-\frac{2b}{\lambda_e}}. \tag{2.51}$$

The radiation factors $|R_n|^2$ correspond to the classical reflection coefficients of a grating and are given by [68]

$$\left|R_n\left(k_y, \theta, \phi\right)\right|^2 = \frac{4}{e^2} e^{2k_{xo}b} \left\{ \frac{\varepsilon_o}{\mu_o} \left|E_y^r\right|^2 + \left|H_y^r\right|^2 \right\} \left(1 - \sin^2\theta \sin^2\phi\right)^{-1}. \tag{2.52}$$

2.3.2 Electric Field Integral Equation

The electric field integral equation method is a new approach developed by Kesar [74, 75] with the collaboration of the author. The method entails determining the surface current from the incident electric field and then calculating the far field radiation due to that surface current. For a charge travelling above a grating as in Fig. 2-1, the electric and magnetic fields incident on the grating can be written as

$$\vec{E}^i(x,y,z,t) = \frac{q\gamma}{4\pi\varepsilon_o}\frac{\widehat{x}(x-x_o)+\widehat{y}(y-y_o)+\widehat{z}(z-z_o-vt)}{[(x-x_o)^2+(y-y_o)^2+\gamma^2(z-z_o-vt)^2]^{3/2}} \quad (2.53a)$$

$$\vec{H}^i(x,y,z,t) = \frac{q\gamma v}{4\pi}\frac{\widehat{y}(x-x_o)+\widehat{x}(y-y_o)}{[(x-x_o)^2+(y-y_o)^2+\gamma^2(z-z_o-vt)^2]^{3/2}}. \quad (2.53b)$$

Assuming an $e^{i(\omega t-\vec{k}\cdot\vec{r})}$ dependence the temporal Fourier transform can be written as

$$\mathcal{E}^i(x,z;y,\omega) = \int_{-\infty}^{\infty} E^i(t)e^{-i\omega t}dt \quad (2.54a)$$

$$= \frac{e\gamma}{4\pi\varepsilon_o}e^{-ik_z(z-z_o)}\left[\int_{-\infty}^{\infty}\frac{\gamma\widehat{x}(x-x_o)+\gamma\widehat{y}(y-y_o)}{[\rho^2+\tau^2]^{3/2}}\cos\left(\frac{k_z}{\gamma}\tau\right)d\tau + i\int_{-\infty}^{\infty}\frac{\widehat{z}\tau}{[\rho^2+\tau^2]^{3/2}}\sin\left(\frac{k_z}{\gamma}\tau\right)d\tau\right] \quad (2.54b)$$

where $\rho^2 \equiv (x-x_o)^2+(y-y_o)^2$ and $\tau \equiv \gamma(vt+z_o-z)$. Using [70] (17.33-9 and 17.34-10), Eq. (2.54b) can be rewritten as

$$\mathcal{E}^i(x,z;y,\omega) = \frac{e}{2\pi\varepsilon_o\gamma\beta c}\frac{k}{\beta}e^{-ik_z(z-z_o)}\left[\frac{\widehat{x}(x-x_o)+\widehat{y}(y-y_o)}{\rho}K_1\left(\frac{k_z}{\gamma}\rho\right) + i\frac{\widehat{z}}{\gamma}K_o\left(\frac{k_z}{\gamma}\rho\right)\right] \quad (2.55)$$

where K_1 and K_0 are the modified Bessel functions of the second kind. The spatial Fourier transform becomes

$$\mathcal{E}^i(x,z;k_y,\omega) = \int E^i(x,z,y;\omega)e^{ik_y y}dy \tag{2.56a}$$

$$= \frac{e}{2\varepsilon_o\beta c}e^{-i(k_z(z-z_o)-k_y y_o+k_a|x-x_o|)}\left[\pm\hat{x}+\hat{y}\frac{k_y}{k_a}+i\hat{z}\frac{k_z}{\gamma^2 k_a}\right] \tag{2.56b}$$

where $k_a^2 \equiv \left(\frac{k_z}{\gamma}\right)^2 + k_y^2$. For an electron travelling above the grating the (-) in Eq. (2.56b) is chosen.

The vector potential is

$$\vec{A}(\vec{r}) = \int\int\int \vec{J}(\vec{r}\,')\frac{e^{-ik|\vec{r}-\vec{r}\,'|}}{4\pi|\vec{r}-\vec{r}\,'|}d\vec{r}\,' \tag{2.57a}$$

$$= \int\int_{s'} \vec{J}(s',y')\,G^{3D}(\vec{r}-\vec{r}\,')ds'dy' \tag{2.57b}$$

where $\vec{J}$ is the surface current density and the integration is over the grating surface, s. The reflected electric field can be computed from the vector potential,

$$\vec{E}^r = \frac{\nabla\nabla\cdot\vec{A}+k^2\vec{A}}{i\omega\varepsilon_o} = -i\frac{Z_o}{k}\left(\nabla\nabla\cdot\vec{A}+k^2\vec{A}\right) \tag{2.58}$$

which gives the electric field components

$$E_x^r = \left(-i\frac{Z_o}{k}\right)\int\int\left[J_x\partial_{xx}G+J_y\partial_{xy}G+J_z\partial_{xz}G+J_xk^2G\right]ds'dy' \tag{2.59a}$$

$$E_y^r = \left(-i\frac{Z_o}{k}\right)\int\int\left[J_x\partial_{yx}G+J_y\partial_{yy}G+J_z\partial_{yz}G+J_yk^2G\right]ds'dy' \tag{2.59b}$$

$$E_z^r = \left(-i\frac{Z_o}{k}\right)\int\int\left[J_x\partial_{zx}G+J_y\partial_{zy}G+J_z\partial_{zz}G+J_zk^2G\right]ds'dy'. \tag{2.59c}$$

The boundary condition for the electric field on the surface is

$$E_{\|} = E^i + E^r = 0 \tag{2.60}$$

such that

$$E^i_{s\|} = -E^r_{s\|} \tag{2.61a}$$

$$E^i_y = -E^r_y. \tag{2.61b}$$

The components of the surface current and electric field are

$$J_x = J_s \sin\alpha' \qquad \text{and} \qquad J_z = J_s \cos\alpha' \tag{2.62}$$

and

$$E^i_s = E^i_x \sin\alpha + E^i_z \cos\alpha.$$

Using Eq. (2.62) the incident electric field on the surface can then be written as

$$\begin{aligned} E^i_{s\|} = i\frac{Z_o}{k}\Bigg\{ & \sin\alpha \int_{s'}\int_{y'} ds'dy' J_s \sin\alpha' \partial_{xx}G + J_y \partial_{xy}G + J_s \cos\alpha' \partial_{xz}G + J_s \sin\alpha' k^2 G \\ & + \cos\alpha \times \\ & \int_{s'}\int_{y'} ds'dy' J_s \sin\alpha' \partial_{zx}G + J_y \partial_{zy}G + J_s \cos\alpha' \partial_{zz}G + J_s \cos\alpha' k^2 G \Bigg\} \end{aligned} \tag{2.63}$$

$$E^i_y = i\frac{Z_o}{k}\int_{s'}\int_{y'} \left[J_s \sin\alpha' \partial_{yx}G + J_y \partial_{yy}G + J_s \cos\alpha' \partial_{yz}G + J_y k^2 G\right] ds'dy'. \tag{2.64}$$

Applying a spatial Fourier transform to both sides gives

$$\begin{aligned}\mathcal{E}^i_{s\|}(x,z;k_y,\omega) &= i\frac{Z_o}{k}\left\{\int_{s'} ds'\times\right. \\ &\mathcal{J}_s\left[k^2\cos(\alpha-\alpha')+\cos a\cos\alpha'\partial_{zz}+\sin\alpha\sin\alpha'\partial_{xx}+\sin(\alpha-\alpha')\,\partial_{xz}\right]\mathcal{G} \\ &\left.-ik_y\int_{s'} ds'\mathcal{J}_y\left(\partial_x+\partial_z\right)\mathcal{G}\right\} \qquad (2.65)\end{aligned}$$

and

$$\mathcal{E}^i_y(x,z;k_y,\omega) = i\frac{Z_o}{k}\left\{\int_{s'} ds'\mathcal{J}_s\left(-ik_y\right)\left(\cos\alpha'\partial_z+\sin\alpha'\partial_x\right)\mathcal{G}+\int_{s'} ds'\mathcal{J}_y k_\perp^2\mathcal{G}\right\} \qquad (2.66)$$

where the grating has been assumed to have a width $2w$ which is wide enough such that $\int_{-w}^{w}\approx\int_{-\infty}^{\infty}$. Eqs. (2.65) and (2.66) can then be written in matrix form

$$\begin{bmatrix}\mathcal{E}^i_{s\|}\\ \mathcal{E}^i_y\end{bmatrix} = \begin{bmatrix}\mathcal{Z}^1_{mn} & \mathcal{Z}^2_{mn}\\ \mathcal{Z}^3_{mn} & \mathcal{Z}^4_{mn}\end{bmatrix}\begin{bmatrix}\mathcal{J}_{sn}\\ \mathcal{J}_{yn}\end{bmatrix} \qquad (2.67)$$

where the elements $\mathcal{Z}_{mn}$ are defined as

$$\begin{aligned}\mathcal{Z}^1_{mn} &= i\frac{Z_o}{k}\int_{s'} ds'\left[k^2\cos(\alpha-\alpha')+\cos a\cos\alpha'\partial_{zz}+\sin\alpha\sin\alpha'\partial_{xx}+\sin(\alpha-\alpha')\,\partial_{xz}\right]\mathcal{G}\\ \mathcal{Z}^2_{mn} &= \frac{Z_o}{k}\int_{s'} ds' k_y\left(\partial_x+\partial_z\right)\mathcal{G}\\ \mathcal{Z}^3_{mn} &= \frac{Z_o}{k}\int_{s'} ds' k_y\left(\cos\alpha'\partial_z+\sin\alpha'\partial_x\right)\mathcal{G}\\ \mathcal{Z}^4_{mn} &= i\frac{Z_o}{k}\int_{s'} ds' k_\perp^2\mathcal{G}\end{aligned}$$

The 2D Green's function is $\mathcal{G} = \frac{1}{4i}H_o^{(2)}\left(k_\perp\sqrt{(x-x')^2+(z-z')^2}\right)$. The matrix equation is solved computationally to obtain values for the surface current. Once the surface current is obtained it can be substituted into the far field ($r \gg r'$) vector potential

$$\vec{A}(\vec{r}) \approx \frac{e^{-ikr}}{4\pi r}\int_{s'}\int_{-w}^{w}\vec{J}(s',y')e^{i\vec{k}\cdot\vec{r}'}dy'ds' \tag{2.68a}$$

$$\approx \frac{e^{-ikr}}{4\pi r}\int_{s'}\vec{\mathcal{J}}(s',k_y)e^{i(k_x x'+k_z z')}ds'. \tag{2.68b}$$

The magnetic component of the far field radiation is

$$\vec{H}(r,\theta,\omega) = \nabla \times \vec{A} \tag{2.69}$$

and the power spectrum is

$$P_s(\theta,\omega) = Z_o r^2 \left|\vec{H}\right|^2. \tag{2.70}$$

The angular distribution of the average radiated energy per groove per meter is given by Parseval's Theorem,

$$E_{AV}(\theta,\phi) = \frac{1}{N_g \pi}\int_0^\infty P_s(\omega,\theta)\,d\omega. \tag{2.71}$$

Eq. (2.71) shows that the radiated energy travels with the radiated magnetic field due to the surface current induced by the incident electric field.

2.4 Coherence Effects

2.4.1 Single Bunch

The effect of multiparticle coherence was first considered in [76] and was further generalized in [77]. For N_e electrons in a bunch the radiated energy can be considered by summing the electric field of each electron such that Eq. (2.2) becomes

$$\frac{\partial^2 I}{\partial\omega\partial\Omega} = \frac{e^2\omega^2}{4\pi^2 c}\left|\int dt \sum_{j=1}^{N_e}\hat{n}\times\hat{n}\times\vec{\beta}_j(\vec{r},t)e^{i(\omega t-\vec{k}\cdot\vec{r}_j)}\right|^2 \tag{2.72}$$

where β_j is the ratio of the electron velocity to the speed of light and r_j is the position for the jth particle. If β_j is assumed to be the same for all particles and the center of mass of the bunch is described by $\vec{r}(t)$. Eq. (2.72) can be rewritten as

$$\frac{\partial^2 I}{\partial\omega\partial\Omega} = \frac{e^2\omega^2}{4\pi^2 c}\left|\sum_{j=1}^{N_e} e^{i\omega r_j/\beta c}\right|^2 \left|\int dt\hat{n}\times\hat{n}\times\vec{\beta}(\vec{r},t)e^{i(\omega t-\vec{k}\cdot\vec{r}(t))}\right|^2 \tag{2.73}$$

where r_j refers to the particle position with respect to the center of mass. Further assume that the particles are travelling with $\beta \approx 1$. This equation is identical to Eq. (2.2) except for the summation over the particle positions,

$$T(\omega) = \left|\sum_{j=1}^{N_e} e^{i\omega r_j/c}\right|^2. \tag{2.74}$$

This can be rewritten as

$$T(\omega) = \sum_{j=1}^{N_e} e^{i\omega r_j/c}\sum_{k=1}^{N_e} e^{i\omega r_k/c} \tag{2.75}$$

and can be further simplified to

$$T(\omega) = \sum_{j=1(j=k)}^{N_e} e^{i\omega(r_j-r_k)/c} + \sum_{j,k=1(j\neq k)}^{N_e} e^{i\omega(r_j-r_k)/c} = N + \sum_{j,k=1(j\neq k)}^{N_e} e^{i\omega(r_j-r_k)/c}. \tag{2.76}$$

Eq. (2.76) can be rewritten as

$$T(\omega) = N_e + N_e(N_e-1)f(\omega), \tag{2.77}$$

where $f(\omega)$ is defined as

$$f(\omega) \equiv \frac{1}{N_e(N_e-1)}\sum_{j,k=1(j\neq k)}^{N_e} e^{i\omega(r_j-r_k)/c}. \tag{2.78}$$

The total radiated energy can be rewritten as

$$\left(\frac{\partial^2 I}{\partial\omega\partial\Omega}\right)_{N_e} = [N_e + N_e(N_e-1)f(\omega)]\left(\frac{\partial^2 I}{\partial\omega\partial\Omega}\right)_1 \tag{2.79}$$

which is simply an incoherent term plus a coherent term multiplied by the power radiated by a single electron. The coherent radiation is described by the factor $f(\omega)$.

Consider a specific particle configuration

$$S_1(r) = \frac{1}{N_e}\sum_{j=1}^{N_e}\delta\left(r - r_j\right) \tag{2.80}$$

where $S(r)$ is a continuous probability distribution (i.e. Gaussian, parabolic, etc.) function such that $N_e S(r)d^3r$ is the probability of finding a particle in the region d^3r about r. In other words, $S(r)$ is a particular ensemble average, $\langle S_1(r)\rangle$, of $S_1(r)$. The ensemble average of Eq. (2.78) becomes

$$f(\omega) = \frac{1}{N_e(N_e-1)}\left\langle \sum_{j,k=1(j\neq k)}^{N_e} e^{i\omega(r_j - r_k)/c}\right\rangle. \tag{2.81}$$

Two assumptions are used to evaluate Eq. (2.81). The first assumption is that $f(\omega)$ is independent of N_e for large N_e such that

$$f(\omega) = \lim_{N_e\to\infty}\frac{1}{N_e^2}\left\langle \sum_{j,k=1(j\neq k)}^{N_e} e^{i\omega(r_j - r_k)/c}\right\rangle. \tag{2.82}$$

The double sum in Eq. (2.82) will contain terms proportional to N and N^2, however only the N^2 terms will be kept and Eq. (2.82) can be written as

$$f(\omega) = \lim_{N_e\to\infty}\left\langle \sum_{j,k=1}^{N_e} e^{i\omega r/c} S_1(r)d^3r\right\rangle. \tag{2.83}$$

The second assumption is that the ensemble average can be evaluated by replacing the particle configuration $S_1(r)$ with the continuous particle distribution $S(r)$ so that

$$f(\omega) = \left|\int e^{i\omega r/c} S(r)d^3r\right|^2 \tag{2.84}$$

and the form factor becomes the square of the Fourier transform of the particle distribution.

If the transverse size of the beam is considered as well Eq. (2.79) can be written as

$$\left(\frac{\partial^2 I}{\partial\omega\partial\Omega}\right)_{N_e} = [N_e S_{inc} + N_e(N_e-1)S_{coh}]\left(\frac{\partial^2 I}{\partial\omega\partial\Omega}\right)_1 \tag{2.85}$$

where the incoherent factor, S_{inc}, is defined as

$$S_{inc} = \frac{1}{\sqrt{2\pi}\sigma_x}\int_0^\infty e^{-\frac{2x}{\lambda_e}} e^{-\left[(x-b)^2/2\sigma_x^2\right]} dx. \tag{2.86}$$

The coherent factor, S_{coh}, is

$$\begin{aligned} S_{coh} &= \left|\frac{1}{\sqrt{2\pi}\sigma_x}\int_0^\infty e^{-\frac{x}{\lambda_e}} e^{-\left[(x-b)^2/2\sigma_x^2\right]} dx\right|^2 \\ &\times \left|\frac{1}{\sqrt{2\pi}\sigma_y}\int_0^\infty e^{-ik_y y} e^{-\left[(y-y_o)^2/2\sigma_y^2\right]} dy\right|^2 \\ &\times \left|\int_{-\infty}^\infty e^{ik_z z} S(z) dz\right|^2 \end{aligned} \tag{2.87}$$

2.4.2 Multiple Bunches

The beam from the HRC accelerator is a train of electron bunches and the effect of multiple bunches should be considered. For periodic multiple bunches emission at harmonics of the bunch frequency was first predicted in [59]. For a train of N_b bunches the total current can be written as a sum of individual currents in each bunch

$$J_{total} = \sum_{m=1}^{N_b} J_1 e^{i2\pi mk\Delta z}$$

where Δz is the spacing between each bunch. The radiated energy, Eq. (2.85), becomes

$$\left(\frac{\partial^2 I}{\partial\omega\partial\Omega}\right)_{N_b} = \left(\frac{\partial^2 I}{\partial\omega\partial\Omega}\right)_{N_e}\left|\sum_{m=1}^{N_b}\exp\left[im2\pi\omega_{sp}/\omega_{rf}\right]\right|^2 \tag{2.88a}$$

$$= \left[\frac{\sin(\pi N_b\omega_{sp}/\omega_{rf})}{\sin(\pi\omega_{sp}/\omega_{rf})}\right]^2 \tag{2.88b}$$

$$\overset{N_b\to\infty}{=} N_b\delta(\omega_{sp}-n\omega_{rf}) \tag{2.88c}$$

where ω_{rf} is the RF frequency and ω_{sp} is the SPR frequency. The second term in Eq. (2.88b) has an amplitude of N_b^2 and a bandwidth of N_b^{-1} at the harmonics of the RF frequency. The effect should be measured by any coherent detector that is phase sensitive. Eq. (2.88c) shows that only frequencies at harmonics of the accelerator frequency should be measured. The measurement of the effect due to multiple bunches using a phase sensitive heterodyne receiver is described in Section 4.6. For incoherent detectors the radiation from each bunch adds linearly such that the radiation is enhanced by N_b.

2.5 Computer Codes

2.5.1 Image Charge Code

A code to calculate the SPR emitted from a bunch charge, Eq. (2.28), was written by Brownell [78]. The output of this code computes the radiant Smith-Purcell energy per steradian per cm of grating length as a function of either polar angle (θ) / wavelength or azimuthal angle (ϕ). The code solves Eq. (2.28) for an echelle grating, which consists of two planar facets that intersect at right angles as in Fig. 2-1. The code considers both the incoherent and coherent contributions to the radiation as in Eq. (2.85). The input for the code is the grating period, blaze angle, number of electrons, beam energy, height of the beam center, FWHM normal to the grating, FWHM parallel to the grating, longitudinal bunch shape (square, triangular, parabola, double-sided exponential, Gaussian) and length, order of emission and angle

of emission. The code typically takes one second to run and was used to design the gratings for the experiment as described in Chapter 4.

2.5.2 Electric Field Integral Equation Code

A code which solves Eq. (2.67) and computes the radiated energy, Eq. (2.71), was written at MIT. The code computes the radiated SPR energy per steradian. The parameters for the code are grating period, blaze angle, number of electrons, beam energy, height of beam center, longitudinal bunch length. The longitudinal bunch shape is assumed to be Gaussian. The code typically takes one day to run and was used to analyze the data.

Chapter 3

Experiment Design

This chapter discusses several aspects of the experiment. The HRC accelerator is described in detail in order to fully understand the mechanisms of short bunch production. The accelerator was simulated with the electron dynamics code PARMELA. Simulations of the output beam from the accelerator are presented for various operating regimes. The designs for several gratings are discussed and simulations of each grating using the image charge code are shown. Finally, the radiation beamline including the vacuum chamber, mirrors, windows and filters are described. Finally, the various detectors employed in the experiment are discussed.

3.1 Haimson Research Corp. Accelerator

The ongoing collaboration with HRC began in the early 90's when a 17 GHz klystron built for Science Research Laboratory (SRL) of Somerville, MA by HRC was relocated to the MIT Plasma Science and Fusion Center (PSFC). In addition to the klystron [79,80] HRC has built many of the components in use for the 17 GHz linac including: a series of microwave waveguides, loads, phase shifters and a four-port hybrid coupler, a DC, 550 kV thermionic electron gun [81], and the 17 GHz, 0.5 meter long linac [82]. The accelerator and klystron are driven by the MIT high voltage modulator [83] which produces 1 μs long pulses at voltages up to 700 kV at a repetition rate of 4 Hz.

3.1.1 HRC Klystron

The power for the accelerator is supplied by the high power klystron. A schematic of the klystron and accelerator is shown in Fig. 3-1. The HRC relativistic klystron is designed to produce up to 25 MW of RF power at 17.136 GHz for pulse lengths up to 1 μs in length. An electron gun, built for MIT by Thomson Co. for a free electron laser experiment [84], is used as the source for the $\sim$ 100 A electron beam in the klystron. The beam is space-charge limited and the gun perveance is 0.27 μperv. The drive for the klystron is provided by a travelling wave tube amplifier (TWTA) built by Applied Systems Engineering which provides 1-10 W. The input to the TWTA is a 2-18 GHz HP 6871B synthesizer which can produce between 1 μW and 10 mW of power. The synthesizer is typically run at $\sim$ 1 mW which produces $\sim$ 10 MW of klystron power.

The klystron consists of the input RF cavity, a gain section, and a travelling wave output section. The output connects to dual WR-62 waveguides. The tube is designed to have a gain of between 60 and 70 dB. Initial klystron experiments into a matched load produced output powers up to 26 MW with a saturated gain of 67 dB. However, subsequent use of the klystron found that there were several spurious modes and higher frequency modes present in the klystron. The klystron was rebuilt and damping circuits were added to suppress the modes. The klystron now achieves high power, stable operation and typically operates at 12 MW to supply enough power to the linac. A comparison of the design and measured klystron characteristics is shown in Table 3.1.

The klystron output power is fed into a four-port hybrid coupler specifically designed by HRC to allow the klystron power to be directed into two separate arms with incrementally varying power levels in each arm. The forward and reflected power to the linac are measured with a 65 dB directional coupler combined with additional attenuator chains terminated by low-barrier Schottky diode detectors. The attenuator chains, usually about 20-30 dB, and diode responses were calibrated at 17.140 GHz with the HP 8617B CW microwave source and an HP 4323B power meter.

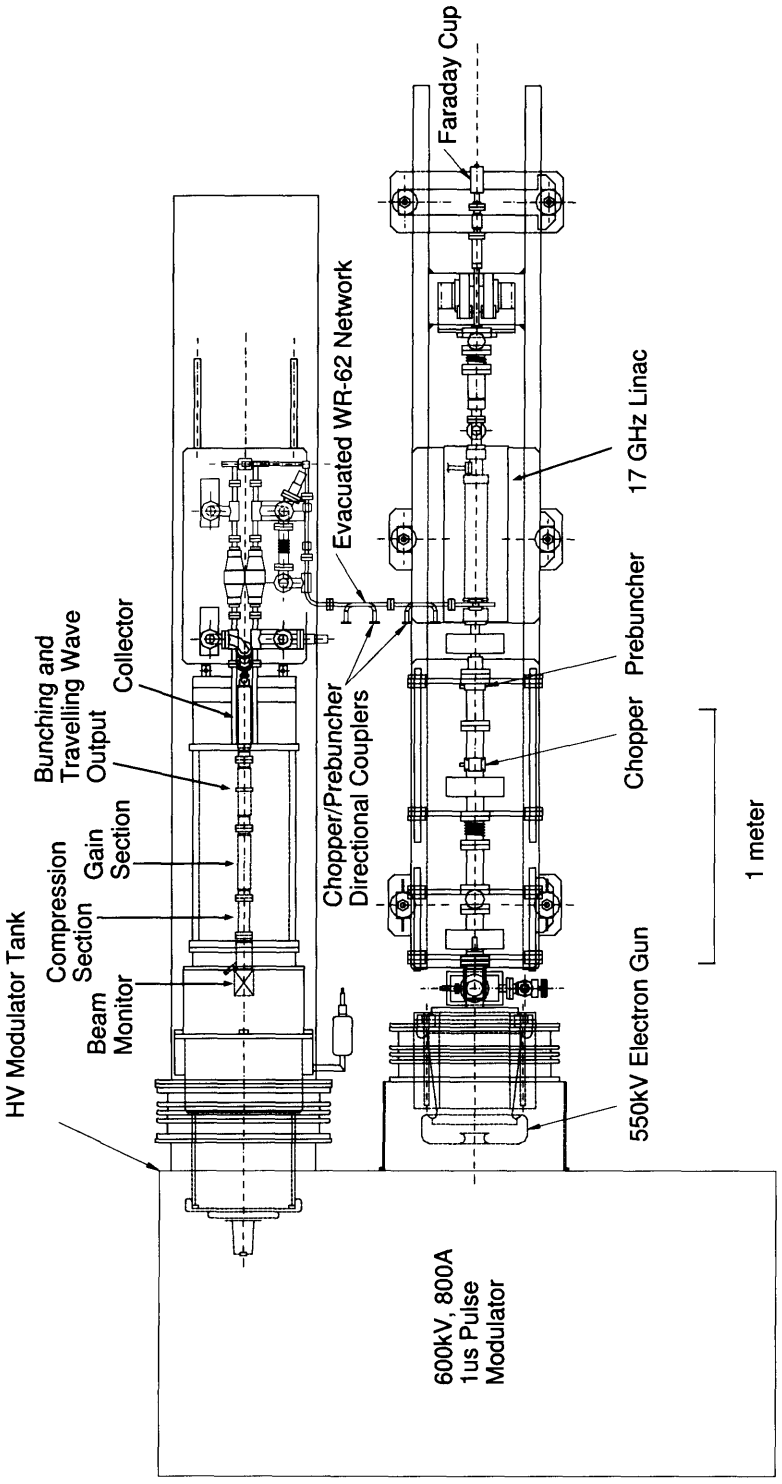

Figure 3-1: Schematic of the HRC klystron and accelerator.

Parameter	Design	Measured (1995)	Current
Frequency (GHz)	17.136	17.136	17.136
Voltage (kV)	580	560	550
Current (A)	100	95	88
Input RF Power (W)	20-25	5	2.8
Output RF Power (MW)	20-25	26	14
Gain (dB)	60	67	67
Pulse width (ns)	1000	150	150

Table 3.1: HRC Klystron Operating Parameters

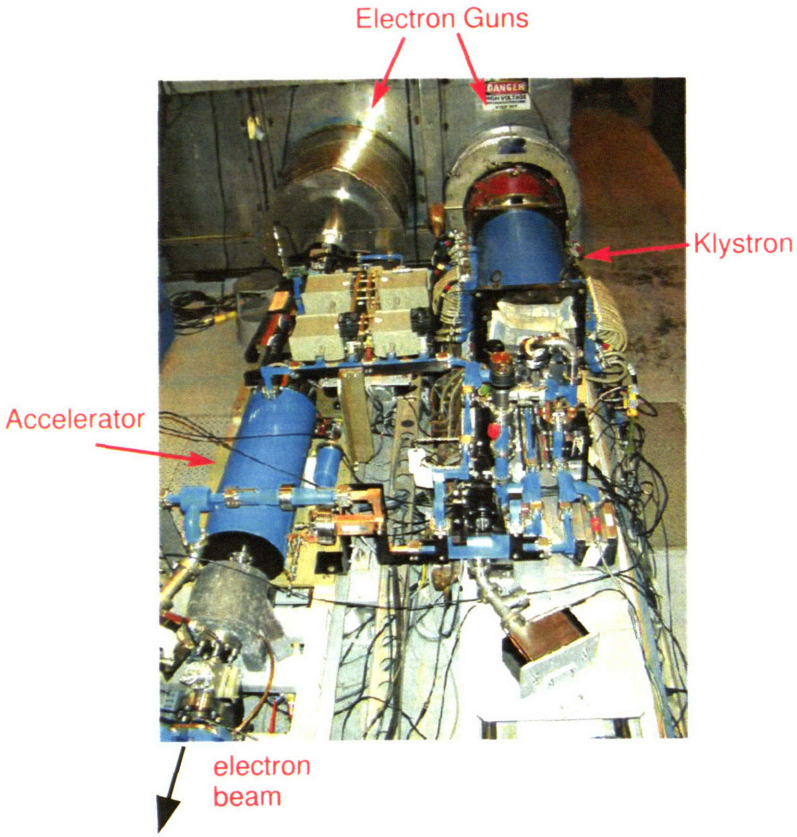

Figure 3-2: Picture of the HRC klystron and accelerator.

3.1.2 HRC Linac

The linac consists of a 550 kV electron gun, a chopper-prebuncher and three lens injector and a quasi-constant gradient accelerating structure consisting of 94-cavities that operate in the $2\pi/3$ mode. A comparison of the design and measured accelerator parameters is shown in Table 3.2. A picture of the klystron and accelerator is shown in Fig. 3-2.

The DC, 550 kV electron gun currently serves as the input for the linac. The gun was designed to produce a 1-2 A beam with an normalized RMS emittance between 2 and 3 π mm-mrad. Measurements of the emittance were performed using two collimators (0.8 and 3.4 mm radii) separated by 37 cm. The measurements indicate

Parameter	Design	Measured	Operation
Input Beam Energy (MeV)	0.5	0.5	0.515
Output Beam Energy (MeV)	20-30	17.5	15
Average Current (A)	0.25	0.1	0.15
Peak Current (A)	80	?	5-20
Bunch Length (degrees)	1.1(180 fs)	?	4-6
Energy Spread (%)	1.1	1	~ 1
Electrons per bunch	1x10^8	1x10^8	6x10^7
Macropulse width (ns)	1000	150	100
Bunch Separation (ps)	59	59	59
Micropulses/macropulse	1.7x10^4	2.5x10^3	1700

Table 3.2: HRC Accelerator Operating Parameters

that the gun produces a beam of current 0.94 A at 550 kV with a normalized RMS emittance of 1.8 π mm-mrad.

The chopper-prebuncher system [85] was designed to produce a high quality beam [$\beta\gamma\varepsilon \simeq 5\pi$ mm-mrad, $\Delta\beta_o < 0.3\%(\pm 5$ keV) and $\Delta\phi_o < 20°$] at the entrance to the linac. A schematic of the injection system is shown in Fig. 3-3 and a picture in Fig. 3-4. A DC magnetic dipole, located at the chopper cavity, is used to bias the RF scanned beam vertically below the centerline. With this biasing technique, the RF scanned beam is returned to the centerline once during each RF cycle so that a fraction of the incident beam is transmitted through a small diameter collimator. This allows injection into the linac during the period when both the energy spread and the rate of change of the transverse momentum introduced by the chopper cavity are tending to zero (i.e. $\frac{\partial V_{RF}}{\partial \omega t}$, $p_\perp$, $\frac{\partial p_\perp}{\partial \omega t} \longrightarrow 0$). The high field prebuncher cavity is designed to produce a 10:1 charge compression and reduce the 50 keV energy spread to < 10 keV prior to injection in the linac. Simulations predict that the injection system will allow $> 90\%$ of the charge to be injected into the linac with an energy spread of 8.8 keV and a longitudinal phase space of less than 15° [86].

The chopper cavity is designed to produce 100° bunches using a peak RF input power of 1.4 kW. The prebuncher was designed to produce bunches of length 15° using a peak power of 1.5 kW. Independently controlled phase shifters and power attenuators are used to adjust the phase relationship between the injector cavities

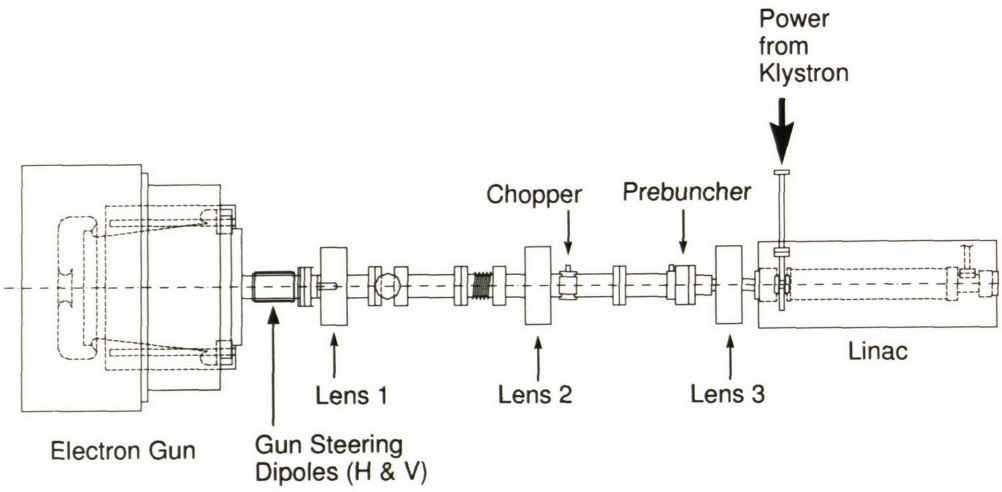

Figure 3-3: Schematic of the injection system for the accelerator.

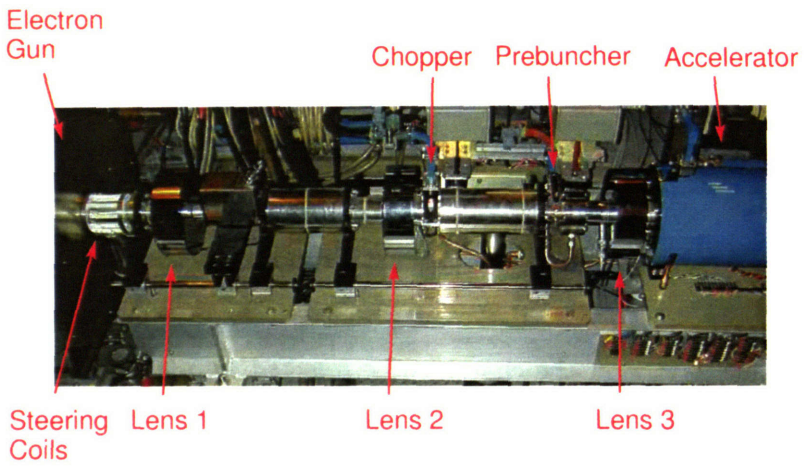

Figure 3-4: Picture of the injection system for the accelerator.

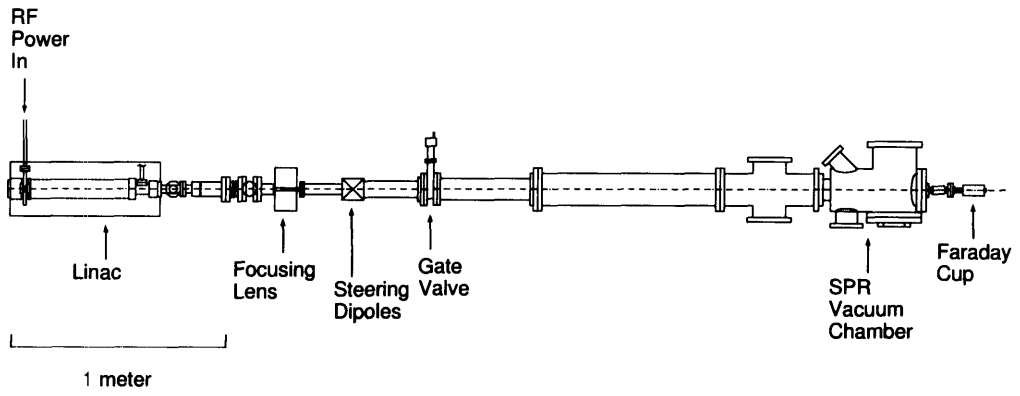

Figure 3-5: Schematic of the accelerator beamline.

and the linac and the power levels of each cavity. The 15° input bunch is further compressed during acceleration in the linac down to 1°, which corresponds to 180 femtoseconds or 60 microns at 17 GHz.

The linac can also run with power only into the prebuncher (i.e. no chopper power). In this mode the DC beam is prebunched directly. As a result two ~120° bunches are formed per RF period. When the prebuncher is phased properly one bunch is accepted by the linac (in phase with the capture field in the first cell) and the second bunch is rejected. As a result of the longer input phase, ~120°, a longer output bunch is produced, ~ 6°.

3.1.3 Electron Beamline

After the exit of the accelerator the beam travels for ~ 0.5 m before reaching a toroidal focusing lens as shown in Fig. 3-5. The lens can produce a peak field of up to 0.6 T. At 0.6 T the minimum beam spot size should be 1 mm. A set of vertical and horizontal steering coils are located ~ 10 cm downstream from the focusing lens. The grating is located ~ 2.5 m downstream from the lens and a faraday cup to measure charge is located 40 cm past the grating. There are also two beam monitors located before and after the linac to measure the beam current.

3.2 Accelerator Simulations

Although several simulations of the HRC accelerator under certain operating conditions are published in [86] it was necessary to perform more simulations under various operating conditions using the publicly available PARMELA code [87]. PARMELA is a multiparticle 2D beam dynamics code that includes the effects of cylindrically symmetric RF field distributions as well as space charge forces. The accelerator was originally designed to reach gradients of 50 MeV/m, however, the accelerator was not operated above 35 MeV/m, in order to prevent breakdown damage to the structure. For the experiments described in this thesis the beam energy was 15 MeV (gradient ~30 MeV/m).

3.2.1 50 MeV/m

The first procedure involved creating a PARMELA input file for the accelerator structure that reproduced identical results to those in [86]. A plot of the emergent electron energy for various injection energies is shown in Fig. 3-6. A similar plot reproduced from [86] is shown in Fig. 3-7. Good agreement is obtained between the PARMELA simulations and HRC-ELOR [88] indicating that PARMELA can be used to simulate the accelerator.

Simulations were also performed to predict the output phase length of the electron bunch at the accelerator exit. A plot of the output bunch length (rms) is shown in Fig. 3-8. According to PARMELA, the minimum output bunch length from the accelerator is predicted to be 50 μm, which is in close agreement with the value of 60 μm given in [86]. The injection beam into the accelerator was specified as 0.5 MeV and 20° input phase length.

3.2.2 30 MeV/m

Since the beam energy for these experiments was 15 MeV the accelerator was simulated for 30 MeV/m gradients in order to have an estimate of the output bunch length. The gradient that the accelerator was set to 30 MeV/m, resulting in an output beam

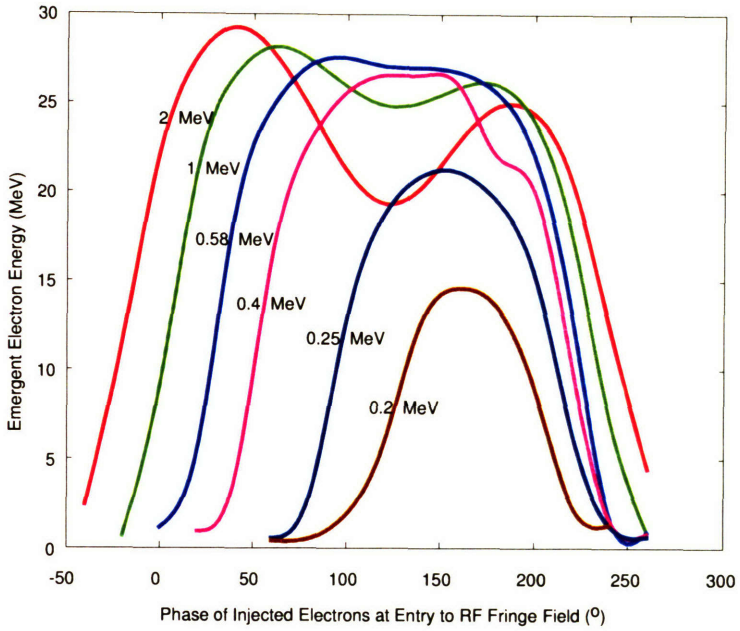

Figure 3-6: Plot Showing Emergent Energy vs. Injection Phase of the 17 GHz TW Linac for a Range of Injection Energies produced by PARMELA.

energy of ~14 MeV. A plot of the output energy versus input phase is shown in Fig. 3-9. The output bunch length approaches 70 μm under these operating conditions as shown in Fig. 3-10. An input beam of 0.5 MeV and 20° input phase length was used.

3.2.3 Linac Operating with PreBuncher Only

The simplest mode of operation for the linac is to operate with only a prebunched beam (no chopper power). This allows the proper phase relationship between the prebuncher and accelerator to be found by scanning the phase of the prebuncher with respect to the linac and observing the amount of charge exiting the linac. The ideal phase is found when the maximum beam transmission is observed. The input phase length for $\sim$ 1.5 kW prebuncher power should be $\sim$ 60° [89]. PARMELA simulations were run for 32 MeV/m gradient, 0.5 MeV, 60° input beam and the output bunch length was simulated to be 200 μm as shown in Fig. 3-11.

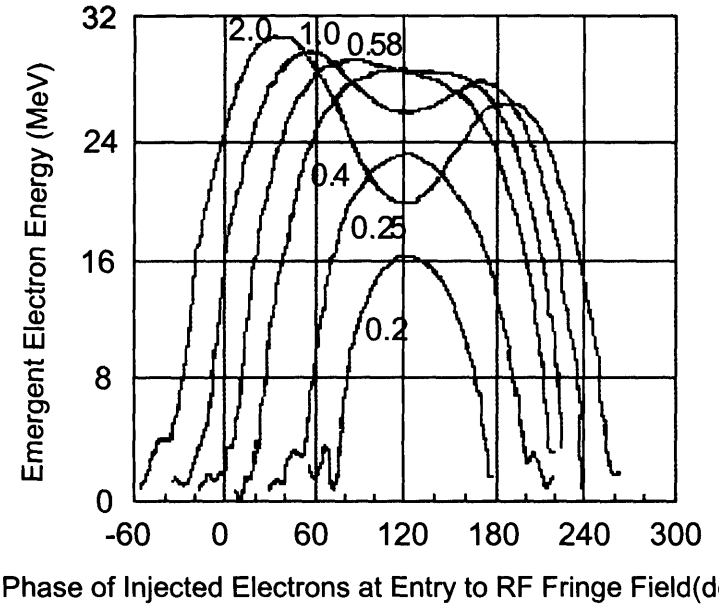

Figure 3-7: Phase Orbit Plots Showing Cut-off and Acceptance of the 17 GHz TW Linac for a Range of Injection Energies. Adapted from [86].

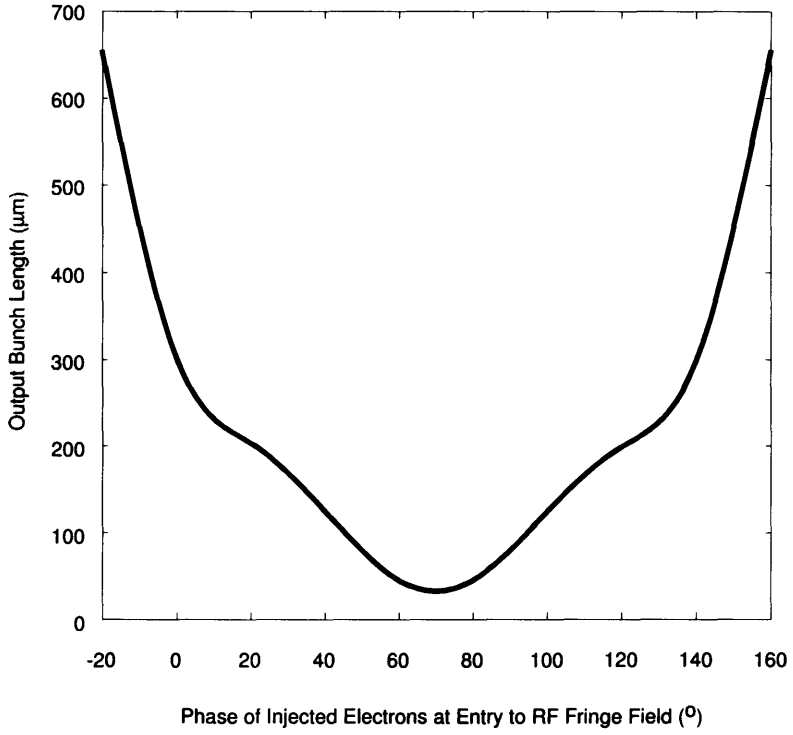

Figure 3-8: Output bunch lengths from the 17 GHz TW Linac for a Range of Injection Phases. The Linac was simulated with 50 MeV/ m gradient and an input beam energy of 0.5 MeV and 20° input phase.

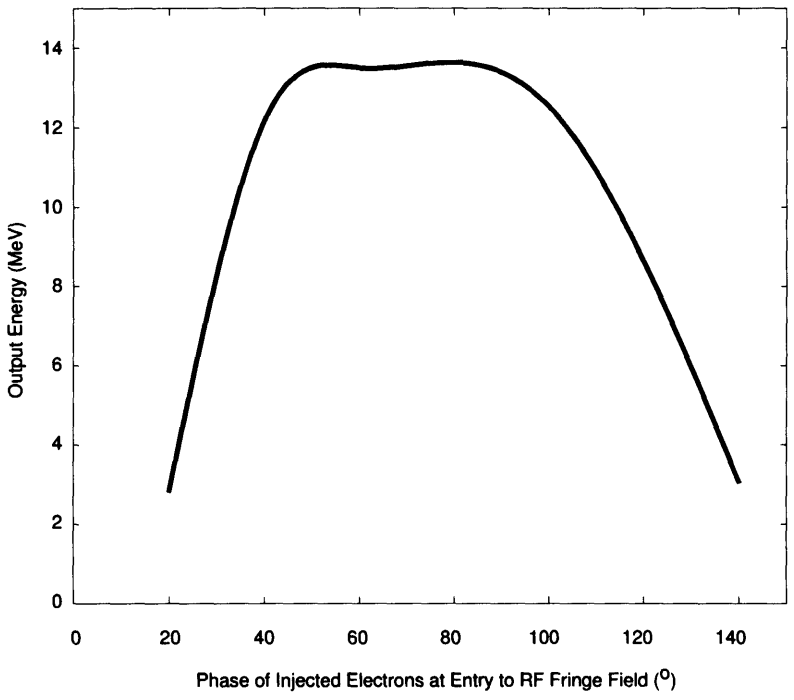

Figure 3-9: Output Energy from the 17 GHz TW Linac for a Range of Injection Phases. The Linac was simulated with 30 MeV/m gradient and an input beam energy of 0.5 MeV and 20° input phase.

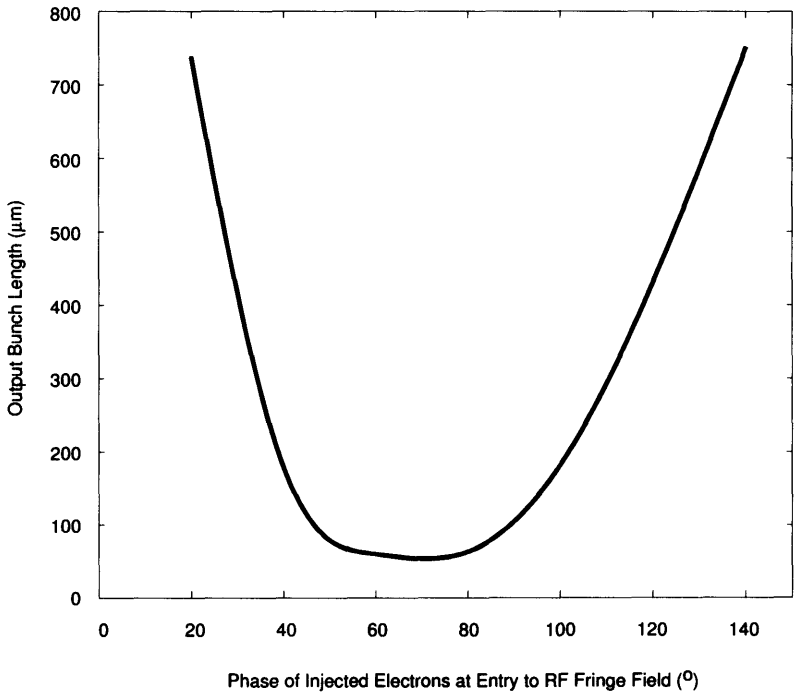

Figure 3-10: Output Bunch Length from the 17 GHz TW Linac for a Range of Injection Phases. The Linac was simulated with 30 MeV/ m gradient and an input beam energy of 0.5 MeV and 20° input phase.

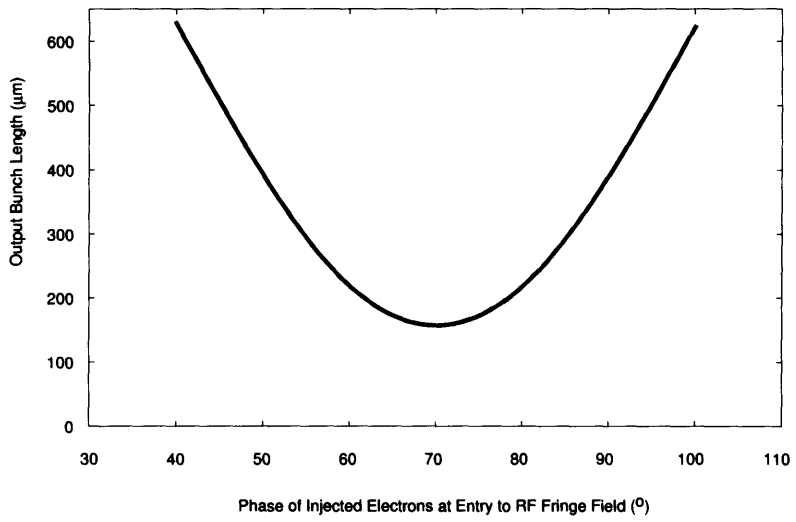

Figure 3-11: Output Bunch Length from the 17 GHz TW Linac for a Range of Injection Phases. The Linac was simulated with 30MeV/ m gradient and an input beam energy of 0.5 MeV and 60° input phase.

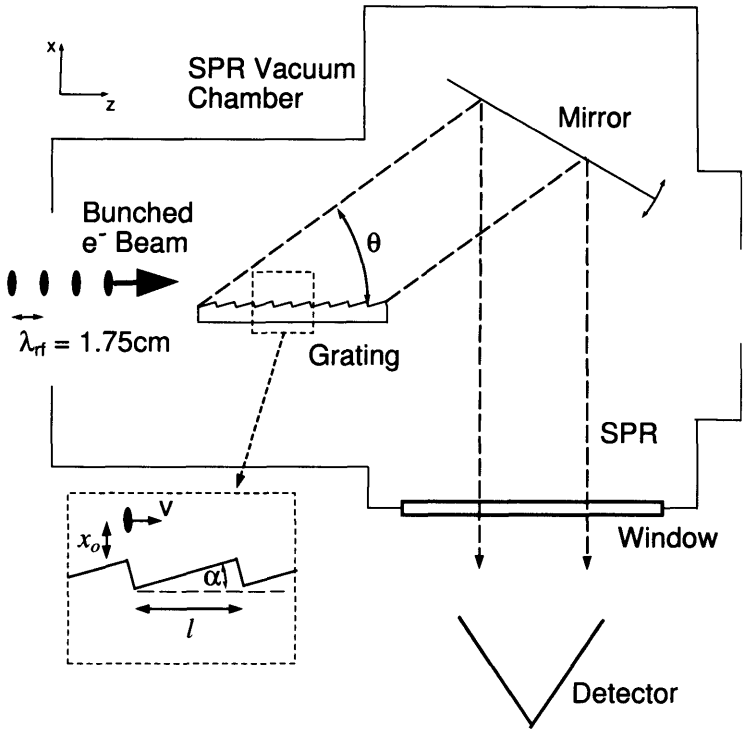

Figure 3-12: Schematic of the SPR Diagnostic Chamber.

3.3 Chamber Design

A general description of the SPR diagnostic vacuum chamber is useful to understand the necessary components to the experiment and how each component fits together. The purpose of the vacuum chamber is to allow for the generation and collection of SPR from a grating. The necessary components are: the grating, a mirror/focusing element and a window through which the radiation is extracted from the vacuum system. An schematic of the vacuum chamber is shown in Fig. ??. The ability to adjust the height of the grating with respect to the beam was incorporated into the design. The front and back of the grating are independently controlled to allow for alignment of the beam along the grating. Also, a means of adjusting the mirror is necessary in order to ensure that a specific angle of radiation is transmitted out of the vacuum chamber. The grating and mirror movement are controlled via remotely

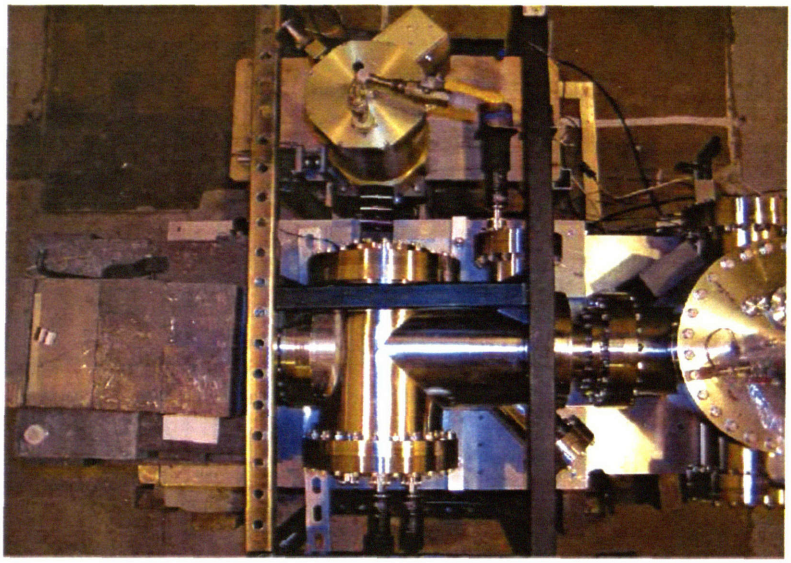

Figure 3-13: A picture of the SPR Diagnostic Chamber. The beam enters from the right and stops in a faraday cup (covered by lead bricks).

controlled stepper motors. A control system that allows for the movement of both the grating and mirror from the control room was built by the author. A picture of the SP chamber on the beamline is shown in Fig. 3-13.

3.4 Grating Design

The procedure developed by Trotz [90] for optimizing the grating parameters for a particular set of beam characteristics (energy, bunch length) was followed for the HRC beam parameters described in Table 3.2. Several gratings were designed to allow for measurements of various bunch lengths ranging from 100 fs to 1.5 ps.

3.4.1 2.1 mm Grating (200 fs bunch)

The first grating was designed for the minimum bunch length that the accelerator would be able to produce, namely 200 fs. Additionally, an energy of 15 MeV ($\gamma = 30$), waist of 1 mm, and emittance of 2.5 π mm-mrad are assumed . A 200 fs bunch will have a peak in the radiation at 60 microns, which corresponds to the bunch length. The optimum impact parameter is

$$b = \frac{\gamma\lambda}{2\pi} = 300\ \mu m. \tag{3.89}$$

The optimum waist diameter is approximately

$$b4\sqrt{\ln 2} \simeq 1\ mm \tag{3.90}$$

which is comparable to the existing beam waist ($\sim$ 2 mm) at the exit of the linac and achievable with the focusing lens. The optimum grating period is $l = \lambda\gamma = 2.1$ mm. The total grating length is restricted to 10 cm in order to be able to extract most of the radiation from the chamber through the 10 cm window. The blaze angle is found by determining the peak emission angle from the overlap of the form factor and the grating efficiency function. The form factor peaks at $\theta \simeq \sqrt{2/\gamma} = 13.7°$. For a blazed grating the grating efficiency factor peaks at twice the blaze angle giving an optimum blaze angle of 7°. A compromise value of 10° was settled on.

The Brownell Image Charge code was run with the grating and beam parameters shown in Table 3.3. Several plots of the emitted SPR per solid angle per cm were produced. The energy as a function of polar angle (θ) for several different bunch

Parameter	Value
Grating Period	2.1 mm
Grating Blaze Angle	10°
Beam Energy	15 MeV
Beam Waist - Normal	1.0 mm
Beam Waist - Parallel	1.0 mm
Number of Electrons	$1x10^8$
Impact Parameter	0.75 mm
Longitudinal Profile	Gaussian

Table 3.3: 2.1 mm Grating Parameters

lengths is shown in Fig. 3-14. The energy as a function of wavelength for several different bunch lengths is shown in Fig. 3-15. Normalized energy as a function of angle for several different bunch lengths is shown in Fig. 3-16. The energy as a function of azimuthal angle (ϕ) for several different bunch lengths is shown in Fig. 3-17. The energy from various orders of emission as a function of polar angle for a 200 fs bunch is shown in Fig. 3-18. Fig. 3-18 shows that the 2^{nd} order emission is an order of magnitude smaller than the 1^{st}. The energy as a function of polar angle for a 200 fs bunch and a 0.75 mm impact parameter but various beam waists is shown in Fig. 3-19.

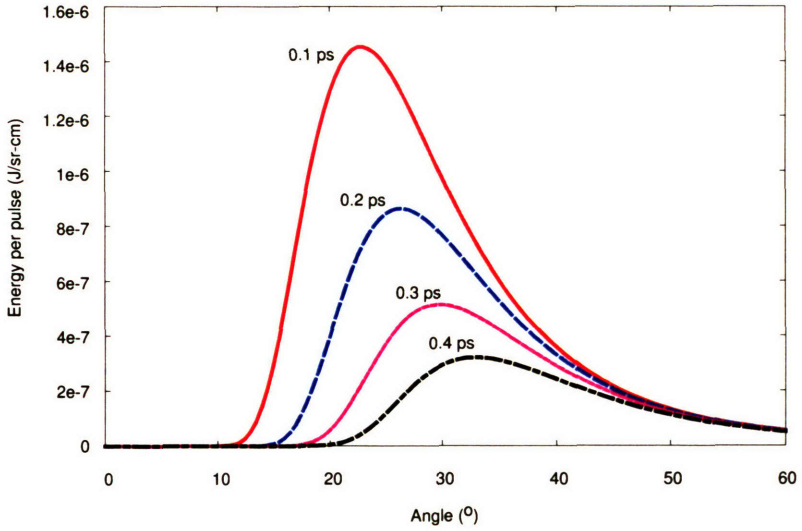

Figure 3-14: S-P radiant energy vs. Angle (θ) for Various Bunch Lengths for a 2.1mm grating period.

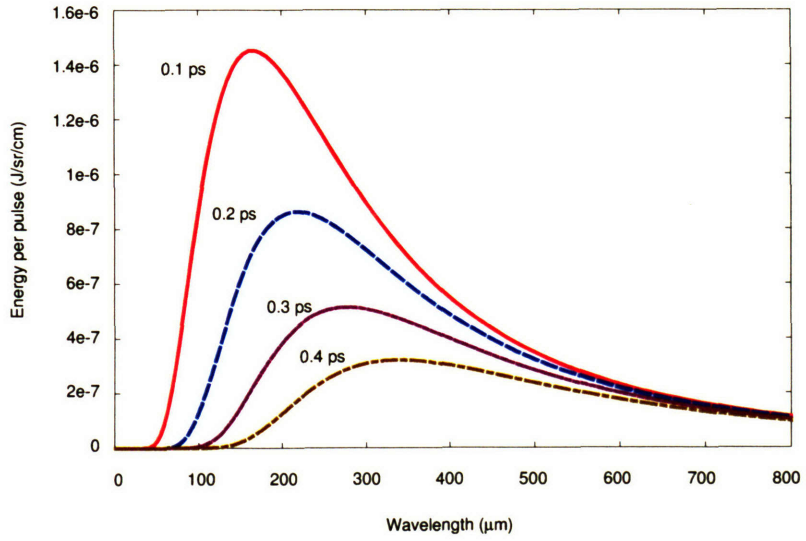

Figure 3-15: S-P radiant energy vs. Wavelength for Various Bunch Lengths for a 2.1 mm grating period.

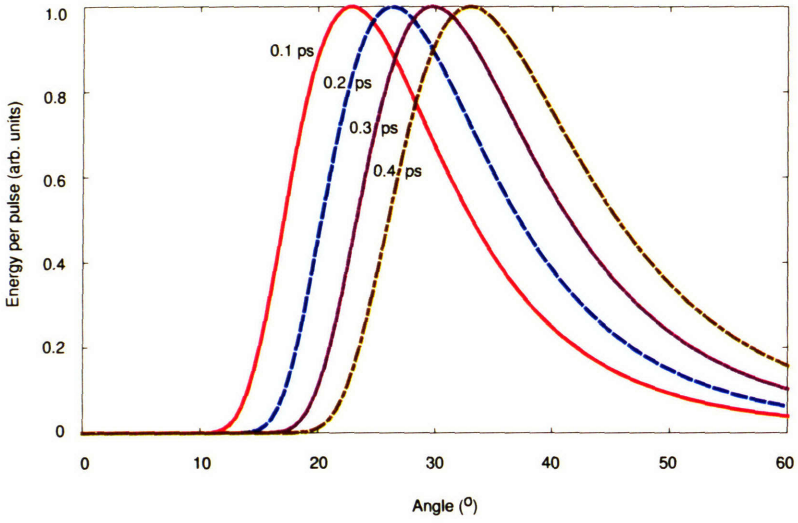

Figure 3-16: Normalized S-P radiant energy vs. Angle (θ) for Various Bunch Lengths for a 2.1mm grating period.

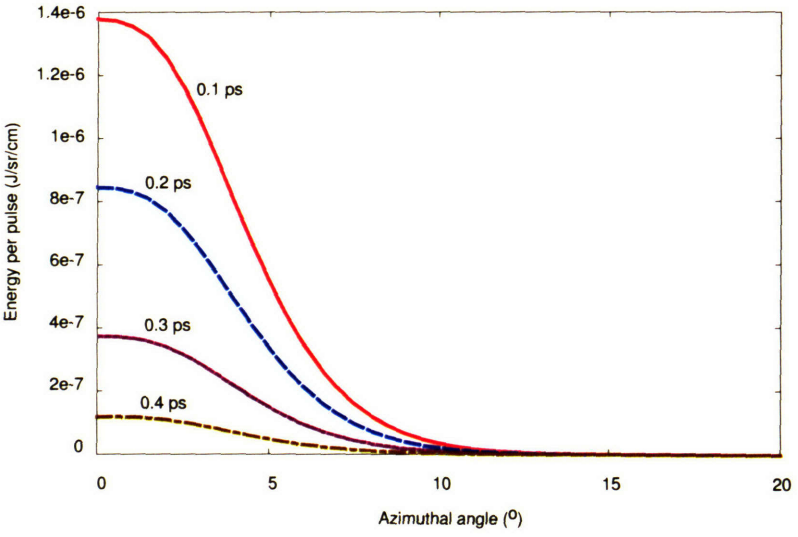

Figure 3-17: S-P radiant energy vs. Azimuthal Angle (ϕ) for Various Bunch Lengths for a 2.1mm grating period.

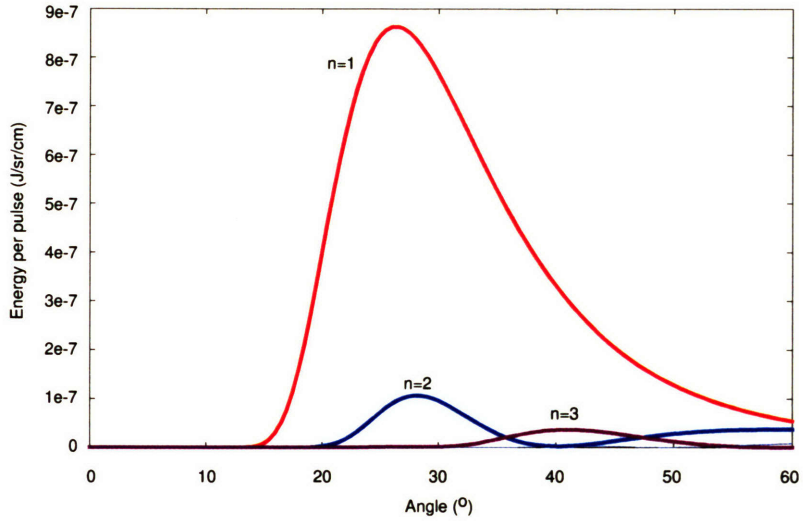

Figure 3-18: S-P radiant energy vs. Polar Angle (θ) for Various Emission Orders for a 2.1mm grating period.

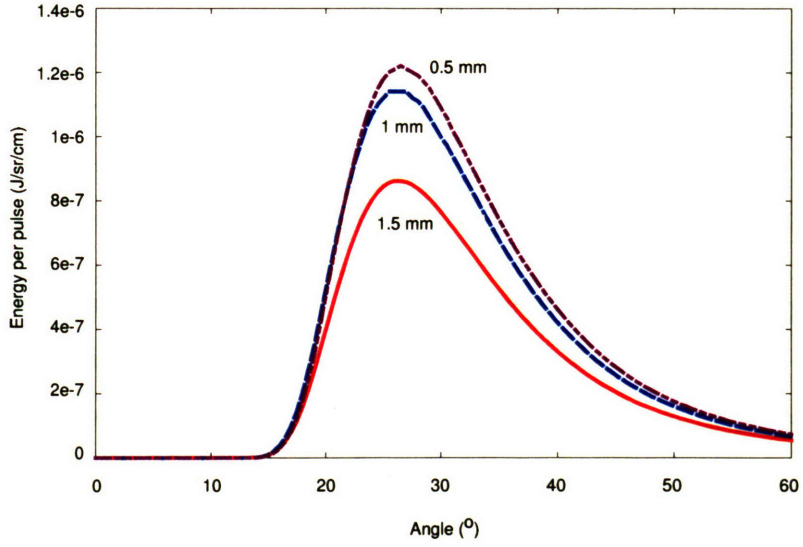

Figure 3-19: S-P radiant energy vs. Polar Angle (θ) for Various Beam Waists for a 2.1mm grating period and 200 fs bunch.

Parameter	Value
Grating Period	10 mm
Grating Blaze Angle	10°
Beam Energy	15 MeV
Beam Waist - Normal	1.0 mm
Beam Waist - Parallel	1.0 mm
Number of Electrons	$1x10^8$
Impact Parameter	0.75 mm
Longitudinal Profile	Gaussian

Table 3.4: 10 mm Grating Parameters

3.4.2 10 mm Grating (1 ps bunch)

A 10 mm grating was designed for the longest bunch length that the accelerator would produce ($\sim$ 1 ps bunches) while operating with only the prebuncher. The other beam parameters were still considered to be identical i.e. E = 15 MeV ($\gamma = 30$), waist of 1 mm, and emittance of 2.5 π mm-mrad. A 1 ps bunch will have a peak in the radiation at 300 microns, corresponding to the bunch length. The optimum impact parameter is

$$b = \frac{\gamma\lambda}{2\pi} \simeq 1.6\ mm. \tag{3.91}$$

The optimum waist diameter is approximately

$$b4\sqrt{\ln 2} \simeq 5\ mm \tag{3.92}$$

which is slightly larger than the existing beam waist. The optimum grating period is $l = \lambda\gamma = 10$ mm. The grating length is still limited to 10 cm in order to be able to extract most of the radiation. An identical blaze angle was chosen.

Several plots of the emitted Smith-Purcell radiation per solid angle per cm were produced. The energy as a function of polar angle (θ) for several different bunch lengths is shown in Fig. 3-20. The energy as a function of wavelength for several different bunch lengths is shown in Fig. 3-21. Normalized energy as a function of angle for several different bunch lengths is shown in Fig. 3-22. The energy as a

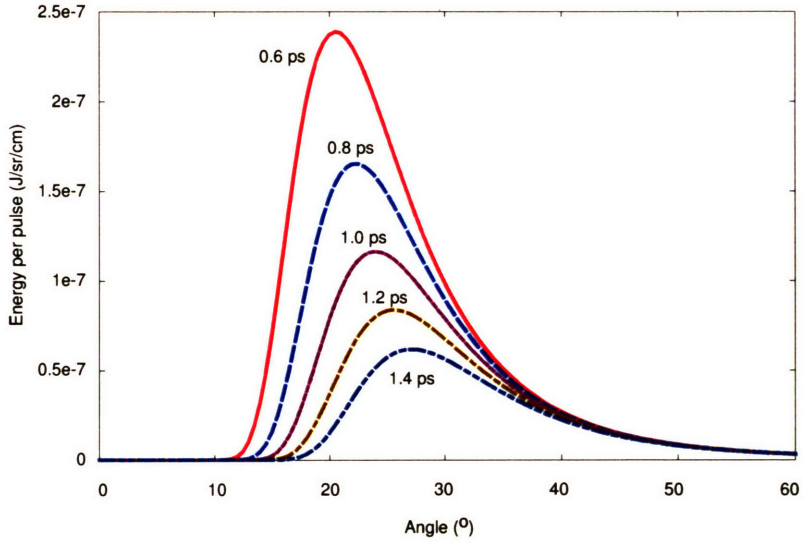

Figure 3-20: S-P radiant energy vs. Angle (θ) for Various Bunch Lengths for a 10mm grating period.

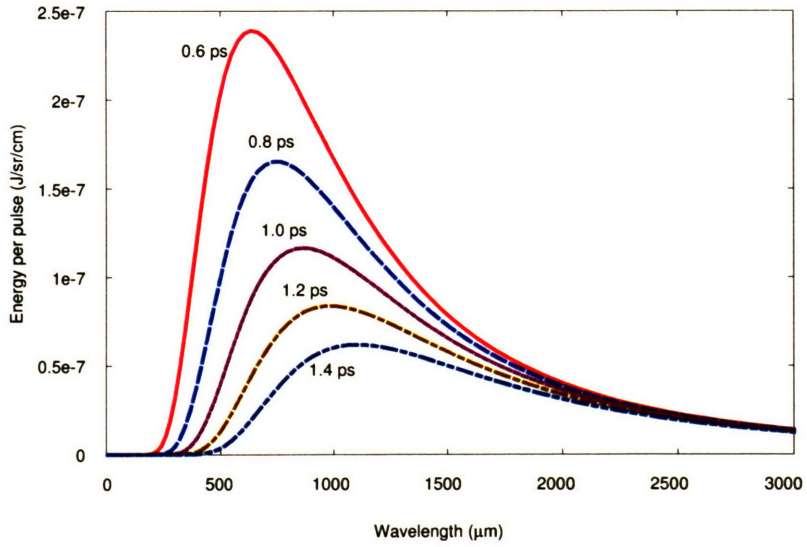

Figure 3-21: S-P radiant energy vs. Wavelength for Various Bunch Lengths for a 10mm grating period.

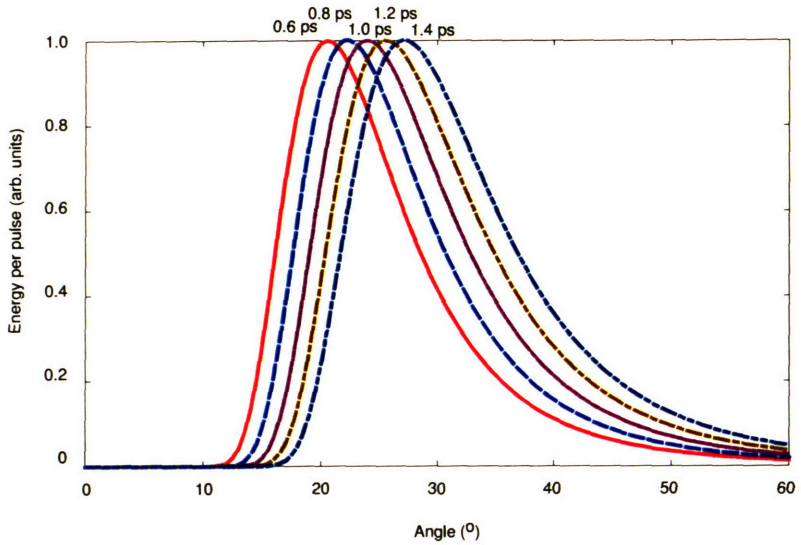

Figure 3-22: Normalized S-P radiant energy vs. Angle (θ)for Various Bunch Lengths for a 10 mm grating period.

function of azimuthal angle (ϕ) for several different bunch lengths is shown in Fig. 3-23. The energy from various orders of emission as a function of polar angle for a 800 fs bunch is shown in Fig. 3-24. The energy as a function of polar angle for a 800 fs bunch and a 0.75 mm impact parameter but various beam waists is shown in Fig. 3-25.

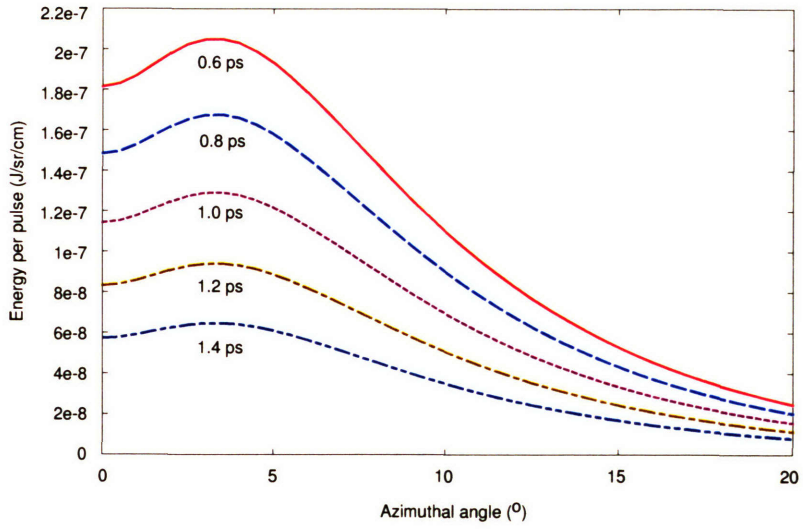

Figure 3-23: S-P radiant energy vs. Azimuthal Angle (ϕ) for Various Bunch Lengths for a 10 mm grating period.

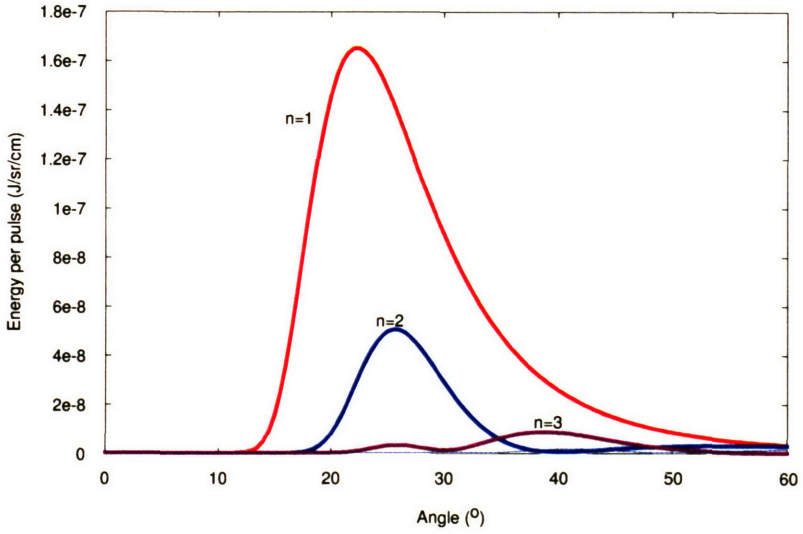

Figure 3-24: S-P radiant energy vs. Polar Angle (θ) for Various Emission Orders for a 10mm grating period.

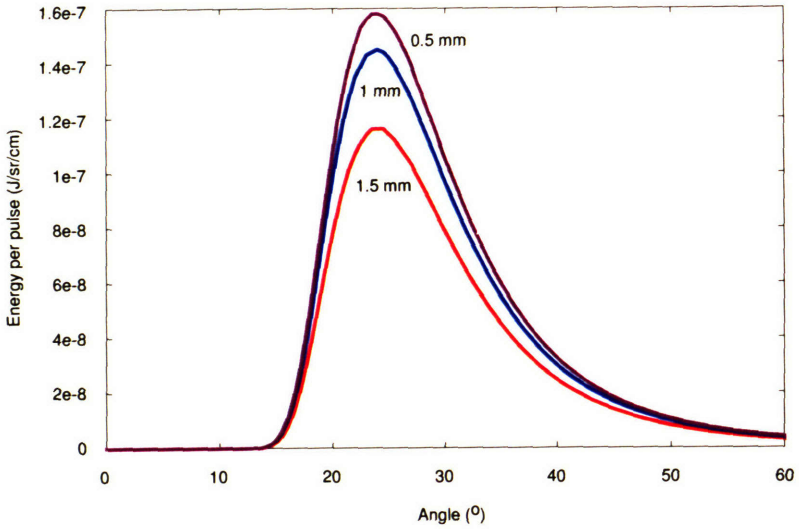

Figure 3-25: S-P radiant energy vs. Polar Angle (θ) for Various Beam Waists for a 10mm grating period.

Parameter	Value
Grating Period	6 mm
Grating Blaze Angle	10°
Beam Energy	15 MeV
Beam Waist - Normal	1.0 mm
Beam Waist - Parallel	1.0 mm
Number of Electrons	$1x10^8$
Impact Parameter	0.75 mm
Longitudinal Profile	Gaussian

Table 3.5: 6 mm Grating Parameters

3.4.3 6 mm Grating (600 fs bunch)

The third grating was designed for the middle range of bunch lengths that the accelerator would produce ($\sim$ 600 fs bunches). The other beam parameters were still considered to be identical i.e. E = 15 MeV ($\gamma = 30$), waist of 1 mm, and emittance of 2.5 π mm-mrad. A 600 fs bunch will have a peak in the radiation at 180 microns, which corresponds to the bunch length. The optimum impact parameter is then

$$b = \frac{\gamma\lambda}{2\pi} = 1.0\ mm. \tag{3.93}$$

The optimum waist diameter is approximately

$$b4\sqrt{\ln 2} \simeq 3\ mm \tag{3.94}$$

which is slightly larger than the existing beam waist. The optimum grating period is $l = \lambda\gamma = 6.3$ mm. The grating length is still limited to 10 cm in order to be able to extract most of the radiation. An identical blaze angle was chosen. Similar plots for the emitted SPR energy per solid angle per cm were produced but will not be shown here.

3.5 Mirror Design

Two different mirror designs were developed, a flat mirror and a curved mirror (in the xz plane). The advantage of a flat mirror is that one emission angle is directed out perpendicular to the window perpendicular to the window. The advantage of a curved mirror is that the radiation can be focused and more radiation can be collected. The design parameters for each mirror are presented.

3.5.1 Flat Mirror

A schematic of the flat mirror is shown in Fig. 3-26. Theoretically, the detector can be placed at any distance from the window. Using a flat mirror requires that the angle of the mirror be changed in the vacuum chamber in order to observe a different angle at the detector location. A CAD drawing of the grating, flat mirror and detector is shown in Fig. 3-27. The major disadvantage of the flat mirror is that the grating "image", i.e. the SPR at a particular angle, is spread out in space and can not be collected by the detector at one location. Thus, the detector must be scanned along the window.

3.5.2 Curved Mirror

A schematic of the grating and curved mirror system is shown in Fig. 3-28. The focal plane of the mirror was chosen to be the window to allow for maximum transmission through the window. Based on the distance from the mirror to the window the focal length of the mirror should be $\sim$ 24 cm. The range of SPR angles necessary for collection are $\sim$ 15°-40°, which gives an average angle of 27.5°. Thus, the radius of the mirror is then

$$R = 2f\frac{1}{\cos(\theta_{ave})} \approx 49\ cm. \tag{3.95}$$

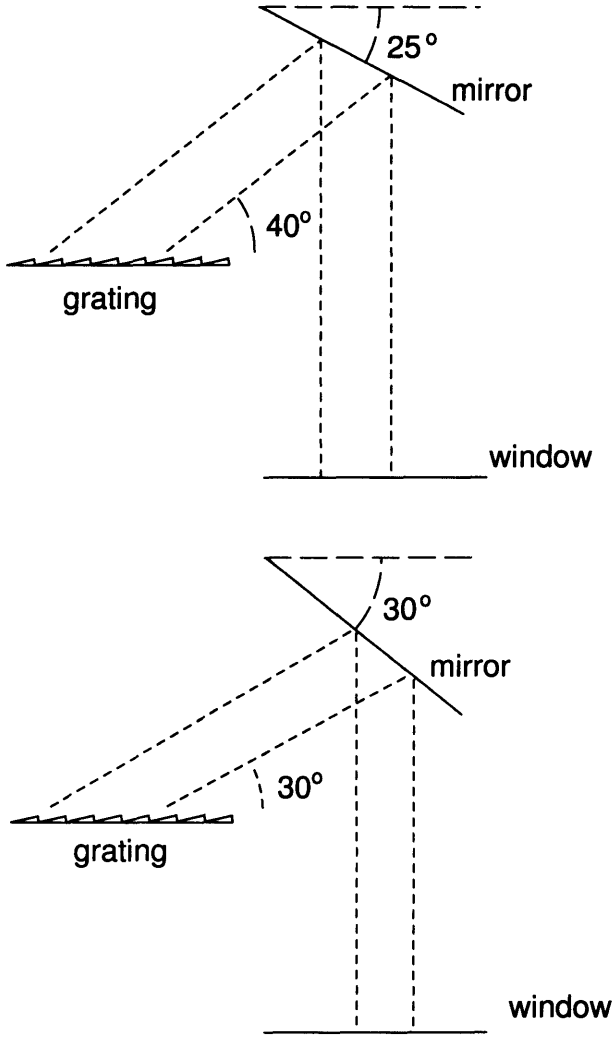

Figure 3-26: Schematic Showing the Radiation Trajectories from the Grating and Flat Mirror for Two Different Emission Angles.

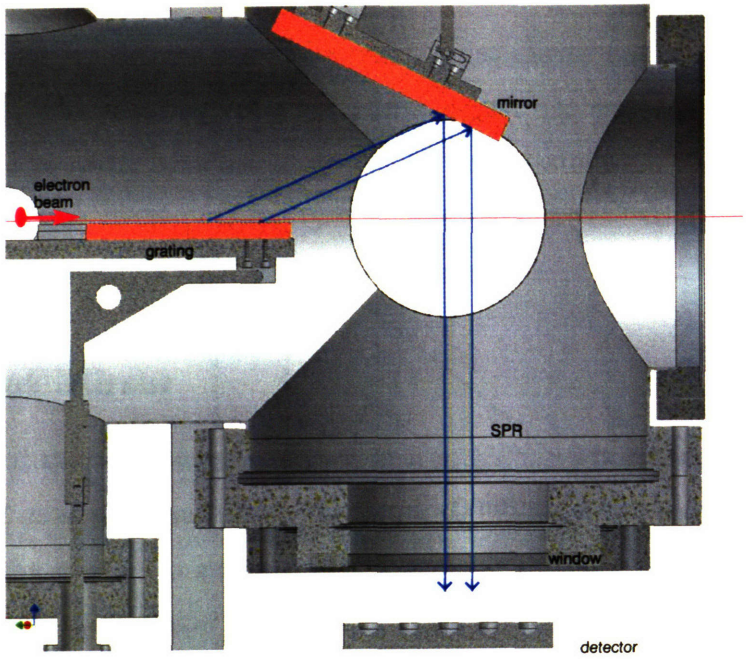

Figure 3-27: CAD drawing of the grating, mirror and radiation system.

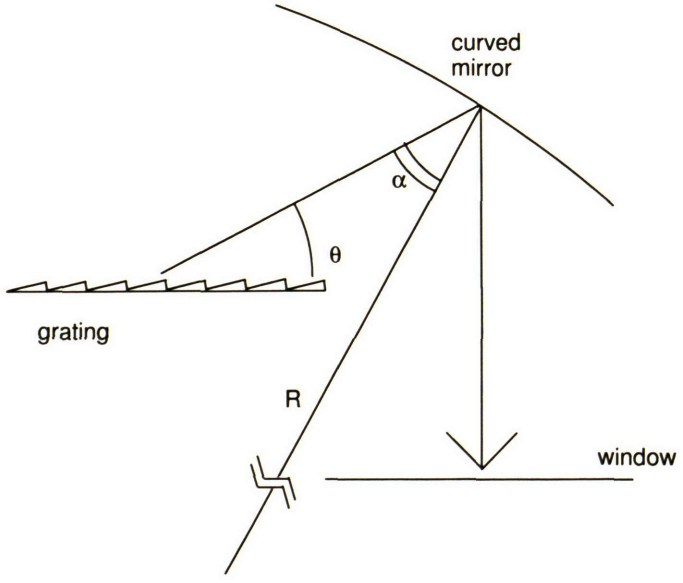

Figure 3-28: Schematic Showing the Radiation Trajectories from the Grating and Curved Mirror.

3.6 Radiation Detection System

Two different detectors were used to detected the SPR: a bolometer and a heterodyne receiver. The bolometer is classified as a thermal detector and as such has a very flat and broad responsivity. The heterodyne receiver is a coherent detector which responds to the electric field strength of the signal and can preserve phase information about the signal. The bolometer was used to verify the SPR resonance condition, the dependence on beam height and current and to measure the angular distribution of the radiation. The heterodyne receiver was used to measure the frequency locking of the SPR to the accelerator frequency and the bandwidth of each of the harmonics. A description of each detector follows.

3.6.1 Bolometers

The bolometer is a thermal detector that absorbs photons and thermalizes their energy. The absorbed energy changes the electrical resistance of the detector material subsequently changing the electric current passing through the material. The change in current is measured and amplified. The wavelength dependence of the responsivity is very flat and as broad as the photon-absorbing material allows. A schematic of a simple bolometer is shown in Fig. 3-29. Since the bolometer signal is generated electronically it is subject to fundamental electronic noise mechanisms. Additionally, the bolometer suffers from thermal fluctuations across the link between the element and heat sink. As a result good performance can only be obtained at very low temperatures, i.e. liquid helium ($\sim$ 4 K).

The bolometer utilized in the Smith-Purcell experiment is a Infrared Laboratories Silicon Bolometer. A picture of the bolometer is shown in Fig. 3-30. The bolometer is mounted in a side looking configuration with a Winston cone collector, a three position filter wheel, far-infrared cut-on type filters and an outer vacuum window. The bolometer is a composite type with a small silicon element thermally bonded to a blackened 2.5 mm diamond absorber mounted in a cylindrical cavity. The absorbing layer thickness has been especially selected to minimize fringing effects.

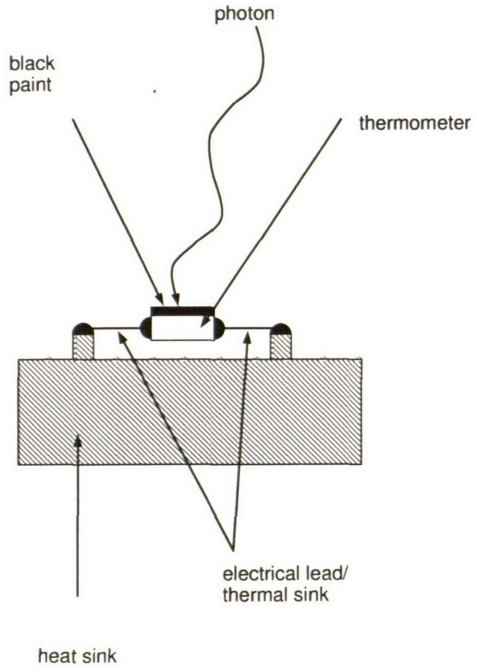

Figure 3-29: Schematic of a simple bolometer.

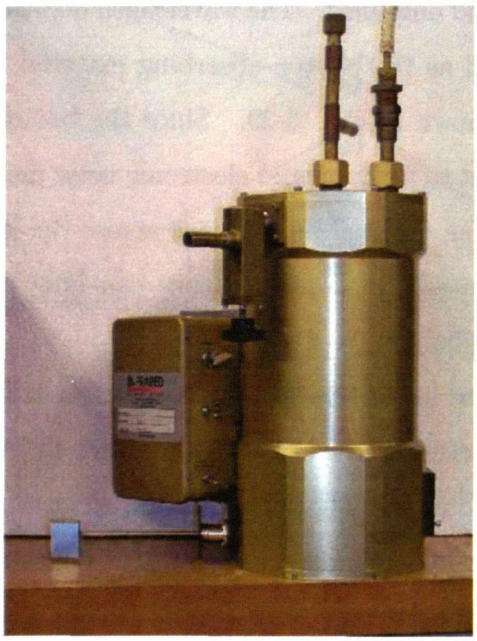

Figure 3-30: Picture of the Infrared Laboratories bolometer.

Power $[mW]$	Pulse Length $[\mu s]$	Response Time $[ms]$	Signal $[mV]$	Gain	Responsivity $[V/W]$
2	5	2	400	1000	8×10^4
2	5	2	92	200	1.84×10^4
2	1	2	100	1000	1×10^5
2	1	2	20	200	2×10^4

Table 3.6: Measured Detector Responsivity

The Winston cone features an entrance aperture of 12.7 mm at a focal ratio of 3.8 and an exit aperture of 1.8 mm and has been gold plated to prevent tarnish and to improve thermal properties. Three cut on filters were available: 30 μm, 100 μm, 330 μm. The outer vacuum window was a wedged type 1 mm HI density polyethylene with diamond (5-10 μm) coating on one side.

The responsivity of the detector was measured electrically by Infrared Laboratories to be 2.63x10^5 V/W. The detector was tested at MIT with a 250 GHz ($\lambda = 1.2mm$), 2 mW, CW solid state source built by Millitech. The source power level was measured with a calibrated Scientech calorimeter. The source has the ability to be pulsed via a TTL input. When the source was pulsed at 1 Hz with 5 μs pulse lengths the detector measured 400 mV on a gain setting of 1000 and 92 mV on a gain setting of 200. When the source was pulsed at 1 Hz with 1 μs pulse lengths the detector measured 100 mV on a gain setting of 1000 and 20 mV on a gain setting of 200. The detector response time was $\sim$ 2 ms, measured from the start to the peak of the signal. The responsivity can be written as

$$S = \frac{V_{[V]}}{P_{[W]}} = \frac{V_{[V]}}{\left(P_{[W]} \times \tau_{[s]}\right)/\tau_{d[s]}}.$$

Table 3.6 shows the measured signals and the respective responsivity values. The detector responsivity was taken to be 2x10^4 V/W on the low gain setting. The discrepancy between the Infrared Laboratory number and our measured number is due to the fact that they simply measured the electrical responsivity of the silicon element and not the response to radiation which includes the collection losses.

These measurement values also agree well with separate measurements of respon-

sivity of three Si bolometers built by Infrared Laboratories performed by Brownell [78] who measured responsivities of 2.5x10^4 V/W at both 119 um and 433 um wavelengths.

3.6.2 Heterodyne Receiver

Heterodyne receivers are coherent receivers which mix the electromagnetic field of the incoming photons with a local oscillating (LO) field producing a signal at the difference, or intermediate, frequency (IF). This measurement technique encodes the spectrum of the incoming signal over a range of input frequencies and retains information about the phase of the incoming wavefront. The resulting IF signal contains frequencies from the original signals but the amplitude is modulated at the difference frequency as shown in Fig. 3-31. Weak signals can be detected because the IF signal is downconverted to frequencies where low noise electronics can amplify the signal.

The heterodyne receiver employed in this experiment is a two stage heterodyne system such that the first IF signal is mixed with a second LO allowing for subsequent amplification. A diagram of the double heterodyne system is shown in Fig. 3-32. The system consists of a first stage with a 110-170 GHz Hughes mixer, a 110-170 GHz Insight Products BWO acting as the first LO, 38 dB gain (2 x P/N ZJL-3G) and a 800 MHz high pass (HP) filter (P/N SHP-800). The second stage consists of a Mini-Circuits 0.3-4.3 GHz mixer (P/N ZEM-4300), a 2.018 $\pm$0.001 GHz oscillator (P/N POS-2120W) acting as the second LO, 62 dB gain (2 x P/N ZFL-500HLN and P/N ZFL-500LN), and 150 MHz HP (P/N SHP-150) and 550 low pass (LP) (P/N SLP-500) filters. The RF input and LO1 were mixed in a 3 dB coupler before the first mixer. The output of the heterodyne system was analyzed using a FFT on a 8GS/s, 500 MHz oscilloscope.

The procedure for finding the SPR frequencies is to scan the BWO (LO1) frequency until a peak enters the active area of the FFT (< 500 MHz). A frequency is identified by finding the four peaks on the oscilloscope such that

$$f_{sp} = m f_{LO1} \pm f_{LO2} \pm \Delta$$

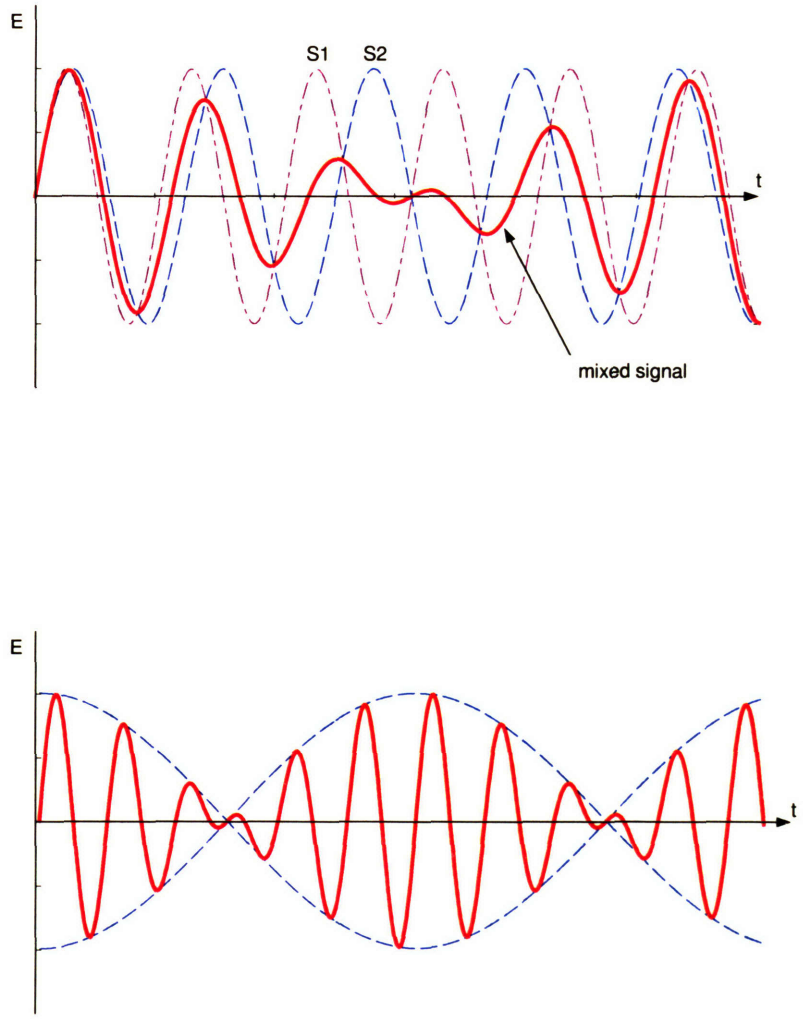

Figure 3-31: (a) Mixing of two signals, S1 and S2, with the result shown (solid). (b) The mixed signal illustrating the beating at the difference frequency. Adapted from [91].

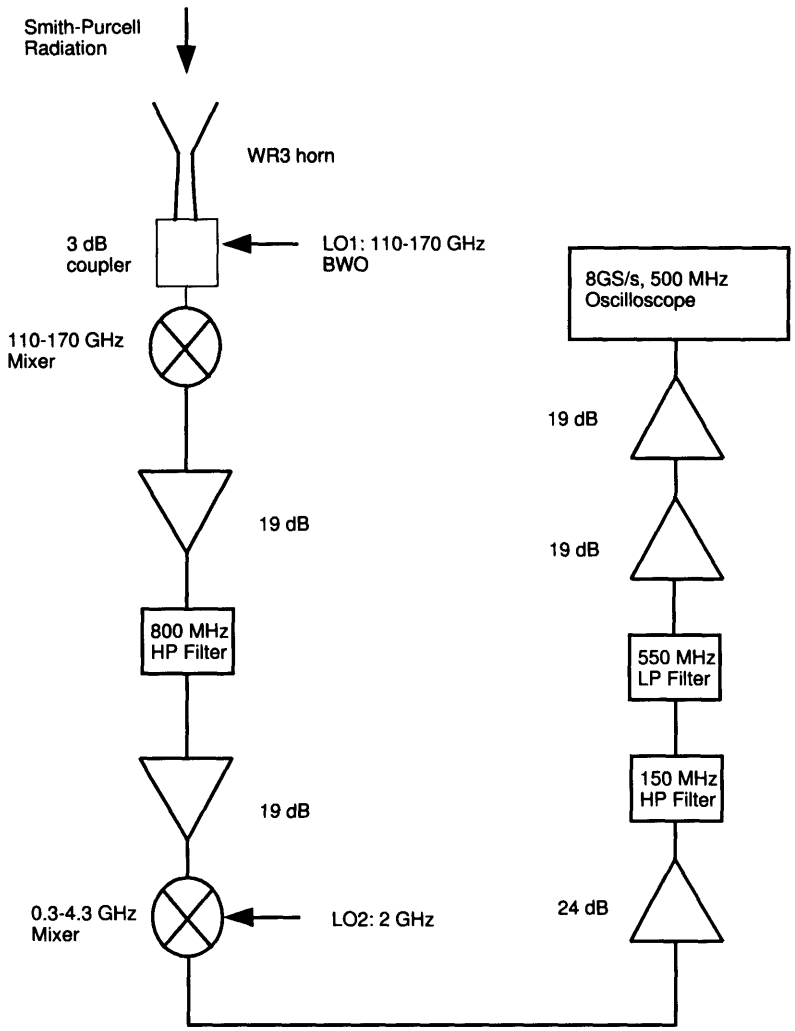

Figure 3-32: Schematic of double heterodyne frequency system.

where f_{sp} is the SPR frequency, f_{LO1} and f_{LO2} are the frequency of the first and second LOs respectively, m is the harmonic of the first LO and Δ is the frequency separation.

The BWO frequency is controlled via a high precision (± 0.5 mV) voltage supply and was calibrated using a different heterodyne receiver designed specifically for the frequency range 110-170 GHz. BWOs are typically unstable in both frequency and output power. The frequency drift was measured to be 5 MHz over 5 minutes. Identification of one f_{sp} typically took $\sim$ 5 minutes. Due to the large fluctuations in BWO output power and the lack of a broadband, calibrated THz source the heterodyne system was not able to be calibrated for energy. However, for a point of reference two sources were measured: a 140 GHz, $\sim$ 50 mW Impatt oscillator and the 250 GHz, 2 mW Gunn diode multiplier. The RF was input via WR7 (110-170 GHz) waveguide for both sources. For the 140 GHz source the amplitude of the FFT was 2V. No signal was measured for the 250 GHz source. The FFT was set to obtain the magnitude of the power spectrum using Blackman Harris windowing (for good sideband rejection). This gives a general idea of the power levels measured by the heterodyne receiver at the first harmonic of the first LO.

3.6.3 Radiation Beamline Components

Absorption

The emergent SPR passes through several components while travelling from the grating to the detector. It is important to note the absorption characteristics of each of these components. The radiation is reflected off the copper mirror, passes through a fused silica window, air, a wedged polyethylene window at the bolometer entrance, and a 100 μm high pass filter. Most of the components have relatively flat absorption characteristics across the wavelength range of the measured SPR spectrum (300 μm - 3 mm).

The reflection of the radiation off the copper mirror is assumed to be close to 100%. The transmission plot for the wedged polyethylene window is shown in Fig.

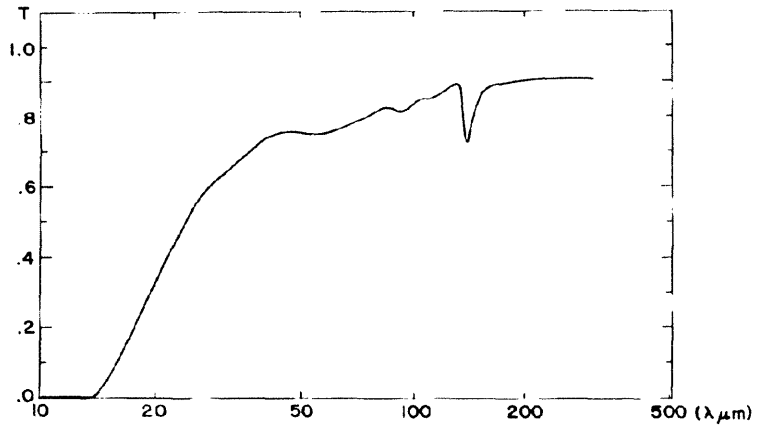

Figure 3-33: Plot of the measured Transmission (at 300 K) for 1 mm HI density Polyethylene Window coated with 5-10 m diamond on one side. Data supplied by Infrared Laboratories.

3-33. Above 300 μm the transmission is expected to approach 90% due to the reflections from the two surfaces of the window. The transmission plot for the 100 μm filter is shown in Fig. 3-34. Above 300 μm the transmission is expected to be 80% due to reflections from the four surfaces in the filter (the filter consists of two separate pieces). A 330 μm filter was supplied by Infrared Laboratories, however, no transmission plot was supplied. The transmission is assumed to be 90% above 330 μm due to the two surfaces.

The transmission through air has been measured in the literature [92,93]. Several plots of the different measurements are shown in Fig. 3-35 and Fig. 3-36. While the two figures do not match exactly they have generally similar shapes. In Fig. 3-35 the attenuation at the 1 THz absorption resonance is 800dB/km = 0.8 dB/m. For Fig. 3-36 the transmission is defined as 10 x optical density so at 1 THz the attenuation is 16 dB/10m = 1.6 dB/m. In this experiment the SP radiation travels less than 20 cms in air so the expected attenuation at 1 THz is 0.2 dB. For lower frequencies (down to 200 GHz) the attenuation should be about a factor of 10 lower. At frequencies higher that 1 THz the attenuation levels are approximately the same

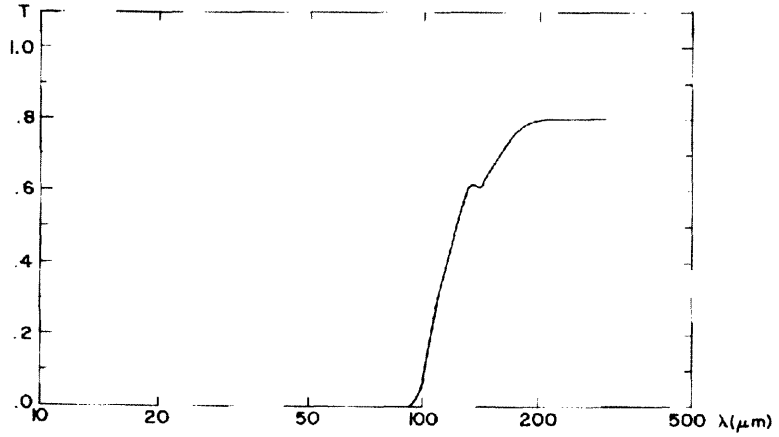

Figure 3-34: Plot of the measured Transmission (at 4 K) for the 100 μm filter composed of 0.8 mm crystalline Quartz with Garnet Powder. Data supplied by Infrared Laboratories.

as at 1 THz. Additionally, it is unlikely that we will notice the sharp absorption spectra due to atomic and molecular resonances because the SPR is broadband. We have chosen to ignore the effects of atmospheric absorption because the radiation is travelling over such a short distance.

The fused silica window is expected to contribute the most absorption of the SPR. Various authors have measured the absorption coefficient of fused silica [94–97]. A summary of data from several sources is shown in Table 3.7. It should be noted that is some disagreement between the authors measurements that is probably a result of measurement techniques and differences in sample. The only data point for the absorption coefficient that appears to be in good agreement between the various authors is that for 900 GHz, giving a value of 1.5 cm^{-1}. The thickness of the fused silica window on the SPR diagnostic chamber is 0.635 cm which can give transmission of $e^{-(1.5)(0.635)} \approx 40\%$ at frequencies close to 900 GHz and $e^{-(0.1)(0.635)} \approx 95\%$ at frequencies close to 300 GHz. Clearly, this absorption can produce a wavelength dependent affect on the measured SPR and the absorption must be factored into the measurements. A plot of the absorption coefficients from the literature and those

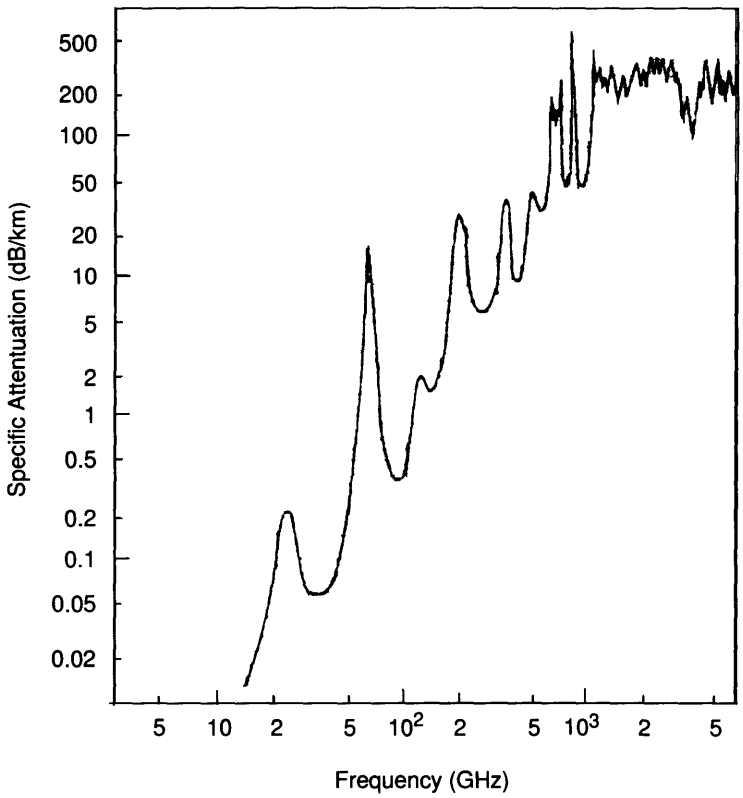

Figure 3-35: Plot of the measured absorption of the atmosphere. Adapted from [93].

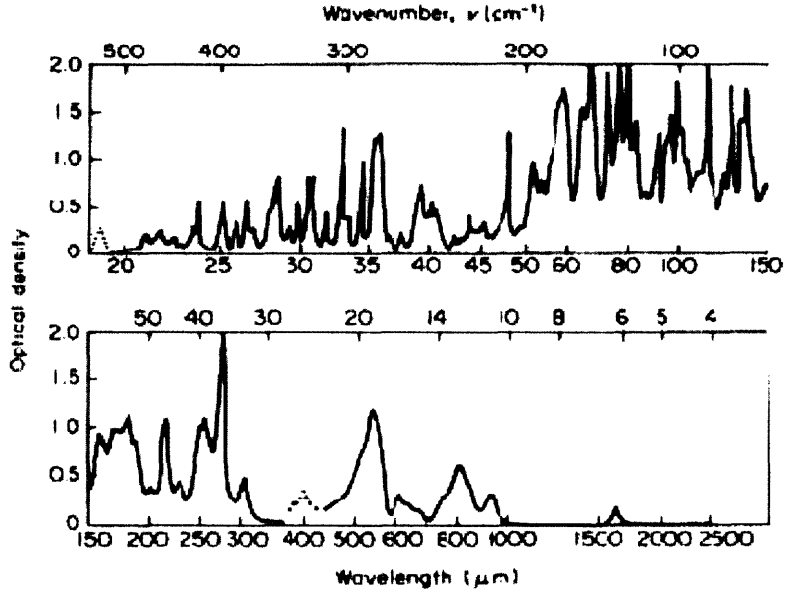

Figure 3-36: Plot of the measured absorption of the atmosphere. Optical density is defined as the logarithm to the base ten of the ratio of the incident to transmitted intensity. The data was taken for atmospheric air of thickness 10 m at a temperature of 20 °C, pressure 760 torr, and absolute humidity of 10.5 gm/m^3. [92]

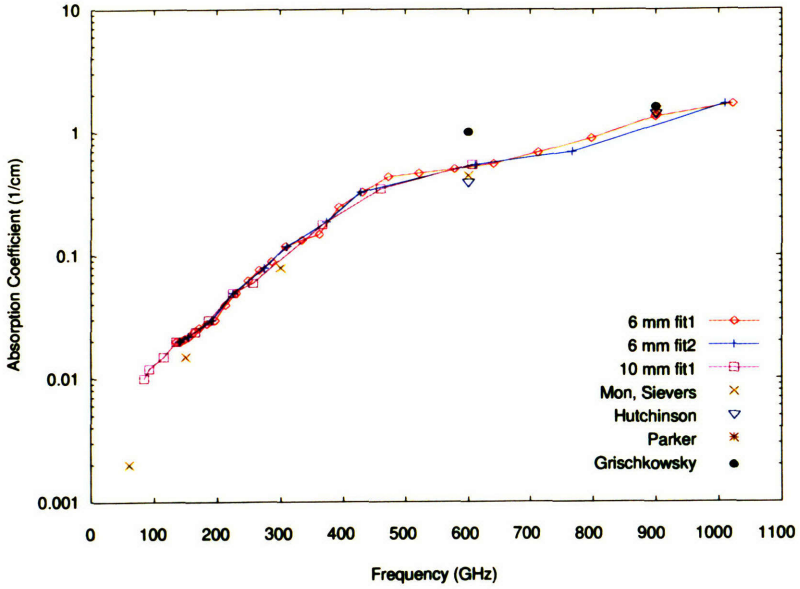

Figure 3-37: Fused Silica Absorption Coefficients used in the Data Analysis.

used in the data analysis are shown in Fig. 3-37.

Frequency	Absorption Coefficient [1/cm]			
[GHz]	Mon, Sievers [94]	Hutchinson [96]	Parker [95]	Grischkowsky [97]
60	0.002	-	-	-
150	0.015	-	-	-
300	0.08	-	-	-
600	0.45	0.4	-	1
900	1.5	1.44	1.5	1.6
1500	2.1	-	4.7	4

Table 3.7: Data on Absorption Coefficient of Fused Silica

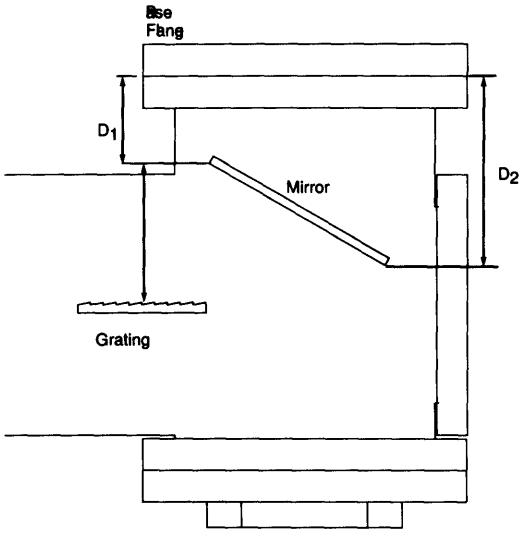

Figure 3-38: Schematic of the Mirror Measurement.

Alignment

The angle for the flat mirror was measured in two different ways. The first technique measured the physical location of the mirror. The second technique used a laser. For the first technique the distance of each end of the mirror from the base flange was measured as shown in Fig. 3-38. Additionally, the distance between the grating and mirror was measured. For the second method an alignment laser was placed at the detector location and the laser beam was reflected off the mirror. The location of the laser on the grating was then measured and the angle determined.

Detector Position

The location of the bolometer in relation to the vacuum chamber is shown in Fig. 3-39 . Two 3/8" collimators were placed between the window and the bolometer in order to restrict the measured radiation to a small angular aperture. The bolometer could be scanned along the window at a fixed distance from the window for a range of 4". The heterodyne receiver horn was placed 1.44" from the window and 0.4" left of center (upstream).

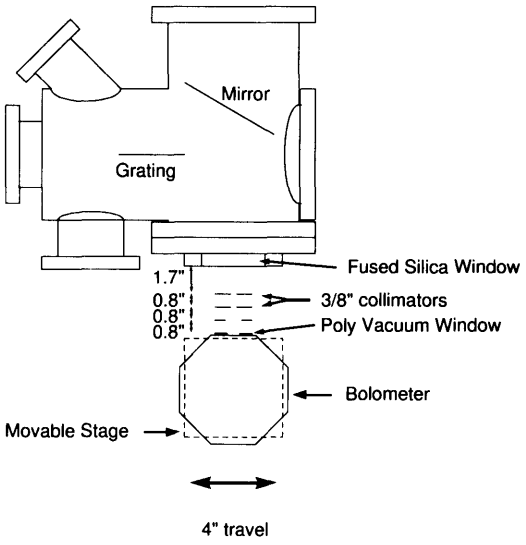

Figure 3-39: Location of the Bolometer with respect to the SPR vacuum chamber.

Chapter 4

Experimental Results

This chapter presents the experimental results obtained from the SPR experiment. The operation of the accelerator and determination of several beam parameters is described. Several experiments verifying that the radiation is SPR are described including measurement of the SP resonance condition, dependence on beam charge and dependence on beam height. The measurement of the angular distribution of SPR and subsequent bunch length determination are presented. Lastly, measurements of the frequency locked SPR with the double heterodyne receiver are shown.

4.1 HRC Accelerator Operation

Due to the nature of the accelerator facility at the PSFC the author operated the HRC accelerator. As a result, it was necessary for the author to understand and optimize the operation of the accelerator. First the correct settings for the three injector focusing lenses, the bias current and gun steering coils were determined. This involved maximizing the currents on beam monitor 1 (BM1) and beam monitor 2 (BM2). A typical BM2 trace is shown in Fig. 4-1. The beam monitors are calibrated so that 1 mV corresponds to 1 mA. The next step involved scanning the phase of the prebuncher while observing the current transmitted through the linac to obtain the correct injection phase.

Prior to the SPR experiment installation a spectrometer was located on the beam-

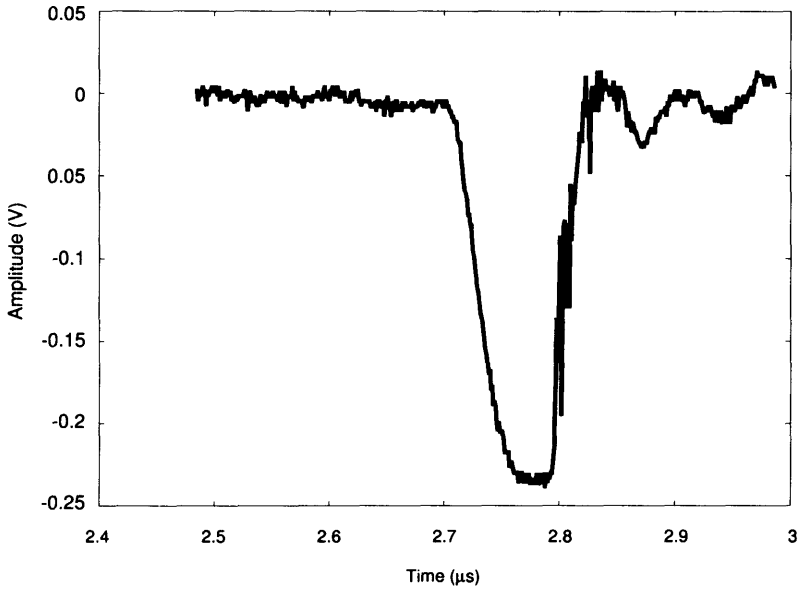

Figure 4-1: Plot of the beam monitor 2 signal.

line. The spectrometer allowed for a calibration of the beam energy from the total input power into the linac. The beam energy can subsequently be determined by

$$E_2 = E_1\sqrt{\frac{P_2}{P_1}} \tag{4.1}$$

A typical trace of the forward power into the linac for a beam energy of 15 MeV is shown in Fig. 4-2.

In addition to the beam monitors, a Faraday cup (FC) was installed at the end of the beamline in order to observe beam interception on the grating. The FC was terminated in 25 Ω so the current can be determined from the trace. A typical FC signal is shown in Fig. 4-3 corresponding to $\sim$ 150 mA of current. The FC signal was also used to optimize the toroidal focusing lens and steering coil settings.

A plot of a typical signal from the bolometer is shown in Fig. 4-4. The maximum value of the bolometer signal was taken to be the value for the signal intensity. Averaging over five shots was performed to obtain a final value, in order to minimize the shot to shot variations in charge, injection voltage and klystron power. These

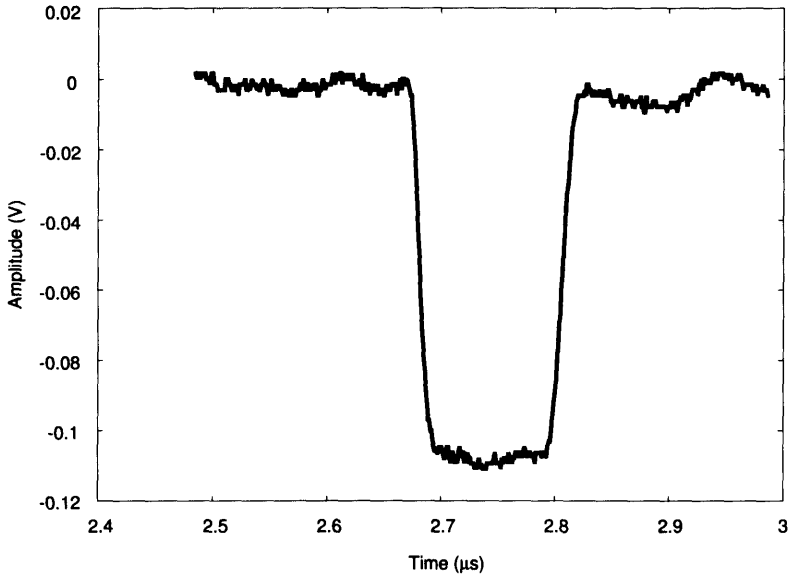

Figure 4-2: Plot of the linac forward power.

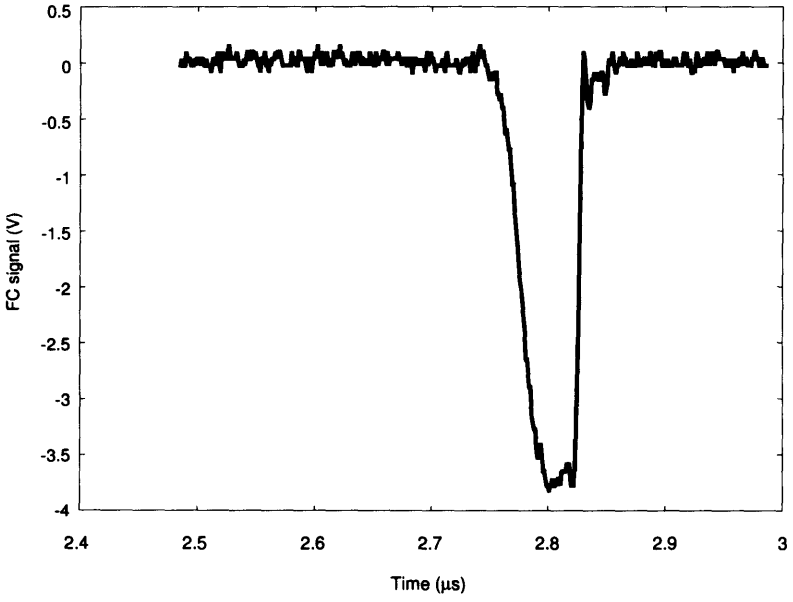

Figure 4-3: Plot of the Faraday cup signal.

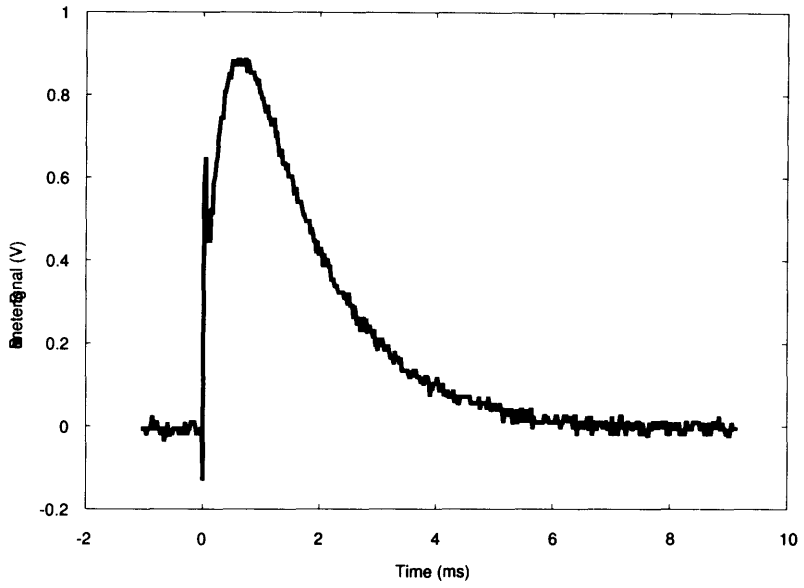

Figure 4-4: Plot of the bolometer signal.

fluctuations could lead to shot to shot variations in the signal as large as 10 percent if the linac settings were on the edge of a point of "stable" operation.

A typical IF signal from the heterodyne receiver is shown in Fig. 4-5. The IF signal was FFT with a 8 GS/s, 500 MHz oscilloscope. The LO1 frequency was scanned and the emission frequencies were determined by finding the four peaks that corresponded to a particular RF harmonic.

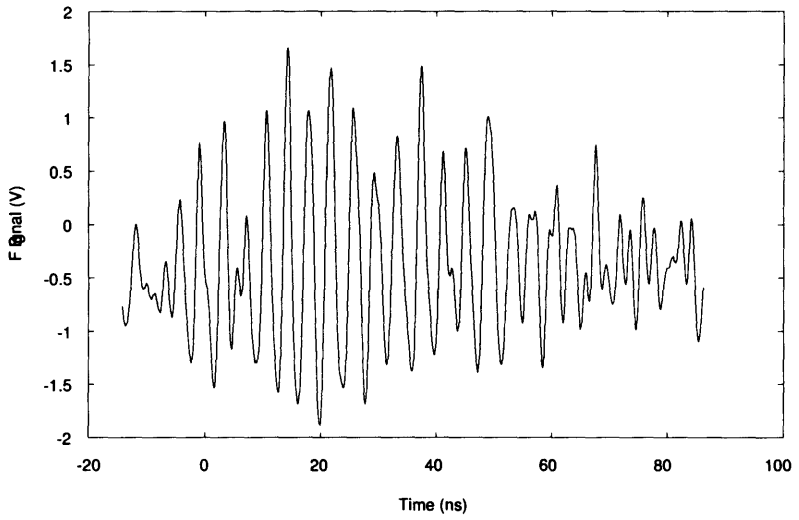

Figure 4-5: Plot of the IF signal from the double heterodyne receiver.

4.2 S-P Resonance Condition

The S-P resonance condition, $\lambda = l(\frac{1}{\beta} - \cos\theta)$, was measured with several band pass filters at the frequencies 183 GHz, 400 GHz, and 800 GHz, which were manufactured by Virginia Diodes. The theory of transmission of metal mesh filters in the far infrared was initially developed in [98] and [99]. The theoretical transmission curves (supplied by Virginia Diodes) for each of these filters is shown in Fig. 4-6, Fig. 4-7,

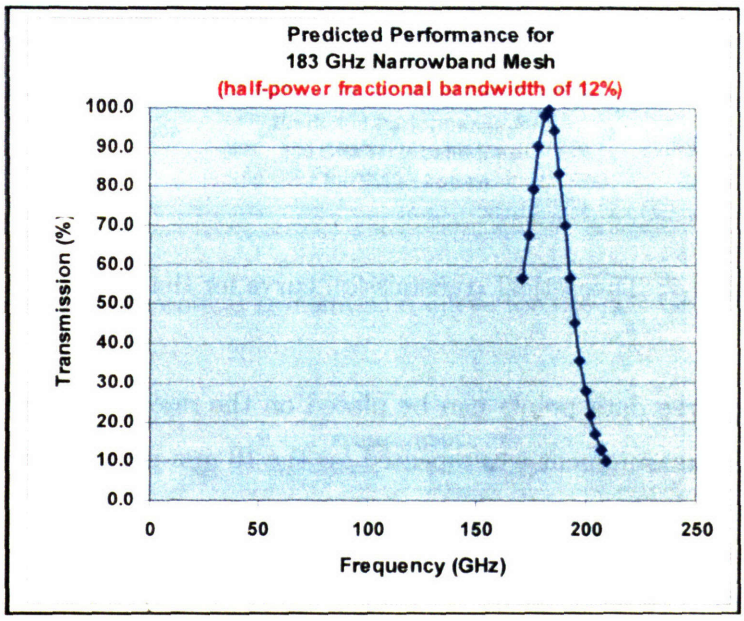

Figure 4-6: Theoretical transmission curve for the 183 GHz filter.

Fig. 4-8. The experimental transmission was measured by changing the angle of the mirror while keeping the detector fixed. Several of the transmission vs. angle measurements using the 6 mm grating are shown in Fig. 4-9. In order to account for long term drift ($\sim$ 10 minutes) in the modulator voltage and toroidal focusing lens the transmission is measured by scanning the mirror without the filter, then scanning the mirror with the filter twice and finally scanning the mirror without the filter again. A transmission value was computed by averaging the signal size with the filter divided by the signal without the filter. Based upon the transmission curves and the angle

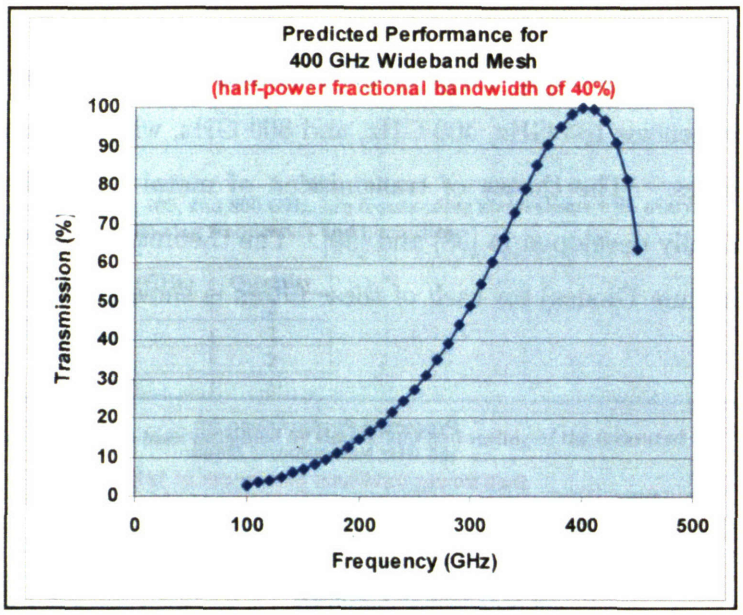

Figure 4-7: Theoretical transmission curve for the 400 GHz filter.

of observation three data points can be placed on the resonance curve as shown in Fig. 4-10. The measurement was repeated for the 10 mm grating and the resonance curve is shown in Fig. 4-11.

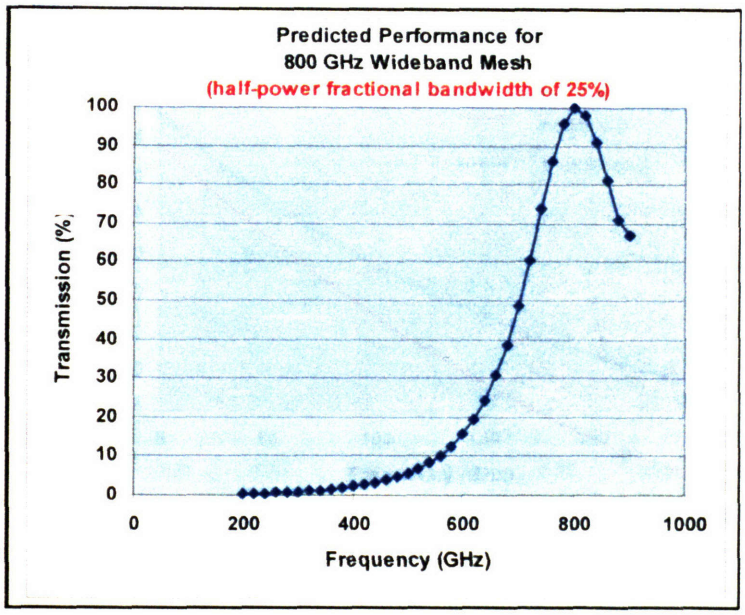

Figure 4-8: Theoretical transmission curve for the 800 GHz filter.

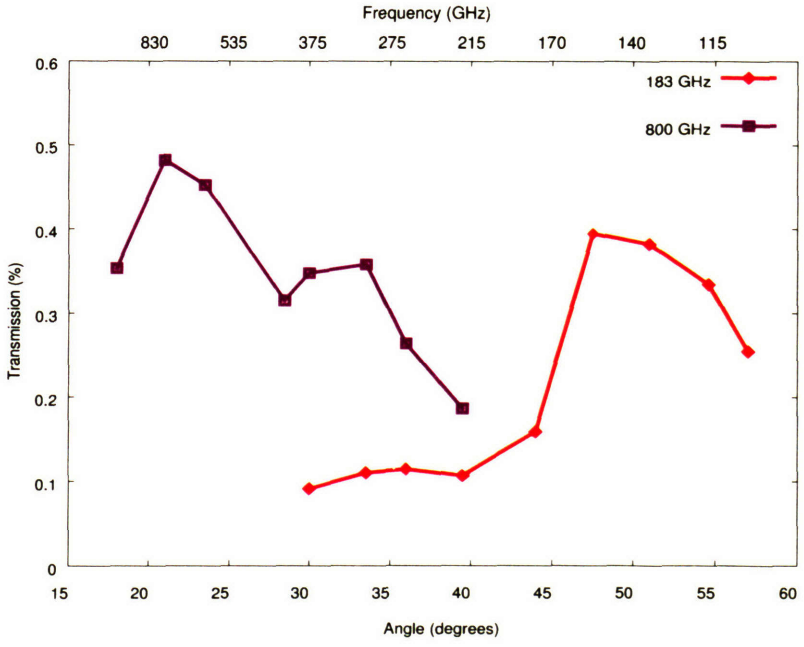

Figure 4-9: Plot of transmission percentages for the 183 GHz and 800 GHz filters vs. angle (frequency) using the 6 mm grating.

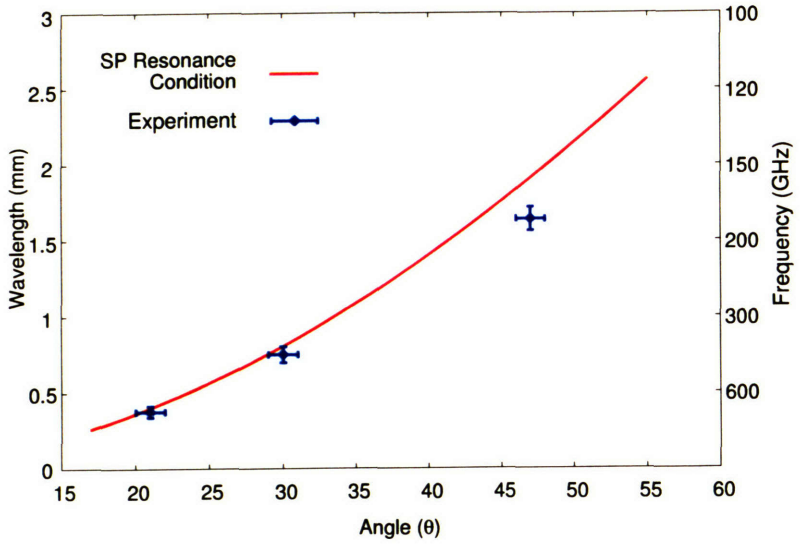

Figure 4-10: Plot of Smith-Purcell resonance condition for the 6 mm grating.

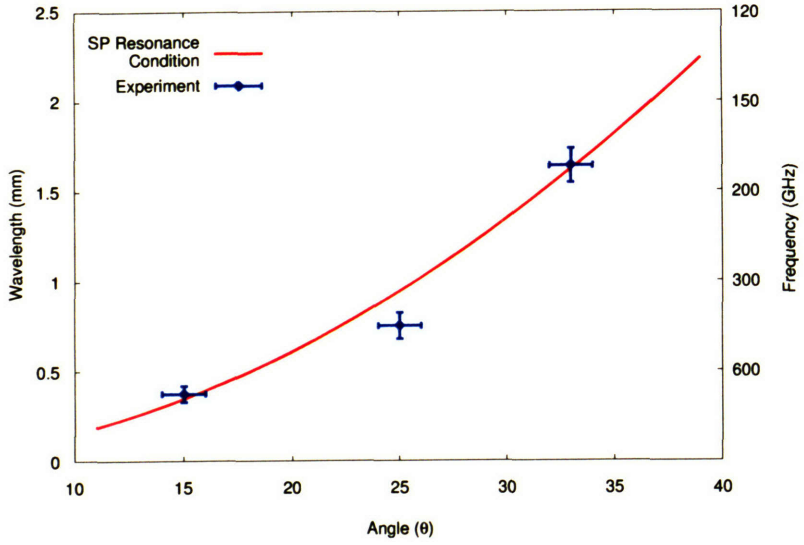

Figure 4-11: Plot of Smith-Purcell resonance condition for the 10 mm grating.

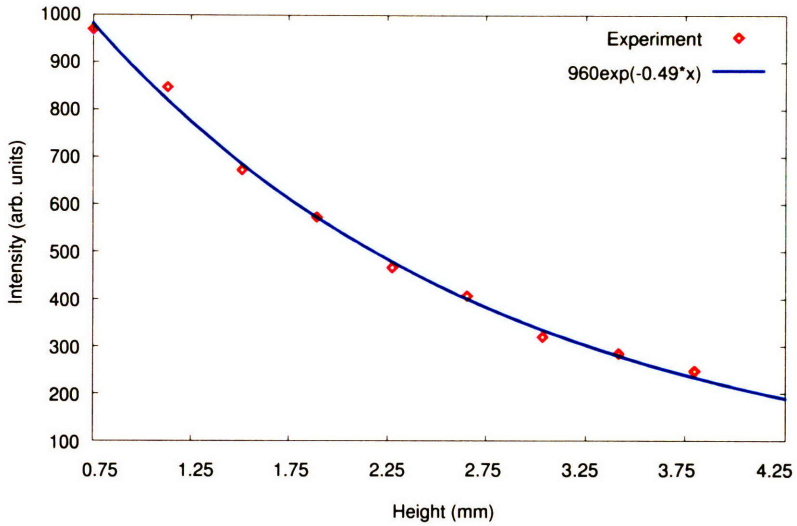

Figure 4-12: Plot of the dependence of SPR Intensity on beam height at a given observation angle. The beam has an energy of 15.5 MeV and the observation angle is 23.5°.

4.3 Beam Height

The dependence of the intensity of the Smith-Purcell radiation on the beam height, Eq. (2.19), scales as

$$\frac{\partial^2 I}{\partial\omega\partial\Omega} \sim e^{-\frac{4\pi b}{\gamma l(1-\beta\cos\theta)}}. \tag{4.2}$$

The beam height was varied by moving the grating away from the beam while the mirror and detector remained stationary. The mirror was kept at an observation angle of 23.5° and the grating period was 10 mm. The beam energy was 15.5 MeV and the current was held constant at 150 mA as well. A plot of the measured dependence of intensity on beam height is shown in Fig. 4-12. The fitted curve agrees well with the theoretical value of $\frac{\partial^2 I}{\partial\omega\partial\Omega} \sim e^{-0.4887b}$ for $\gamma = 31$, $\theta = 23.5°$, and $l = 10$ mm.

4.3.1 Beam Width

The beam transverse size at the grating location was measured by moving the grating into the beam and observing the FC signal. The beam spot size was adjusted via the toroidal focusing lens. The beam size was measured at the typical current setting for the toroidal focusing lens, 21 A, which corresponds to a magnetic field of 6 kG. The perpendicular beam profile can then be fitted via the current transmission. For a lens current of 21 A the beam FWHM was 1 mm as shown in Fig. 4-13.

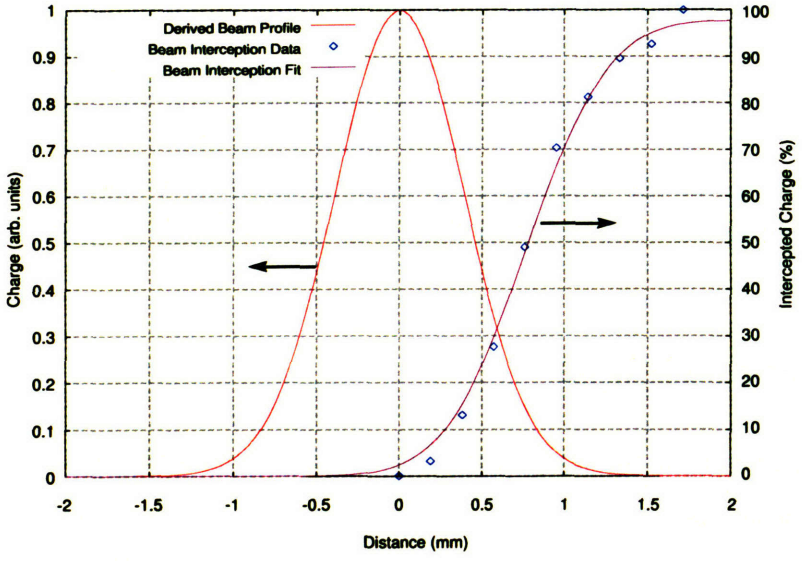

Figure 4-13: Least squares fit for the beam profile.

4.4 Beam Current

The beam current can be varied by adjusting either lens 1 or 2 (or both) in the injection system. This allows the input beam current to be raised or lowered without affecting the beam energy or pulse length. The beam parameters are considered constant until the current is increased enough to produce beam loading in the linac. Beam loading effects were typically observed at currents above 200 mA. The 10 mm grating was used and the mirror and detector positions were held fixed. The beam

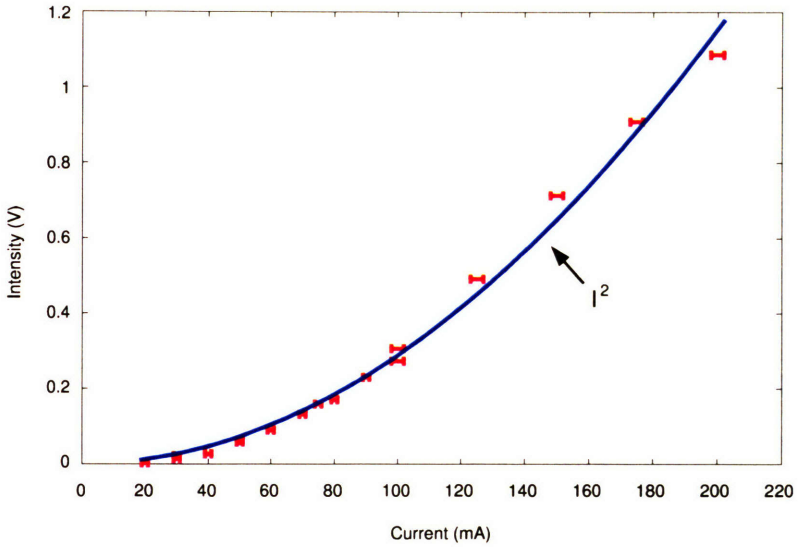

Figure 4-14: Plot of the dependence of SPR Intensity on beam current at a given observation angle. The beam has an energy of 15 MeV and the observation angle is 23.5°.

energy was 15 MeV. According to Eq. (2.79) the radiated energy should scale as I^2. The bolometer signal versus beam current is shown to scale as the square of the current in Fig. 4-14.

4.5 Angular Distribution

The angular distribution of SPR was measured by adjusting the mirror angle while moving the detector across the window in 3/8" steps. The measured intensity was then summed up for each detector position and angle to give the total radiation emitted at a particular angle. The values were then adjusted for absorption due to the fused silica window and normalized before comparing to the 3D EFIE code. Based on the calibration of the bolometer and the measured signal size (1 V) the typical energy values measured were $\sim 0.1\ \mu J$.

4.5.1 Prebuncher Only

A plot of the angular distribution of SPR for the 10 mm grating is shown in Fig. 4-15.

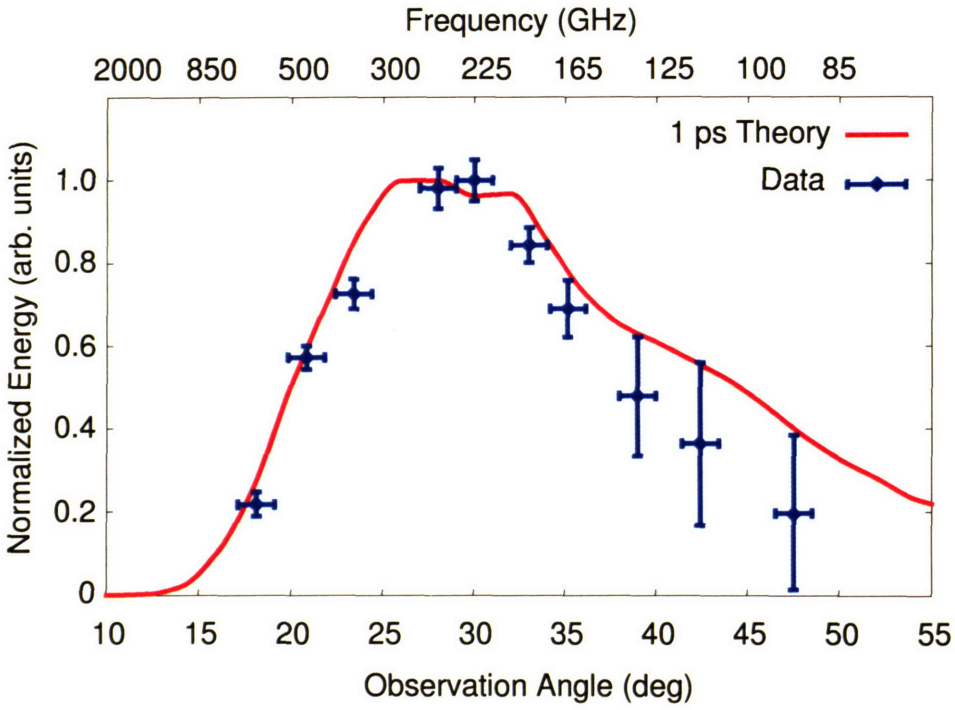

Figure 4-15: Comparison of the measured angular distribution of SPR to theory.

The beam was 15 MeV, 150 mA and 1 mm spot size. The power in the prebuncher

was 0.4 kW. Several different theoretical curves are plotted versus angle in Fig. 4-16.

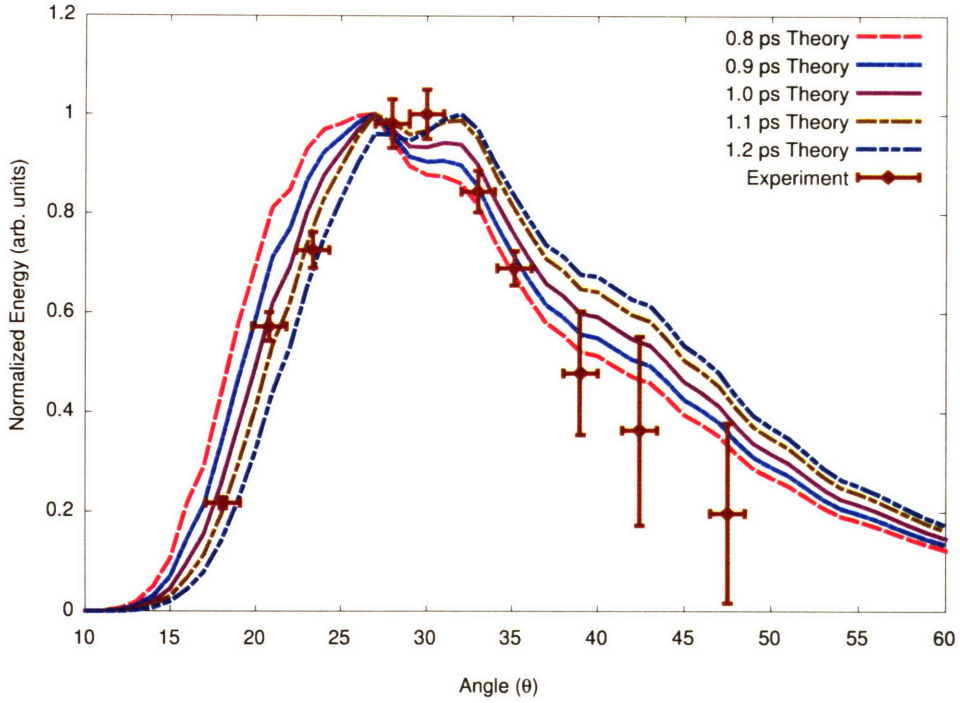

Figure 4-16: Comparison of the measured angular distribution of SPR to the theory for various bunch lengths.

The most important part of the curve for determining the bunch length is the drop off at high frequencies due to the loss of coherence. The bunch length was determined to be 1.0 ± 0.1 ps.

4.5.2 Chopper and Prebuncher

A plot of the angular distribution for the 6 mm grating is shown in Fig. 4-17. The beam was 15 MeV, 100 mA and 1 mm spot size. The power in the prebuncher was 1.2 kW while the power in the chopper was 1.1 kW. Several different theoretical curves are plotted versus angle in Fig. 4-18. The bunch length was determined to be 0.60 ± 0.1 ps.

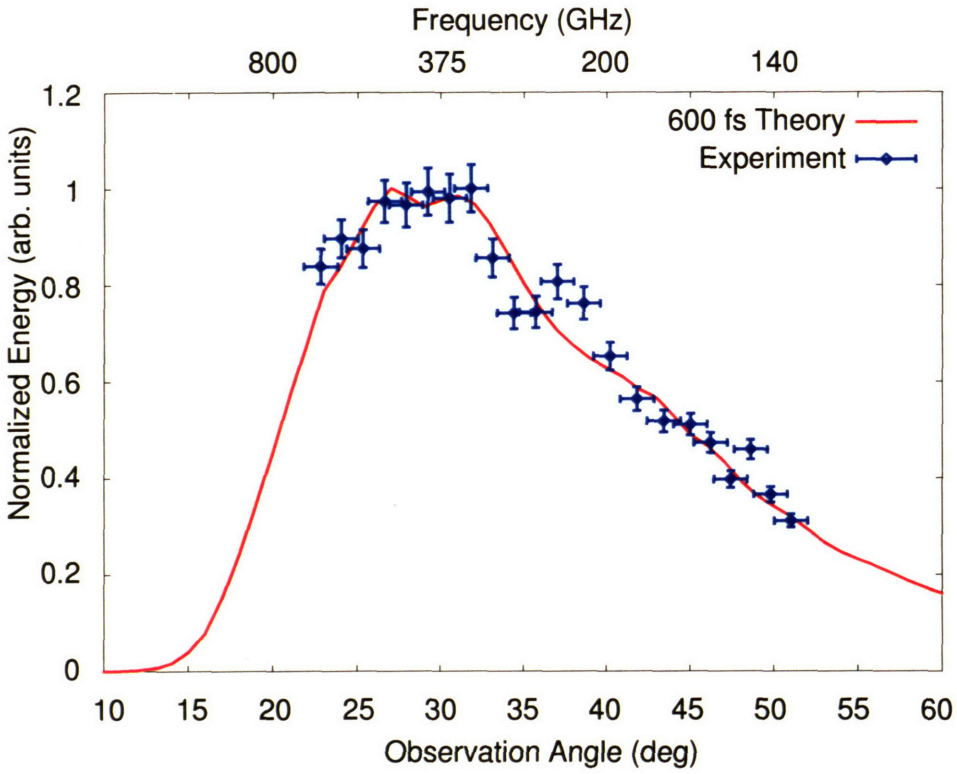

Figure 4-17: Comparison of the measured angular distribution of SPR to theory.

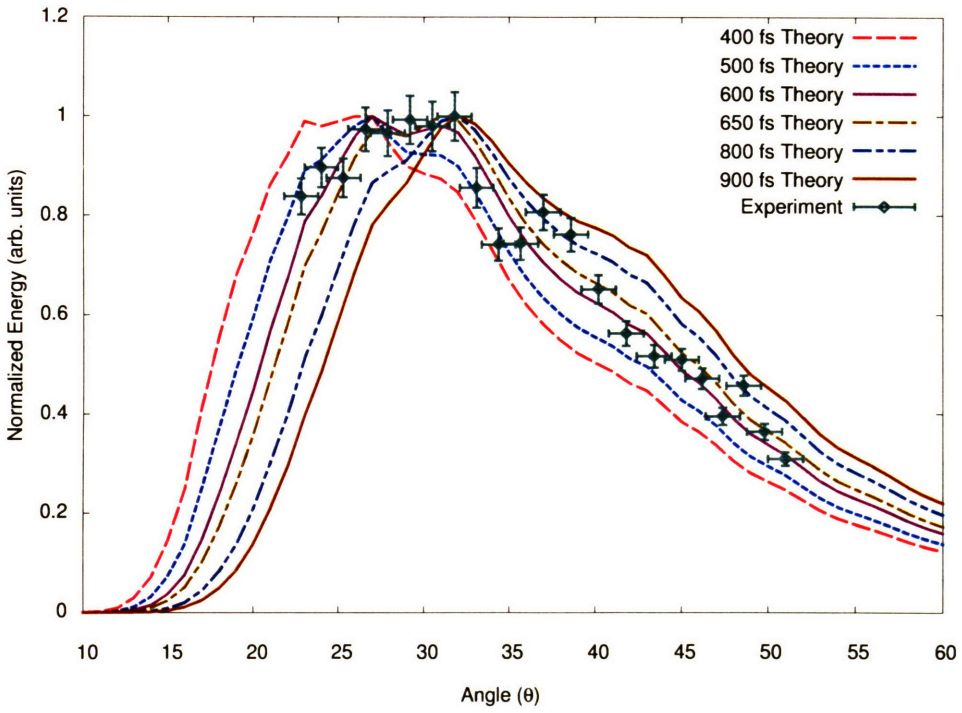

Figure 4-18: Comparison of the measured angular distribution of SPR to the theory for various bunch lengths.

4.5.3 Absolute Energy

A preliminary comparison of the measured absolute energy to theory can be performed. The 3D finite grating theory predicts a peak intensity of 1 nJ/str/groove/bunch for the 10 mm grating. The angular collection aperture is 5 x 10^{-4} str due to the 1 cm diameter collimator, 40 cm from the grating. The grating also has 10 grooves and there are 500 bunches. This gives an energy of 2.5 nJ at the detector. The peak signal measured by the bolometer is 1.2 V. The electrical responsivity of the detector is 2.63x10^5 V/W, the time constant of the detector electronics is 0.5 ms and the absorption of the beamline elements is $\sim$ 0.7. This gives a measured energy of 3.25 nJ.

4.6 Heterodyne Measurements

The double heterodyne receiver was used to measure the frequency spectrum of the SPR. A search in frequency space found only frequencies at integer multiples of the accelerator frequency. A table of all the measured frequencies is shown in Table 4.1. Each of the frequencies was identified by finding the four corresponding peaks. Each peak had a width of $\sim$ 25 MHz. Several harmonics were not able to be measured due to the available frequency range of the first LO and characteristics of the WR6 harmonic mixer.

For a mirror angle of 28° and a accelerator frequency of 17.140 GHz the measured frequencies are a plotted in Fig. 4-19. The slope of the fitted line matches the accelerator RF frequency to within 1 MHz. Small changes of order 5 to 10 MHz in the 17.140 GHz accelerator frequency resulted in comparable and reproducible changes in the FL-SPR frequencies.

The FFT for one of the peaks at 240 GHz is compared to theory in Fig. 4-20. The theoretical curve, Eq. (2.88b), which is computed for $N_b = 550$ ($\sim$32 ns) matches the data extremely well, even showing the 2^{nd} maxima in detail. The measured peak has a FWHM of 28 MHz. This is the first measurement of a transform limited bandwidth

Frequency [GHz]	RF Harmonic
120.09	7
137.23	8
154.35	9
240.07	14
257.22	15
291.49	17
308.62	18
325.75	19
377.04	22
394.29	23
411.44	24
428.58	25
462.89	27
480.05	28
514.26	30

Table 4.1: Frequencies Measured with the Double Heterodyne Receiver

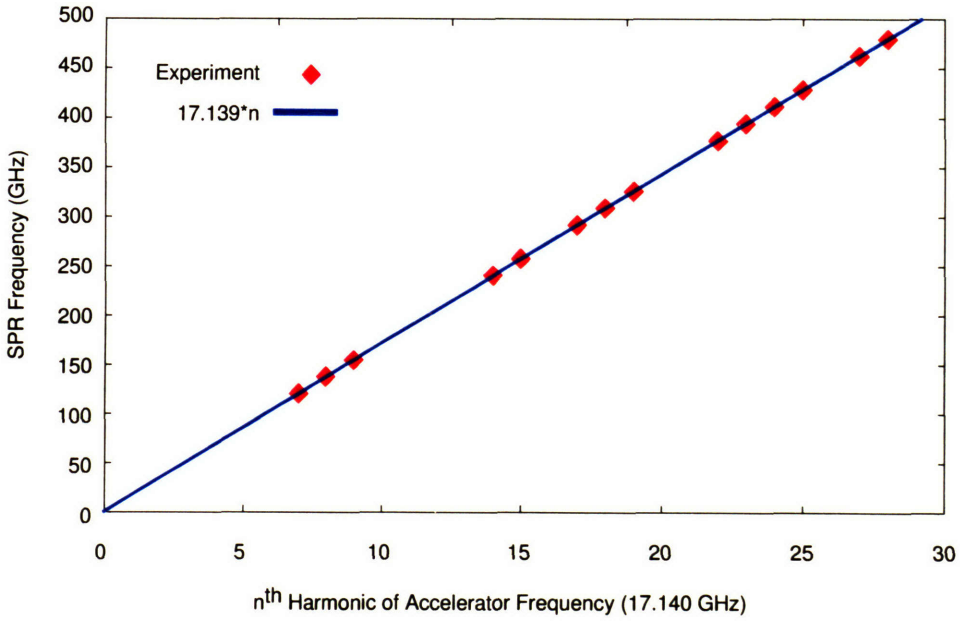

Figure 4-19: Plot of the SPR as measured by the double heterodyne receiver. Several harmonics were not able to be measured with the existing frequency system, but are presumed to be present.

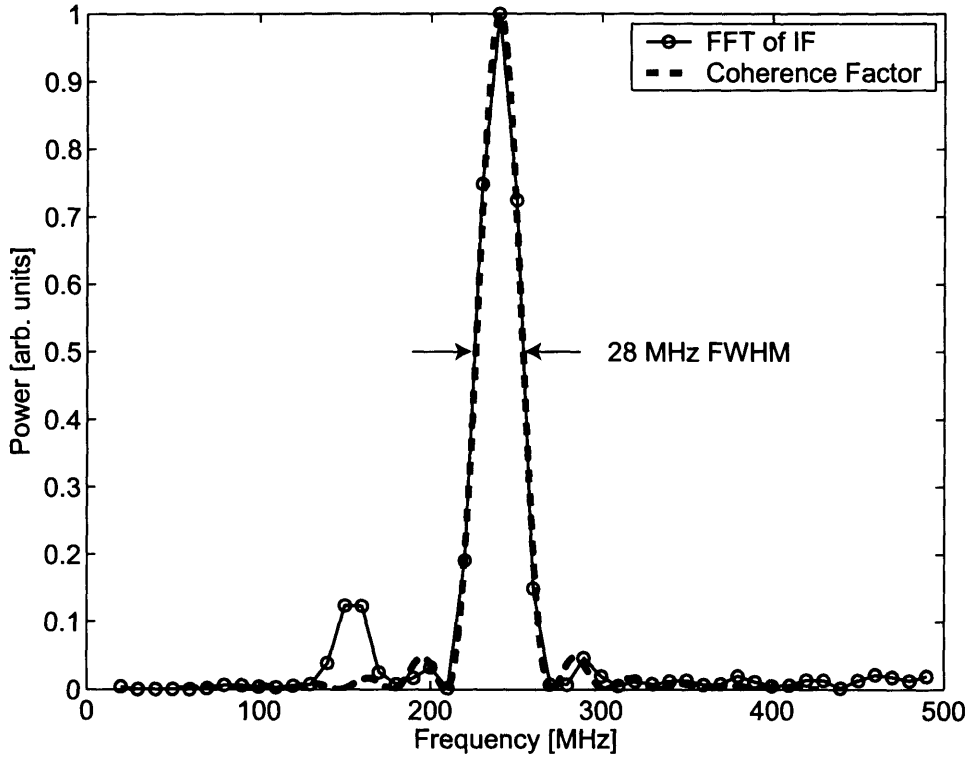

Figure 4-20: Comparison of the measured power in the FFT of the IF signal from the SPR and the theoretical prediction. The peak corresponds to a radiation frequency of 239.96 GHz (14th harmonic) and has 28 MHz FWHM. The theoretical curve is calculated using Nb = 550. The small peak at 170 MHz is due to low frequency noise in the heterodyne system and is present at all times.

due to the number of bunches in a pulse train. The small peak at 170 MHz is due to low frequency noise in the heterodyne receiver and is present at all times.

Chapter 5

Conclusion and Discussion

5.1 Conclusion

An experiment to measure SPR from a train of 15 MeV, 9pC bunches of electrons produced by a 17 GHz high gradient accelerator was designed, built and operated. The accelerator is unique because it can produce a variety of bunch lengths ranging from $\sim$ 200 fs to 1.5 ps. The SPR experiment demonstrates three unique results: 1) the ability use SPR radiation as a non-destructive bunch length diagnostic for sub-picosecond electron bunches, 2) measurement of frequency locked SPR with a transform limited bandwidth and an overall intensity enhancement of $N_g N_e N_b$, 3) the possibility of using SPR for the production of powerful THz radiation.

Two theoretical models for SPR were presented: the image charge theory and the diffracted wave theory. The author collaborated on the development of a new diffracted wave theory that takes into account finite grating effects. The effects of having multiple electrons in a bunch and multiple bunches in a train were discussed. PARMELA simulations of the accelerator under different operating conditions were presented. The image charge theory was used to design several different gratings measure bunch length over the expected range.

The SP resonance condition was measured for the 6 and 10 mm gratings using a set of three bandpass filters. The quadratic dependence of the SPR on beam current was measured as well as the exponential dependence on beam height. Comparison

of the angular distribution of radiation from the 6 and 10 mm gratings with theory obtained bunch lengths of 0.60 ± 0.1 ps and 1.0 ± 0.1 ps, respectively. This is the first subpicosecond bunch length measurement using SPR and improves upon the previous measurement by almost two orders of magnitude. The experiment demonstrates the use of SPR as a non-destructive bunch length measurement technique with 100 fs resolution. The measured values agree with an independent measurement using the HRC beam deflection technique [100].

The SPR from the 10 mm grating was measured using a double heterodyne receiver. These measurements are the first demonstration of frequency locking at the RF harmonics for SPR. Frequencies up to 514 GHz (30th harmonic) were observed. The measurement was also the first demonstration of a transform limited bandwidth due to the $\sim$ 30-40 ns of steady state beam for any coherent radiation generation technique. A linewidth of 28 MHz was measured with an accuracy of 1 part in 10,000. The radiation intensity enhancement factor of $N_g N_e N_b$ has been measured for the first time. Energies of 0.15 μJ in a collection aperture of 10 mrad were measured with the Si bolometer, which corresponds to $>$ 1 W average power during the pulse. A relatively flat power level over a wide frequency range was seen. These power levels are very high when compared to other THz radiation sources. A summary of several of the most common THz sources and their respective power levels is shown in Table 5.1.

	Optically pumped THz lasers	Time domain sources	Backward wave oscillators	Direct multiplied sources	Frequency mixing	Smith-Purcell Radiation
Power	> 100 mW	~1μW	10 mW	mW-μW	mW-μW	1 W
Useable range [THz]	0.3-10	0.1-2	0.1-1.5	0.1-1 THz	0.3-10	0.1-5 THz
Tunability	Discrete lines	N/A	200 GHz	~10-15% of center f	Continuous	Discrete Lines
CW/pulsed	CW or pulsed	Pulsed	CW	CW	CW	Pulsed
Turnkey system?	Yes	Yes	No	Yes	No	No

Table 5.1: Summary of Terahertz Sources

5.2 Discussion

This experiment advances the understanding and potential uses for SPR however, some questions and issues are still left unanswered. Perhaps the biggest question is the agreement between theory and experiment for the absolute energy radiated. The radiated energy predicted by the image charge and electric field integral equation theories can differ by as much as one to two orders of magnitude. While it is not necessary to know the absolute energy for a bunch length measurement the possibility of performing a measurement by direct comparison of the measured energy exists. Order of magnitude agreement was obtained in this experiment, however, if good agreement is desired a separate experiment would need to be designed to specifically account for radiation losses and use well calibrated detectors. Additionally, the measurement would be best performed at a lower frequency (< 150 GHz) due to the availability of sources and the lower losses in the fused silica window.

Several sources of noise were present in this experiment and should be discussed. The background noise that was present was usually about 10% of the peak signal. This noise was observed when either the mirror angle was adjusted to a range where no radiation should be reflected out of the chamber or when the detector was moved to a section of the window where no radiation should be exiting. This noise is most likely SPR that is emitted from the grating and bounces around the vacuum chamber before exiting the window (e.g. radiation emitted at higher angles). The overall sensitivity of the bunch length measurement to this noise was considered small because it was present at all detector locations. In several experiments there occasionally was noise seen at angles slightly higher and lower than 20°. This is most likely transition radiation from edge or halo electrons impinging upon the grating. The transition radiation should be directed at angles of twice the blaze angle $\pm 1/\gamma$. The transition radiation noise was typically small and could be reduced by moving the beam away from the grating.

The uncertainty in the value of the absorption coefficient of fused silica could lead to errors in the bunch length measurement. The effect due to small changes, i.e. less

than a factor of 2 in the values of the window absorption coefficient produced changes of less than a few percent in the intensity at each angle. These small intensity changes resulted in shifts the peak intensity of less than 1°. The calibration of the mirror angle could also give an error in the bunch length. When the mirror position was measured multiple times there were occasionally small differences in the measured angle, typically of the order of 1°. While the method of changing the mirror angle was sufficient for this experiment a different mirror scheme which rotates the mirror angle around an axis centered on the grating may perform better.

Several limits on the bunch length measurement system were encountered. The primary limit occurs when the accelerator is run for very short bunches. Short bunches are produced by sweeping the injected beam across a collimator with the DC bias field. For very high DC bias settings, i.e. short bunches, the amount of charge is reduced by a factor of three. The results is an order of magnitude reduction in radiated energy. The signal becomes of the order of the noise and prevents a measurement of very short bunches. Fortunately, this is not a problem with the measurement technique but rather the beam properties of the accelerator.

Although the curved mirror was utilized several times the measured results were difficult to interpret. This could be a result of poor alignment or diffraction of the SPR. Even though the energy levels were quite high ($\sim \mu J$) the SPR was not detectable with the Scientech pyroelectric detector. Lastly, only Gaussian beam profiles for the longitudinal distribution were used in the 3D diffracted wave theory and the theory could be expanded to include other profiles. However, from the circular deflection cavity experiments the beam was seen to have a Gaussian shape.

The bunch lengths observed here are in agreement with independent measurements from the HRC deflecting cavity [100]. Unfortunately, due to laboratory constraints, it was not possible to run both experiments simultaneously to obtain an immediate comparison. It would be very interesting to make this comparison. By decreasing the noise and improving the error in angle the sensitivity of the measurement could potentially be improved. The results of this experiment show that a SPR diagnostic could have a big impact on FEL's and next generation linear colliders.

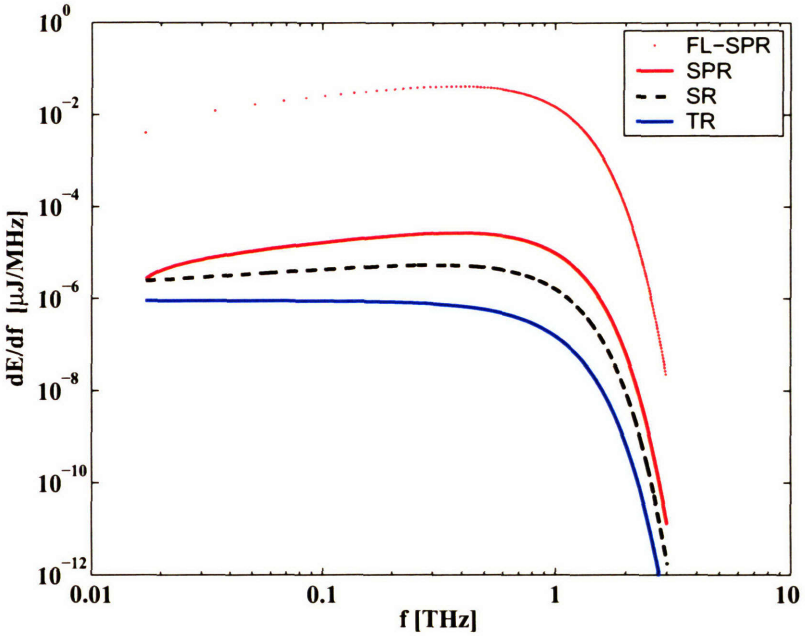

Figure 5-1: Plot of the calculated energy density for various radiation mechanisms using the MIT beam parameters: a 15 MeV beam consisting of 1500 bunches of 6×10^7 electrons (9pC) with 0.5 ps bunch length.

One of the most promising uses of SPR is as a THz source. Due to the inherent enhancement by N_g, SPR has the potential to produce higher power radiation than other techniques like synchrotron or transition radiation. A theoretical comparison of the three radiation mechanisms using the MIT electron beam is shown in Fig. 5-1. For the SPR calculation the beam centroid is 0.5 mm above the grating. The grating consists of 10 periods, having 1 cm periodicity and 10° blaze angle. The frequency locked SPR is show as points for clarity. Each point is actually a delta function of width $1/N_b$. Although the energy density in each peak is N_b higher, the power is the same for both the frequency locked SPR and normal SPR. For the synchrotron radiation (SR) calculation the bending magnet radius is 1 m and for the transition radiation (TR) calculation the foil is considered to be infinite in width. It is clear from the figure that the energy densities for the FL-SPR are four orders of magnitude higher than that of SR. SPR also has the added advantage that a

specific frequency can be chosen by restricting the collection optics to a small angular range. Frequency step tuning could then be obtained by tuning the mirror. This SPR experiment uses a compact RF accelerator to produce high power levels (>1 W) comparable to those seen at larger facilities like Jefferson Lab. Coherent SPR can produce several orders of magnitude higher energy and power levels than coherent SR and should be considered for THz radiation production at light sources.

Bibliography

[1] S. Smith and E. Purcell, Phys. Rev., Vol. 92, pp. 1069 (1953).

[2] G. Kube, et.al., Phys. Rev. E, Vol. 65, 056501 (2002).

[3] J.H. Brownell, et.al., Nucl. Instr. and Meth. in Phys. Res. A, Vol 393, pp. 323-325 (1997).

[4] G. Doucas, et.al., Int. Jo. Inf. and Mil. Waves, Vol 24, pp. 829-844 (2003).

[5] G. Doucas, et.al., Phys. Rev. Lett., Vol. 69, pp. 1761-1764 (1992).

[6] K.J. Woods, et.al., Phys. Rev. Lett., Vol. 74, pp. 3808-3811 (1995).

[7] Y. Ishi, et.al., Phys. Rev. E, Vol. 51, pp. R5212-5215 (1995).

[8] Y. Shibata, et.al., Phys. Rev. E, Vol. 57, pp. 1061-1074 (1998).

[9] D.C. Nguyen, Nucl. Instr. and Meth. in Phys. Res. A, Vol. 393 pp. 514-518 (1997).

[10] M.C. Lampel, Nucl. Instr. and Meth. in Phys. Res. A, Vol. 385 pp. 19-25 (1997).

[11] R. B. Palmer, Annual Rev. Nucl. Part. Sci., Vol. 40, pp. 529-592. (1990).

[12] G. A. Loew, Beam Line, Vol. 2, No. 4, p. 21 (1992) and the Proceedings of LC-92.

[13] M. Tigner, Proc. of Adv. Acc. Concepts, AIP Conf. Proc. 279, AIP Press, New York, p. 1-15 (1993).

[14] R. H. Siemann, Proc. of 1993 Particle Accelerator Conf., IEEE Catalog Number 93CH3279-7, IEEE Press, Piscataway, NJ, p. 532-534 (1993).

[15] J. S. Wurtele, Physics Today, Vol. 47, No. 7, pp. 33-40 (1994).

[16] R. Brinkmann, Proc. of 1999 Particle Accelerator Conf., IEEE Catalog No. 99CH36366, IEEE Press, Piscataway, NJ, p. 16-20 (1999).

[17] T. O. raubenheimer, Proc. of 1999 Particle Accelerator Conf., IEEE Catalog No. 99CH36366, IEEE Press, Piscataway, NJ, p. 16-20 (1999).

[18] International Linear Collider: Technical Report Committee, Second Report, SLAC-R-606, (2003).

[19] J. LaClare, Proc. of the Workshop on Fourth Generation Light Sources, Grenoble, France, (1996).

[20] A. Lumpkin, Nucl. Inst. and Meth. in Phys. A, Vol. 393, pp. 170-177 (1997).

[21] B. Faatz, et.al., Nucl. Inst. and Meth. in Phys. A, Vol. 407, pp. 302-306 (1998).

[22] E.L. Saldin, et.al., Nucl. Inst. and Meth. in Phys. A, Vol. 429, pp. 197-201 (1999).

[23] B. Carlsten, Micro Bunches Workshop, AIP Conf. Proc. 367, pp. 21 (1995).

[24] A. H. Lumpkin, Micro Bunches Workshop, AIP Conf. Proc. 367, pp. 327 (1995).

[25] A.H. Lumpkin, et.al., Nucl. Instr. and Meth. in Phys. Res. A, Vol. 445, pp.356-361 (2000).

[26] A. H. Lumpkin, Nucl. Instr. and Meth. in Phys. Res. A, Vol. 259, pp. 13-18 (1987).

[27] A. H. Lumpkin and M.D. Wilke, Nucl. Instr. and Meth. in Phys. Res. A, Vol. 331, pp. 803-808 (1993).

[28] M. Uesaka, et.al., Nucl. Instr. and Meth. in Phys. Res. A, Vol. 406, pp. 371-379 (1998).

[29] T. Watanabe, et.al., Nucl. Instr. and Meth. in Phys. Res. A, Vol. 480, pp. 315-327 (2002).

[30] J. Haimson, IEEE Trans. on Nucl. Sci., No. 3, pp. 996-1011 (1965).

[31] R.H. Miller et.al., IEEE Trans. on Nucl. Sci., No. 3, pp. 804-808 (1965).

[32] D.X. Wang, G.A. Krafft, and C.K. Sinclair, Phys. Rev. E 57, 2283 (1998).

[33] J. Haimson, et.al. Adv. Acc. Concepts, AIP Conf. Proceedings 647, AIP Press, New York, pp. 810-820 (2002).

[34] R.H. Milburn, Phys. Rev. Lett., Vol. 10, pp. 75-77 (1963).

[35] F.R. Arutyumian and V.A. Tumanian, Phys. Lett., Vol. 4, p. 176 (1963).

[36] W.P. Leemans, et.al, Phys. Rev. Lett., Vol. 77, pp. 4182-4185 (1996).

[37] I. Wilke, et.al., Nucl. Instr. and Meth. in Phys. Res. A, Vol. 483, pp. 282-285 (2002).

[38] X. Yan, et. al., Phys. Rev. Lett., Vol. 85, pp. 3404-3407 (2000).

[39] G. Berden, et. al., Phys. Rev. Lett., Vol. 93, pp. 114802-1 (2004).

[40] M.S. Zolotorev and G.V. Stupakov, SLAC-PUB 0-7132, 1996; in Proc. of 1997 Particle Accelerator Conference (IEEE Piscataway, NJ 1998).

[41] P. Catravas, et.al., Phys. Rev. Lett., Vol. 82, pp. 5261-5264 (1999).

[42] U. Happek, E.B. Blum, A.J. Sievers, Phys. Rev. Lett., Vol. 67, pp. 2962-2965 (1991).

[43] Y. Shibata, et.al., Phys. Rev. A., Vol. 45, pp.R8340-8343 (1992).

[44] K. Ishi, et.al., Phys. Rev. A, Vol. 43, pp. 5597-5604 (1991).

[45] D.X. Wang, et.al., Appl. Phys. Lett., Vol. 70, pp. 529-531 (1997).

[46] Y. Shibata, et.al., Phys. Rev. E, Vol. 52, pp. 6787-6794, (1995).

[47] A.H. Lumpkin, et.al., Nucl. Instr. and Meth. in Phys. Res. A, Vol. 475, pp. 470-475 (2001).

[48] G. Doucas, et.al., Phys. Rev. Spec. Top. - Acc. and Beams, Vol. 5, 072802 (2002).

[49] J.C. Wiltse, IEEE Trans. Microwave Theor. Tech., Vol. 32, pp. 1118-1127 (1984).

[50] P. H. Siegel, IEEE Trans. Microwave Theor. Tech., Vol. 50, pp. 910-928 (2002).

[51] B.B. Hu and M.C. Nuss, Opt. Lett., Vol. 20, pp. 1716-1718 (1995).

[52] D.M. Mittleman, et.al., IEEE J. Sel. Top. Quantum Electron., Vol. 2, pp. 679-692 (1996).

[53] D.M. Mittleman, et.al., App. Phys. B, Vol. 68, pp. 1085-1094 (1999).

[54] M.C. Beard, et.al., J. Phys. Chem. B, Vol. 106, pp. 7146-7159 (2002).

[55] G.L. Carr, et.al., Nature, Vol. 420, pp. 153-156 (2002).

[56] M. Abo-Bakr, et.al., Phys. Rev. Lett., Vol. 90, 094801 (2003).

[57] J.M. Byrd, et.al., Phys. Rev. Lett., Vol. 89, 224801-1 (2002).

[58] W.P. Leemans, et.al., Phys. Rev. Lett., Vol. 91, 074802-1 (2003).

[59] F.R. Buskirk and J.R. Neighbours, Phys. Rev. A, Vol. 28, pp. 1531-1538 (1983).

[60] Y. Shibata, et.al., Phys. Rev. A, Vol. 44, pp. R3445-R3448 (1991).

[61] T. Takahashi, et.al., Phys. Rev. E, Vol. 48, pp. 4674-4677 (1993).

[62] F. Ciocci, et.al., Phys. Rev. Lett., Vol. 70, pp. 928-931 (1993).

[63] Y. Shibata, et.al., Phys. Rev. Lett., Vol. 78, pp. 2740-2743 (1997).

[64] C.R. Jones, et.al., Appl. Phys. Lett., Vol. 67, pp. 1483-1485 (1995).

[65] J. Walsh, K. Woods, S. Yeager, Nucl. Instr. and Meth. in Phys. Res. A, Vol. 341, pp. 277-279 (1994).

[66] J.H. Brownell, J.E. Walsh, and G. Doucas, Phys. Rev. E, Vol. 57, pp. 1075-1080 (1998).

[67] G. Toraldo di Francia, Nuovo Cimento, Vol. 16, pp. 61-77 (1960).

[68] P.M. van den Berg, J. Opt. Soc. Am., Vol. 63, pp. 1588-1597 (1973).

[69] J.D. Jackson, Classical Electrodynamics, 3rd ed. (Wiley, New York, 1999).

[70] I.S. Gradshteyn and I.M. Ryzhik, *Table of Integrals, Series, and Products* (Academic Press, San Diego, 2000).

[71] R. Petit and D. Maystre, Rev. Phys. Appl., Vol. 7, pp. 424 (1972).

[72] P.M. van den Berg, Appl. Sci. Res., Vol. 24, pp. 261-293 (1971).

[73] O. Haeberle, et.al., Phys. Rev. E, Vol. 49, pp. 3340-3352 (1994).

[74] A. S. Kesar, M. Hess, S. E. Korbly, R. J. Temkin, accepted for publication in Phys. Rev. E.

[75] A. S. Kesar, M. Hess, S. E. Korbly, R. J. Temkin, to be submitted to Phys. Rev. E.

[76] S. Nodvick and D.S. Saxon, Phys. Rev., Vol. 96, pp. 180-184 (1954).

[77] C.J. Hirschmugl, et.al., Phys. Rev. A, Vol. 44, pp. 1316-1320 (1991).

[78] H. Brownell, Private Communication.

[79] J. Haimson, B. Mecklenburg and B.G. Danly, Proc. of Pulsed RF Sources for Linear Colliders, AIP Conf. Proc. Vol. 337, AIP Press, New York, pp. 146-159 (1995).

[80] J. Haimson, et.al., Proc. of High Energy Density Microwaves, AIP Conf. Proc. Vol. 474, AIP Press, New York, pp. 137 (1999).

[81] J. Haimson, et.al., Proc. of Adv. Acc. Concepts, AIP Conf. Proc. Vol. 398, AIP Press, New York, pp. 898-911 (1997).

[82] J. Haimson and B. Mecklenburg, Proc. of Adv. Acc. Concepts, AIP Conf. Proc. Vol. ,New York, pp. (1994).

[83] W.J. Mulligan, et.al., IEEE Trans. Electron Dev., Vol. 38, pp. 817-821 (1991).

[84] T.S. Chu, et.al., Phys. Rev. Lett., Vol. 72, pp. 2391-2394, (1994).

[85] J. Haimson and B. Mecklenburg, Proc. of 1991 Particle Accelerator Conf., IEEE Catalog Number 91CH3038-7, pp. 3183-3185 (1991).

[86] J. Haimson and B. Mecklenburg, Proc. of 1995 Particle Accelerator Conf., pp. 755-757 (1995).

[87] L.M. Young "PARMELA," Los Alamos National Laboratory report, LA-UR-91-1835.

[88] J. Haimson, Nucl. Instr. and Meth, Vol. 39, pp. 13-34 (1966).

[89] J. Haimson, Private Communication.

[90] S. Trotz, et.al. Phys. Rev. E, Vol. 61, pp. 7057-7064 (2000).

[91] G.H. Rieke, *Detection of Light* (Cambridge, Cambridge UK, 2003).

[92] N.G. Yaroslavsky and A.E. Stanevich, Appl. Opt. Vol. 7, pp. 380-382 (1959).

[93] International Radio Consultive Committee, Report 719, (1990).

[94] K.K. Mon and A.J. Sievers, Appl. Opt. Vol. 14, pp.1054 (1975).

[95] T.J. Parker, et.al. Infr. Phys., Vol. 18, pp. 215-219 (1978).

[96] I.H. Hutchinson, Infr. Phys., Vol. 22, pp. 117-121 (1982).

[97] D. Grischkowsky, et.al. J. Opt. Soc. Am. B, Vol. 7, pp. 2006-2015 (1990).

[98] K.F. Renk and L. Genzel, Appl. Opt., Vol. 1, pp. 643 (1962).

[99] A. Mitsuishi, et.al., Jap. Jo. of App. Phys., Vol. 2, pp. 574 (1963).

[100] J. Haimson, Proc. of 2004 Adv. Acc. Conf., AIP Conf. Proc., to be published.